9-2020

Survey of Airflow around a Heated Manikin as a Simulated Aeromedical Evacuation Patient on a Litter with Computational Fluid Dynamics Models

George P. Lemmer

SURVEY OF AIRFLOW AROUND A HEATED MANIKIN AS A SIMULATED AEROMEDICAL EVACUATION PATIENT ON A LITTER WITH COMPUTATIONAL FLUID DYNAMICS MODELS

THESIS

George P. Lemmer, Contractor

AFIT-ENV-MS-20-S-070

DEPARTMENT OF THE AIR FORCE
AIR UNIVERSITY

AIR FORCE INSTITUTE OF TECHNOLOGY

Wright-Patterson Air Force Base, Ohio

AFIT-ENV-MS-20-S-070

SURVEY OF AIRFLOW AROUND A HEATED MANIKIN AS A SIMULATED AEROMEDICAL EVACUATION PATIENT ON A LITTER WITH COMPUTATIONAL FLUID DYNAMICS MODELS

THESIS

Presented to the Faculty

Department of Systems Engineering and Management

Graduate School of Engineering and Management

Air Force Institute of Technology

Air University

Air Education and Training Command

In Partial Fulfillment of the Requirements for the

Degree of Master of Science in Industrial Hygiene

George P. Lemmer, BS

Contractor

September 2020

AFIT-ENV-MS-20-S-070

SURVEY OF AIRFLOW AROUND A HEATED MANIKIN AS A SIMULATED AEROMEDICAL EVACUATION PATIENT ON A LITTER WITH COMPUTATIONAL FLUID DYNAMICS MODELS

George P. Lemmer, BS

Contractor

Committee Membership:

Dr. Jeremy Slagley
Chair

Col Robert Eninger, PhD
Member

Lt Col Casey Cooper, PhD
Member

Abstract

Aeromedical Evacuations remain the predominant method used to transport patients from forward deployed areas of operations to secure locations with more robust medical infrastructure. Of particular concern is the transportation of chemical warfare casualties and infectious patients resultant from biological warfare or normal communicable disease. The C-130 is one of the few cargo aircraft used by the United States Air Force designed to land and takeoff from austere airfields. The placement of an infectious patient is designated in the rear lower litter position to reduce the chance of exposure to the flight crew. Basic precautions are prescribed as well as the general airflow characteristics of the aeromedical environment during patient transport.

Specific airflow characteristics paired with environmental control system settings are a gap in scholarly literature. Computational fluid dynamics models were created to simulate the airflow around a patient represented by human geometry using commercially available software. In order to compare simulated and experimental results a heated manikin was placed in the MURPHEE aerosol exposure chamber and velocity of the airflow was surveyed. The survey and model results indicated that the heated manikin generated a thermal plume that increased the airflow on average at 18/33 experimental positions and 26/33 model positions. The Mann-Whitney U test showed that 28/33 positions were significantly different ($p<0.05$) between heated/unheated sample positions. More research is required to determine the impact of multiple litters during aeromedical operations and impact on cross contamination from patient to aircraft or aircrew.

Table of Contents

Page

List of Figures

Page

Chapter IV

List of Tables

Page

Chapter IV

List of Equations

Page

Chapter IV

SURVEY OF AIRFLOW AROUND A HEATED MANIKIN AS A SIMULATED AEROMEDICAL EVACUATION PATIENT ON A LITTER WITH COMPUTATIONAL FLUID DYNAMICS MODELS

I. Introduction

General Issue

1.1 Knowledge Gap About Airflow in Aircraft During Aeromedical Evacuation Operations Following Possible Chemical Biological Radiological Nuclear (CBRN) Event and Patient Transport

There is a knowledge gap in scholarly literature about the exact airflow characteristics in military aircraft especially in older cargo aircraft used for Aeromedical Evacuations (AE) operations. AFI 48-307v1, *En Route Care and Aeromedical Evacuation Medical Operations*, states general airflow characteristics for several aircraft used during AE operations and general precautions to use during transport of infectious patients (US Department of the Air Force, 2017). The general airflow top to bottom and aft to forward dictates that the location for transport of an infectious patient in a C-130 aircraft is the bottom rear most litter location. Infectious patients can be as simple as transporting patients with common communicable diseases or the result of a biological attack.

It was demonstrated qualitatively with smoke tubes that the flow within a C-130 is turbulent and matches the described aft to forward airflow pattern. The release of *B. subtilis var. niger* spores quantitively demonstrated that up to 3% of the spores introduced inflight reached the flight deck. This work was performed on a C-130E (Clayton, 1976) and the C-130 has undergone some platform upgrades since then including new engines and lengthened cargo compartment (Martin, L., 2013). Previous work surveyed the airflows, temperature, thermal

comfort and skin temperatures during training AE missions on C-130E and C-130H aircraft. Data collected can be used to create computational fluid dynamics (CFD) models that can solve for simulated airflow velocities and particle transport in a C-130 during AE operations (Walsh, M.; Clayton, 1976).

The modeled the interior of a C-130 based on high resolution 3-D scan of an AE training aircraft to predict transport of biological contamination during patient transport. The model predicts that up to 70% of aerosol particles equal to or less than 10 μm would stay entrained in the flow patterns modeled in a C-130 which were circular in nature along the fuselage of the aircraft. The longest particle tracing model duration was 121s and demonstrated possible particle transport from front to aft (Duran, 2019).

1.2 Problem Statement

A complete understanding of the inflight flow characteristics of C-130H and J aircraft is a gap in scholarly literature. The most informative data available came from older models of the aircraft with or without patients and it is unknown if that can be applied to newer models of the aircraft. The flow characteristics within the aircraft will ultimately determine the fate small particles that are transported by fluid flow and are not likely impact larger particles dominated by gravitational settling. Because the flow characteristics can only be determined by real world inflight data gathering it was decided to focus on the patient and the airflow characteristics around a simulated litter bound patient.

The patient is the source of contamination in AE operations whether biological or chemical contamination is suspected. The scale of resources and time required to study manikins instead of conducting human research or full-scale environmental monitoring inflight on a C-130

is greatly reduced. In order to study airflow around a manikin an exposure chamber was required to study the airflow around and downstream from a manikin.

1.3 Research Objectives/Questions/Hypotheses

The first research objective was to perform a gap analysis on exposure and decontamination from CBRN events. The research focused on gaps as it pertains to patient decontamination and safe transport during medical evacuation. Using the gaps identified from this research to conduct individual research utilizing an aerosol exposure chamber. This research objective is addressed in Chapter II.

In order to conduct research an aerosol chamber needed to be built and characterized. Additional work was performed to model the chamber using computational fluid dynamics (CFD) to correspond to the measured air velocities from the characterization process. This research objective is addressed in Chapter III

The airflow around a heated manikin was measured and compared to unheated conditions. The survey included downstream positions and specific locations on the manikin. The comparison between heated and unheated airflow was performed using the MURPHEE chamber to create a constant airflow at 0.20m/s. CFD Models were created to inform about airflow around the human geometry in 2-D. Representative 3-D models were created and compared to the measured experimental data. This research objective is addressed in Chapter IV.

Investigative Questions

Does the heat flux from a heated manikin change the observed windspeed by decreasing the air velocity due to thermal plume effect?

Can computational fluid dynamics and coupled heat flux models accurately predict the airflow around human geometry, heated human geometry and human geometry on a simplified litter?

Thesis Outline

This thesis has five chapters. Chapter I introduces the research and describes the general issue to be addressed by the remaining chapters by focusing on specific research objectives. Chapter II provided a portion of the literature review required to perform the research in Chapter IV; Chapter II is a published article addressing several gaps in published literature relating to patient decontamination and transport of CBRN casualties. Chapter III describes the design and characterization of the MURPHEE aerosol exposure chamber with CFD model. Chapter IV describes the experimental survey of windspeeds around a heated manikin and CFD models for air flow around human geometry, heated human geometry and human geometry on a simplified litter. Chapter V is the conclusions, recommendations and limitations of the research conducted.

II. A Review of CBRN topics related to military and civilian patient exposure and decontamination.

Chapter Overview

The purpose of this chapter was to perform a literature review of predominantly focused on chemical and biological agent research. The literature reviewed determined a gap in the research about decontamination and the environment during aeromedical evacuation. The gaps would provide the basis for future student research at the Air Force Institute of Technology.

This chapter was a collaborative effort with Ms. Emily Titus and reviewed by thesis chair Dr. Jeremy Slagley and committee member Col Robert Eninger, PhD.

The article was published in the American Journal of Disaster Medicine, Vol. 14, No.2 in Spring 2019; see Appendix I.

III. Design and Characterization of Multi-Use for Research for Particulate Hazards and Environmental Exposures (MURPHEE) Aerosol Test Chamber.

Chapter Overview

The purpose of this chapter is to describe the design and characterization of an aerosol exposure chamber. The exposure chamber would be used in effect as a wind tunnel to generate a constant airflow around a heated manikin for the research conducted in Chapter IV. This research was a collaborative effort with Ms. Megan Steele, Ms. Emily Titus, Mr. Jacob Denney and reviewed by thesis chair Dr. Jeremy Slagley, committee members Col Robert Eninger, PhD, and Lt Col Casey Cooper, PhD.

The manuscript is currently submitted to Aerosol Science and Technology and undergoing review and revision. The article and supplemental information as submitted is found in Appendix II and Appendix III respectively.

IV. Survey of Airflow Around a Heated Manikin as a Simulated Aeromedical Evacuation Patient on a Litter with Computational Fluid Dynamics Models

Chapter Overview

This chapter describes the experimental and modeling efforts resulting from the gap analysis of chemical and biological decontamination and patient transport conducted in Chapter II (also see Appendix I). The efforts to design and characterize the test chamber used are described in Chapter III (also see Appendices II and III). This chapter addresses how the airflow passes around a simulated patient on a litter and the impact of using a heated manikin to simulate the environment of a C-130 aeromedical evacuation. Computational Fluid Dynamics (CFD) was used to compare experimentally measured values to the modeled conditions.

4.1. General Issue

The United States Air Force provides aeromedical evacuation (AE) to all other branches of service to move battlefield casualties that require medical attention that cannot be provided in potentially austere deployed environments. The role of AE is distinct from medical evacuation (MEDEVAC), that falls on each branch of the armed forces, in that AE is a secondary transport and follows some form of MEDEVAC from the battlefield. Independent of AE, Critical Care Air Transportation Teams (CCATT) augment the AE resources for patients requiring advanced medical care, limiting patients to 3 or 6 depending on the level of care required (US Department of the Air Force, 2015). CCATT is not intended for response to mass casualty events such as a chemical, biological, radiological, or nuclear (CBRN) attack.

Response to CBRN events are established by *Updated Guidelines for Mass Casualty Decontamination During a HAZMAT/Weapon of Mass Destruction Incident, Volumes I and II*

for military and civilians alike (Lake, 2009). The most common response to such events is patient decontamination and transport away from the incident site. AE allows for transport of patients that are victims of CBRN attack following decontamination and also infectious patients while using modified Centers for Disease Control (CDC) guidelines. The specific guidelines for each agent should be followed, however the general guidelines are the wear of N95 filtering face piece respirator for the infected patient and anyone within 10 feet or providing direct care. General droplet precautions describe droplets greater than 5 μm can travel up to 3 feet are produced by actions such as talking, sneezing and coughing as described in Air Force Instruction (AFI) 48-307v1, En Route Care and Aeromedical Evacuation Medical Operations, (US Department of the Air Force, 2017). Better distinction between droplets and aerosols should be made, defined separately, to establish the basis for particle transport within aircraft. Further confounding the need to make AE of CBRN patients is the variety of aircraft the United States Air Force (USAF) has at its disposal to perform AE with each having their own unique airflow, internal thermal conditions and litter transport capacity.

General airflow characteristics are listed in AFI 48-307v1 (US Department of the Air Force, 2017) for 5 aircraft; 3 cargo (C-130, C-17 and C-21) and 2 tanker (KC-135 and KC-10). Relevant information about each aircraft is listed in Table 1 (Church, 2020). Additionally, AFI 48-307v1 (US Department of the Air Force, 2017) provides exception authority to theater surgeons and directors of airlift operations for intra-theatre transport. Approval from Major Command (MAJCOM), Transportation Command, and respective surgeons general of the destination if inter-theatre transport is required. Meaning the same document that recommends against transporting highly infectious patients prescribes the approval process to allow it.

Table 1. List of Aircraft with Described Airflow and Litter Count

Air Frame	Model	# of Aircraft	Litter Capacity	Date of First Delivery
C-130	H	171	74	March, 1965
	J	132	74	February, 1999
C-17		222	36	June, 1993
C-21		19	1	June, 1998
KC-135	R	343	Not Listed	July, 1984
	T	51	Not Listed	July, 1984
KC-10		59	Not Listed	March, 1981

Chapter II and Appendix I identified several gaps in the research of CBRN decontamination and AE. The study of airflow around a litter bound patient is a poorly studied phenomenon as it pertains to military aeromedical evacuations (AE) and possible cross contamination from patients to aircrew or aircraft. The prescribed droplet considerations likely do not take into account the dry conditions and airflow characteristics of individual aircraft aside from recommendation to wear a mask if there is any mix of cabin and flight deck air.

Chapter III along with Appendices II and III described research efforts to design, build and characterize an aerosol exposure chamber appropriate for exposures at or below windspeeds of 1 m/s and a Computational Fluid Dynamics (CFD) model to inform about chamber airflow characteristics.

4.2. Literature Review

4.2.1. C-130 Literature

The airflow characteristics and thermal environment within a C-130 cabin can be characterized from several different scholarly texts, service publications and AFI 48-307v1. The general airflow described by AFI 48-307v1 is from top to bottom aft to front with mixing of the cargo bay and the flight deck (US Department of the Air Force, 2017). Additionally, the

Technical Orders (TO) involving the air conditioning system were reviewed for any relevant technical data to better characterize the internal thermal environment in a C-130. The TOs generally stated operation and control of the air conditioning system and certain trouble shooting and repair operations and did not provide much relevant data. The pressurization system requires certain torque specifications to provide a 'leaky' ducting system to maintain adequate cabin pressurization. The cabin altitude can maintain sea level pressurization up to aircraft altitude of 18,000 feet and cabin altitude up to 5,000 feet up to aircraft altitude of 28,000 feet. The air conditioning is designed to maintain a cabin temperature range of 68-75°F (US Department of the Air Force Technical Order). Additional information is distributed through Service News by the Lockheed publications division.

The series of Service News publications ran for 30 volumes from 1974 – 2005 were open source publications notifying maintainers of service tips, platform modification and other general news pertaining to the C-130 platform from A to J. One point to consider if reviewing the documents is that there is no correlation between Lockheed serial numbers and Air Force Tail Numbers (Roy, 1975), so each individual aircraft could have different equipment than current production models if a full retro fitting of updated equipment is not performed. A series of changes and upgrades have been performed on the air conditioning systems of the C-130. As such the general air conditioning characteristics will be described that apply to all stages of platform upgrade (Matulich, 1991).

Air that enters the C-130 cabin and flight deck is derived from engine bleed air (hot air), engine bleed air that has passed through a heat exchanger (cool air) and cool air that is passed through an expansion turbine (cold air) with approximate temperatures of 600°, 140-200° and 35°F respectively (Roy, 1975). Mixed cool and cold air pass through a water separator which

removes ~70% of free moisture in air at altitude before entering the cargo bay and flight deck (Wood, 1989). Heat is provided optionally by adding hot air to mixed cool and cold air and then enters the cargo compartment. The conditioned air enters the cargo bay from the top of the cabin and optional heat is added from the floor with a separate system of ducts designed to maintain a cabin temperature of 75°F. It is stated that if both the air conditioning and the heat are operating the heat will dominate the mixed conditioned air (Roy, 1975).

A variety of valves and sensors control then direct the flow of air in the ducting with the cabin thermostat located at fuselage station 357 (left side of the aircraft) and a recirculating fan located in the overhead ducting at either fuselage station 450 or 460 (Roy, 1975; Roy, 1976). Bleed air from each system is provided by the engines and conditioned air introduced at 70 pounds per minute at sea level, the flight deck and the cabin each have an independent air conditioning system. The airflow is regulated with an outflow valve under the flight deck dictating the aft to front airflow pattern.

A single work is often cited to describe the airflow and transport of microbiological organisms in a Canadian C-130E aircraft (Clayton, 1976). Using Dräger air current tubes, smoke tests on board an aircraft on the ground and inflight smoke traveled from aft to forward under all test conditions. Without pressurization it was noted that most of the smoke drifted directly towards the outflow valve under the flight deck. While inflight the smoke flowed aft to forward with counter clockwise swirl and rotation in the aft half of the cargo bay and clockwise swirl and rotation in the forward section of the cargo bay estimating 20% drifted into the flight deck. Additionally, to the qualitative smoke visualization, bacterial spores (*B. subtilis var. niger*) were aerosolized and sampled using a Wilson Mono mask. The spores were released from the aft of the cargo bay directed forward with freon as a propellent. As much as 3% of the sampled

spores reached the flight deck and were sampled at 12 separate positions throughout the crew compartment and flight deck over the duration of approximately an hour and forty minutes. The study simulated a single highly infectious patient that demonstrated the possibility for biological agents to migrate the entire length of a C-130E aircraft in flight.

4.2.2. C-130 Patient Conditions

The C-130 aircraft has over 30 cargo configurations as delineated by AFI11-2C-130JV3ADDA, *C-130J Operations Configurations/Mission Planning*, (US Department of the Air Force, 2009) with 5 being dedicated AE configurations in each of the long or short aircraft. The general cargo layout is divided into sections that cover a set area and can hold a fixed payload called a pallet. Palletization it allows logisticians to plan for cargo and patient loads appropriately. The AE configurations are described as such i.e. CONFIGURATION AE 1-5 and represent an allotment of litter positions, ambulatory patient/passenger seating, equipment pallets and AE medical providers and loadmaster personnel. Crew seating is 9 or 10 with passenger capacity ranging from 0-53 and litter patients from 10-97, in conversations with military personnel at the School Aerospace Medicine it was related that CONFIGURATION AE-3 is the most common operational configuration. CONFIGURATION AE-3 provides 20 litters covering 2 pallets, 53 ambulatory patients/passengers and 9 crew seats.

A pallet of litters consists of up to 10 litters with 5 on each side of the center line of the cargo bay with brackets anchoring the litters in place to the floor and ceiling. Litter locations are identified by pallet location designated by letters according to the Configuration AE with individual litters a numbered 1-5 from bottom to top. Cables with brackets anchor the opposite side of the litter to the ceiling and floor and each litter arranged vertically in the pallet. Litters will be placed with at least 18” of vertical separation. The official North Atlantic Treaty

Organization (NATO) designation for AE appropriate litter/stretcher is STANAG 2040 with detailed specifications for support brackets and dimensions being found in NATO Standard AMedP-2.1 Stretchers, Bearing Brackets and Attachment Support (NATO, 2013). The number of patients able to be transported in a given AE is primarily dictated by the number of attending AE crew and pallet configuration. A computer aided design (CAD) drawing of a litter pallet can be seen in Figure 1.

The thermal environment in C-130 E & H aircraft is best characterized in the thesis *Thermal Environment of Litter Positions and Human Responses onboard Hercules C-130 Aircraft* (Walsh, 1998). The thesis is a non-experimental characterization of the airflow and temperature around different litter positions with flight crew as surrogate patients. The correlative nature of the survey is of limited use for validating CFD models but does provide ranges of values that give insight to the overall flow characteristics and temperature inflight during C-130 AE operations.

The ambient air temperature was recorded by hotwire anemometer and reported by litter position. The range of ambient temperatures was 15.1-29.3°C across all positions, but the range of average temperatures was 21.6-25.8°C (which converts to 70.9-78.4°F) closely matching the reported 68-75°F design characterization from the TO (US Department of the Air Force Technical Order). The status of heat and air conditioning was not reported thus a control setting could not be correlated with cabin conditions. The hot wire anemometer was also used to record airflow across the litter positions.

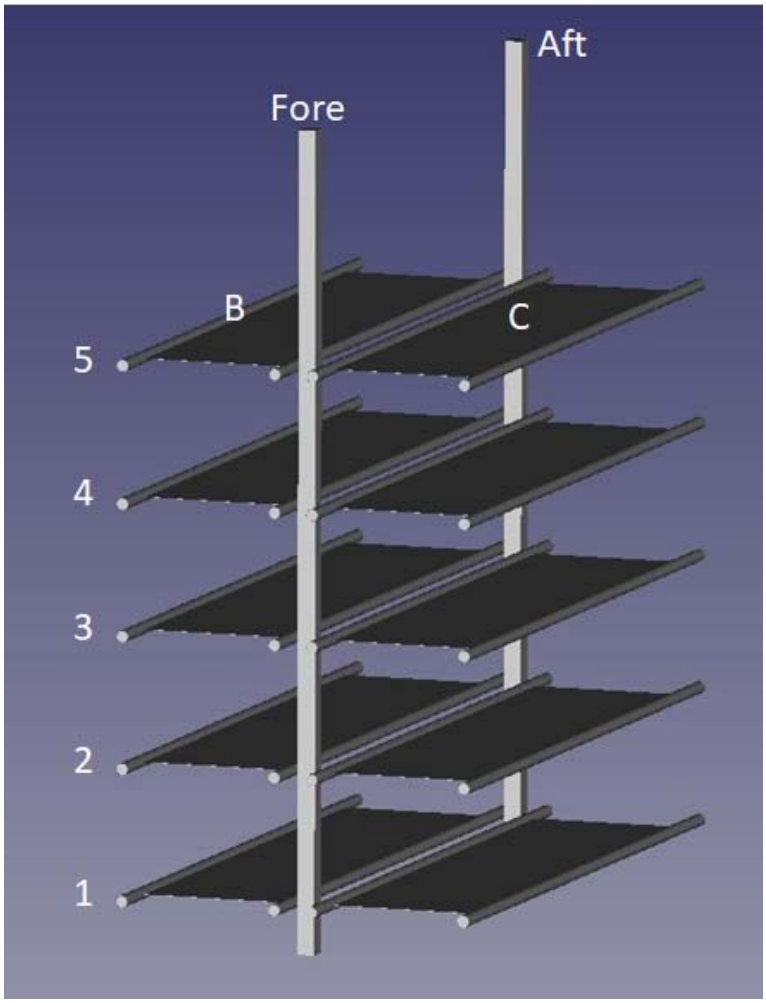

Figure 1. CAD Representation of a Litter Pallet Containing All Litters.

The airflow was recorded 12" above the litter at the surrogate patients' hips, centered across the litter. The range of airflows recorded ranged from 0-0.6m/s across all positions with the range of averages being 0.03-0.29m/s measured while inflight. The anemometer was reported to have a measuring range from 0.2-20m/s with resolution of 0.1 m/s and accuracy $\pm$3% meaning that only higher air velocities were likely within the instrument's ability to measure accurately. It is also worth noting that for almost all of the measurements outside of the rear

lower litter position the standard deviation was equal to or greater than the reported mean. In addition to airflow and air temperature the patient skin temperatures were recorded.

The skin temperature was calculated using a method of adding the chest and bicep measurement, taking 35% of that value and adding it to 15% of the thigh and calf temperatures described by Mitchel and Wyndham, 1969. The range of skin temperatures reported was from 28.7-35.2°C with the range of averages 29.2-34.5°C. All body temperatures from surrogate patients represented healthy individuals and would not necessarily be representative of actual patients needing AE.

4.2.3. CFD and Worker/Patient exposure

The bulk flow of the interior of a C-130J has been modeled using CFD as it pertains to biological contaminants. The work summarizes that the biological particles would generally not travel greater than 9 ft when released in the forward section of the aircraft but that particles of 0.1 and 1.0 µm were more likely to be transported to the flight deck. The study simulated releases with time dependent iterations of 100,000 particles over the course of 180 seconds. The model showed that the airflow within the aircraft can be quite turbulent and approximately 70% of particles can stay entrained in the bulk flow for the extent of the simulation. The remaining particles were removed by the ventilation outlets (23.4%) or deposited on horizontal surfaces (6.3%) being removed from the bulk flow (Duran, 2019). Since patients are considered the source of contamination efforts are made to create realistic representations by using manikins that can simulate breathing or are heated to represent the thermal load of a real person.

Coughing and sneezing are commonly recognized as the mechanism of biological delivery for infectious modeling. When investigating the effects of thermal plume on airflow a simulated seated manikin was used to model coughing and droplet dispersal when considering

thermal plume and droplet evaporation at 50% relative humidity. The model showed that there would be a thermal plume around a seated individual, this would have an impact on the overall dispersal of a sneeze by having a buoyant effect when compared to a non-heated model. Additionally, it was reported that their model showed an approximate 26% reduction in droplet size across all size ranges when considering evaporation impact on particle size. The conclusion of the model showed that particles between 3.5-20 µm would be affected by the upward flow of buoyancy from exposure to body heat after experiencing evaporative loss in particle size (Yan, 2019). It should be noted that this article is completely model based without an independent experimental validation but shows that heat load of individuals could be of concern when considering transport of particles 20 µm and below.

One way to visualize particle flow is to use particle image velocimetry. This involves the use of a laser to illuminate the particle and high-speed photography to measure velocity measuring the displacement across several planes of illumination if necessary. Experiments conducted in a climate-controlled (20-35°C in 0.5°C intervals) room (5m x11m x 3m) and thermal manikin (30°C skin temperature and 1.7m tall). By controlling the ambient temperature to 20°C, 30°C and 35°C and airflow of 1.0m/s or still air; smoke was used for particle tracing around the manikin. At airflow of 1.0 m/s no discernable plume was visualized across the temperature ranges studied. At the near still air condition a thermal plume was visualized at various areas ranging from 0.08-0.15m/s (Arinami, 2017). Seated models have been used when studying building environment and of interest to Industrial Hygienists, the use of standing manikins have also been used to simulate worker exposure to work place hazards.

Heated manikins in the standing position can impact the observed worker exposure from work place hazards. A large exposure chamber was used to estimate worker exposure by

controlling ventilation velocity (0-0.8m/s), turbulence and thermal condition of the manikin (90W of radiant and convective heat). The work explored a worst-case scenario exposure to a worker with their back to the direction of ventilation flow and the exposure to the workers front creating a wind break and reducing the effectiveness of the industrial ventilation. The amount of free stream turbulence modeled (10-80%) directly impacted the amount of exposure with an inverse relationship to the free stream turbulence intensity. An unheated manikin showed that as ventilation velocity increased the resulting exposure decreased thus working as intended. Heating the manikin under the same conditions resulted in a maximum exposure concentration between 0.15-0.30 m/s when exposed to the vapor (Li, 2007). Seated and standing scenarios can be representative of ambulatory patients but apply less to patients that would be stretcher bound.

The construction of an operating suite that utilized horizontal flow instead of laminar down draft was constructed using a fan filter unit providing High Efficiency Particulate Air (HEPA) filtration with air flowing horizontally across a simulated patient on an operating table with lamps and surgeons for heat sources. Inflow velocity was validated to be 0.32m/s. The simulated particle size was monodispersed 5 μm to simulate skin cell particles. Each light was assumed to be 100W and each person to contribute 150W when calculating thermal conditions within the room. The horizontal flow was reported to provide adequate washing effect to reduce contaminants at the patient that were produced by the simulated surgeons and the patient (Liu, 2009). The surgical patient with horizontal flow is the closest representation to that of a litter patient in a C-130 environment simulating release of biologic agents.

4.3 Methodology

4.3.1. Experimental Design

The need to characterize a C-130 AE environment is still a research gap that needs to be addressed to create accurate validated CFD models. The ability to perform sampling on an aircraft requires all of the equipment to have been approved for use during flight which is a time restrictive process. Additionally, it is unknown if the aerospace ground equipment (AGE) carts used to provide air conditioning on the ground provide as much airflow and conditioned air as the engines provide during flight and if the carts provide the same internal flow to study that environment instead of inflight during AE operations Several AE C-130 training environments were visited in order to become familiar to the setup of the inside of the aircraft.

The USAF School of Aerospace Medicine on Wright-Patterson Air Force Base provided the opportunity to generate a 3-Dimensional (3-D) scan of the interior of a C-130 used for training purposes (Duran, 2019). The original intent was to use the high-resolution scan to create CFD models but due to the lack of information on the C-130 internal airflows and the complex nature of designing CFD models with intricate geometries, simplified models were determined to be more appropriate. Models with many million degrees of freedom can take many hours or days to solve even on high performance computers designed for modeling. The exposure chamber described in Chapter III (and appendices 2 and 3) with representative models was determined to be appropriate to characterize airflow around a representative litter bound patient.

The experiments described hereafter were designed to measure airflow around and downstream from a manikin and determine if CFD models can accurately calculate the turbulent environment within the MURPHEE chamber. Based on the properties of volumetric flow it would be expected that the velocity would increase around the manikin as the cross-sectional area of the chamber is displaced by the volume of the manikin and return to normal velocity downstream from the manikin. Heating the manikin accounted for the thermal output of a

human and is expected to slow the air as detected by hot wire anemometer because of a thermal plume rising around the manikin. Statistical analysis conducted focused on comparing the sampled populations from each chamber configuration (empty chamber, litter assembly without manikin and litter with heated manikin) and comparing the sampling positions closest to the manikin surface and downwind from the manikin while heated.

In order to characterize the airflow around a litter bound patient it was determined necessary to utilize a manikin instead of recruiting human volunteers. This is due to additional logistics to support human subjects and the additional requirements to conduct human research. A large body of literature supports the use of manikins thus it was not determined to be a detriment to the research. When determining the appropriate manikin to use those designed for research can be cost prohibitive. In order to determine if the manikin was appropriate, measurements were taken and compared to anthropomorphic data gathered by the Department of Defense (US Department of Defense, 1991, Gordon, 2014). The data was used to scale the human geometry used during modeling and as a means to compare the manikin to the modeled geometry.

Before sampling was conducted several preliminary CFD models were generated 2-dimensionally (2-D) to qualitatively assess the impact of body size on airflow. The body size models were based on height as the determining factor, creating a side view of the 3-D geometry (TurboSquid.com, 2020) scaled to the 90^{th}, 75^{th}, 50^{th} and 25^{th} percentiles for height based on stature measurement in the anthropomorphic literature. The appropriate percentiles were nearly identical based on males in the United States Army, 1988 (US Department of Defense, 1991) and United States Army Males in 2012 (Gordon, 2014) thus deciding to use the 2012 values. The 2-

D representations were imported to the CFD software and solved to gain insight into possible sampling sites and the impact of heat on the flow around the manikin.

A digital representation of the model was used but was a more general anthropomorphic design not a direct copy of the heated manikin. The 3-D geometry was acquired under the standard license from TurboSquid.com (TurboSquid.com, 2020), which allows for use by others to edit and use for modeling purposes. The original geometry was scaled based on height to 90th percentile using Autodesk MeshMixer® and measured using FreeCAD software. The reported measurements for the 3-D geometry and manikin are reported on Table 2, with appropriate anthropomorphic percentiles. The geometry was modified using Autodesk MeshMixer® to place the arms at the side and to fit the width of a litter; creating a posture more representative of a stretcher bound patient. The model was also post processed using MeshLab (Cignoni, 2008), to reduce the total number of vertices, file size and geometry detail. SolidWorks® was used to convert the file type to a parasolid file format .x_t to make importation to COMSOL Multiphysics® more reliable with respect to geometry preservation.

The human geometry is larger in each of the measured dimensions except tragion height while standing indicating that anatomical landmark is higher on the manikin then the human geometry. The tragion height to the top of the head is in the 1% meaning that from about the mid ear to the top of the head is very short indicating a small head based on height alone. The head length agreed with the other percentile ranges at the 15th percentile. The manikin head appeared anthropomorphic and does not look out of proportion on the manikin but has small measurements when considering anthropometrics. The manikin was assumed to be appropriate because the scaled geometry should retain the same shape; it would just be larger on the human geometry than on the manikin.

Table 2. Measurements of Manikin and 3-D Human Geometry

Measurement Description	Heated Manikin (cm)	Percentile	Human Geometry (cm)	Percentile
Chest Breadth	27.3	20th	31.3	90th
Chest Depth	22.9	15-20th	27.5	75-80th
Hand Breadth	8.4	10-15th	9.15	75-80th
Head Length	19.2	15th	21.7	99th
Tragion Height, Standing	174.9	95-97th	170.4	85-90th
Tragion-Top of Head	10.5	1%	14.2	97th
Stature	184.2	85-90th	184.6	90-95th

4.3.2 Methods

In order to heat the manikin a heat source had to be added that was representative of the human heat load to generate a thermal plume around a litter bound patient. The literature review showed that several methods of determining the heat load of a person as represented by a manikin can be taken. The first is uniform temperature of the manikin surface and the second is a heat source representative of the thermal load of a human not accounting for temperature as surface temperature varies on the human body (Kelly, 2006). A hybrid approach was determined to be the best suited based on availability of equipment and time requirements. A heat lamp of 150 W with a dimmer switch (manufacturer details can be found in Appendix IV) was used to generate heat and a series of temperature sensors to record temperature from several areas across the manikin. The assembled manikin did not allow for airflow between body sections because the torso, hips with right leg, head, each arm and the left leg were separate pieces. The rear of the torso was cut out and reattached with hinges to access the internal cavity of the manikin. Each body section had plastic material removed to allow airflow throughout the entire internal volume of the manikin.

The heat lamp was positioned in the upper chest with a metal shade around the bulb fixture with an additional aluminum piece 5.5” long by 10.5” wide and 0.02” in thickness. The added aluminum created a semicircular extension of the shade to reduce hotspots on the manikin surface. The shade had several holes cut out to allow for heat to transfer through flexible metal dryer ducting away from the bulb. The internal air was circulated by a fan powered by 9 V battery. Without addition of the aluminum shade and fan the chest surface temperatures would exceed 45° C and there was little to no temperature increase in the head and extremities. Additionally, a thermal imaging camera was used to approximate the surface temperature during the manikin development phase. The images were used to refine the housing around the lamp to avoid hot spots based only on lamp proximity and was much more efficient than using the thermocouples for measurement of whole-body temperature.

Heating of the manikin was controlled by the dimmer switch that was preset and left in that position set to 81.3V; this was checked with multimeter prior to initiating sampling. Single phase alternating current electricity exhibits the relationship presented in Equation 1, with the power factor of an incandescent bulb being 1. The expected wattage of the dimmed bulb would be 101.625 W. In order to move the air inside the manikin a brushless DC fan was attached to the interior of the manikin at the seam between the torso with attached leg and the chest portion of the manikin. The fan was directed towards the legs with the intent of greater heated airflow to the lower portion of the manikin.

$$Watts = Power\ Factor\ x\ Amps\ x\ Volts \qquad \text{Equation 1.}$$

The manikin was to be placed on the litter and held by the litter assembly which was designed to resemble the actual litter assemblies on AE configured C-130 aircraft. The handles of the litter were approximately 2 feet downstream from the inlet HEPA filter bank. Square tube

steel support 2” in diameter were braced between the top and bottom of the chamber with round brackets attached to hold up one side of the litter. The other side of the litter was held in place with plastic coated braided steel cable attached to the outside of the top of the chamber. The experimental setup is pictured next to AE litter and training manikin in Figure 2. The orientation of the manikin was head towards the filter bank inlet of the chamber meaning the direction of flow was from head to foot in order to simulate the bottom rear litter patient during AE. The seams of the manikin were taped to limit heat loss during experiments. The initial plan was to scan the manikin and litter to import the exact geometries but that task could not be accomplished because access to facilities were limited in response to the COVID-19 pandemic and time constraints. The litter was simplified and represented as a flat plane drawn in the modeling software under the manikin and joined as a separate domain during CFD modeling.

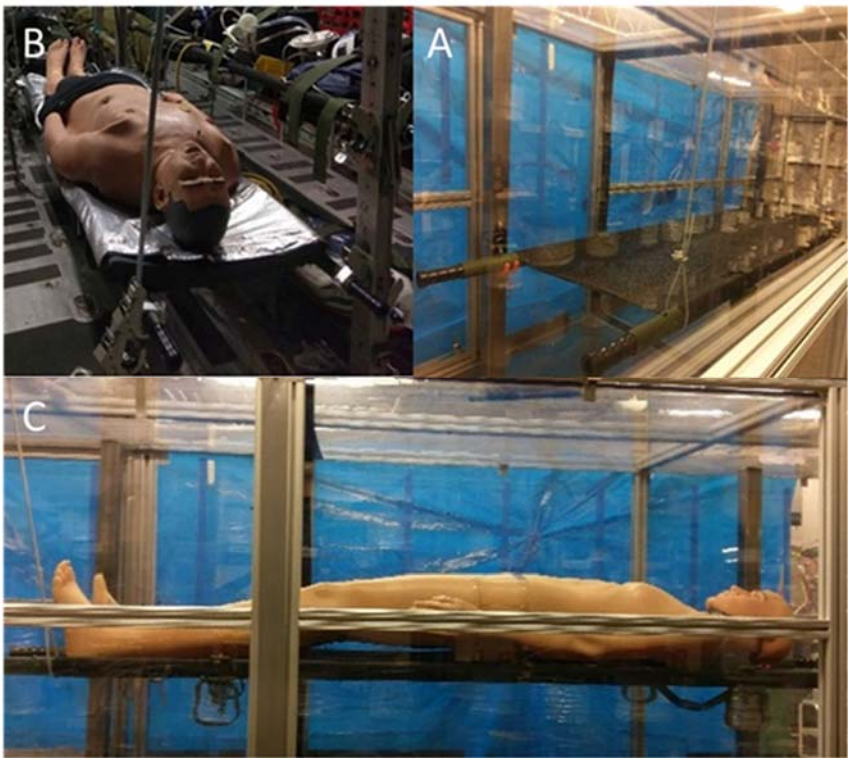

Figure 2. Experimental Setup (A), AE Training Patient (B), Heated Manikin (C).

The transport equations for RANS k-ε used by COMSOL are described in Chapter III. The Heat Transfer in Solids module (COMSOL, 2018) was used to model heat exchange in the modeling domains coupling the turbulent flow modeled in the Turbulent Flow k-ε module (COMSOL, 2018). The Equations for heat transfer for are presented in equations 2 and 3 (COMSOL, 2018).

$$\rho C_p \mathbf{u} \cdot \nabla T + \nabla \cdot \boldsymbol{q} = Q + Q_{ted} \qquad Equation\ 2$$

$$\boldsymbol{q} = -k\nabla T \qquad Equation\ 3$$

ρ = Density
C_p = Specific heat capacity at constant pressure
u = *Fluid velocity vector*
T = Temperature
q = *Conductive heat flux*
Q = Heat Source
Q_{ted} = Thermoelastic damping
k = Thermal conductivity

A series of models were created to examine the airflow around the human body in the lying position. The first set of models performed were 2-D generated by creating a 2-D drawing from the side orientation of the 3-D model on a litter. The first set of 2-D models were designed to measure the impact of body size relative to height based on the 90th, 75th, 50th and 25th percentiles. The next set of 2-D models was to compare the impact of body heat on fluid flow at the 90th percentile for height. Each set of models performed was intended to increase in complexity by adding physics or by recreating the model in 3-D.

Three dimensional models were carried out using the 90th percentile by height 3-D model. These models followed the same pattern as the 2-D models from less complex to more complex. The initial scenario was just the human model in the center of the fluid domain at 0.8 m downstream from the inlet filter bank corresponding to the intended experimental position of

the manikin. The manikin was added to a simplified litter, a plane representing the canvas using the thickness of the handles for the height. A separate model was created for a heated manikin. The model was centered in the chamber as described above. A list of equipment and software used is listed in Appendix IV.

The characteristics of the MURPEE chamber are described in Chapter III, Appendix II and Appendix III of this thesis and should be referenced for additional details on the chamber. The fan settings of 16Hz and 30Hz had a target wind speed of 0.20 m/s and 0.50m/s were used for the characterization of airflow around the simulated patient. A total of 28 additional sampling locations were added to take air measurements using a hot wire anemometer. Any measurement reported for chamber location was taken using the laser measure on the equipment list. The location of the sampling points is reported in Table 3.

Table 3. Location of Sampling Positions in Meters.

Sampling Positions in Meters	y	z	Position	y	z	Position	y	z
H1	0.954	0.656	B1	1.559	0.811	P1	2.737	0.664
H2	0.902	0.551	B2	1.683	0.762	P2	2.968	0.670
H3	1.029	0.554	B3	1.257	0.656	P3	3.267	0.670
H4	0.900	0.500	B4	1.562	0.659	P4	3.572	0.671
H5	1.027	0.500	B5	1.867	0.657	P5	2.735	0.394
H6	0.819	0.422	B6	2.289	0.648	P6	2.959	0.394
H7	0.898	0.414	B7	2.280	0.465	P7	3.275	0.395
H8	1.025	0.406	BA1	1.267	0.549	P8	3.575	0.394
H9	0.898	0.359	BA2	1.567	0.564			
H10	1.021	0.362	BA3	1.868	0.554			

The positions were given letter designators based on the locations of the body ‘H’ for head, ‘B’ for body and ‘P’ for post, representing the downstream sampling points. Positions with

'A' designation were added after the first round of measurements were taken to include measurements on the body surface. The positions were numbered from top to bottom then left to right with positions B2 and B7 being preexisting sampling points. The coordinates are given in meters with y indicating the length of the chamber as distance away from the filter bank inlet and relate to the planes described in Chapter III. The z coordinate is the height from the bottom of the chamber. Each sampling position was sampled at insertion depths of 0.304 m (12 inches), 0.457 m (18 inches) and 0.609 m (24 inches) with nine repeat measurements. The positions at H4, 5, 7, 8, and 9 were in line with the head and could not be sampled beyond the 0.304 m insertion distance. The values recorded at 0.457 m is the fully inserted distance with tip of the probe resting against the manikin (probe perpendicular to the surface 0.75cm away) for the above positions around the head only. H10 passed under the neck of the manikin. Sampling positions can be seen in Figure 3. Selected locations on the manikin surface were sampled from the sampling positions by modifying the insertion distance and utilizing the flexible probe. These positions were: forehead, chin, nose, top of the head, left and right side of the chest, left and right thigh and below the navel on the seam between the torso and upper body. Each body location was sampled 10 times and independently from the position sampling. Heated sampling only occurred at positions BA1-3, P1-8 and body locations: chest left/right, thigh left/right and below the navel.

The light was turned on and a temperature of 29.0° C or above was achieved at each sensor on the manikin before sampling took place. The light was turned off if all of the sensors reached a temperature of 33.0°C or higher. The internal fan was on for the duration of sampling pushing air to the legs and feet. The entire sampling process was carried out with the chamber

fan set at 0.20 m/s and 0.50 m/s with an empty chamber, litter and assembly, manikin on litter assembly and with heated manikin on litter assembly (at positions BA1-3 and P1-8).

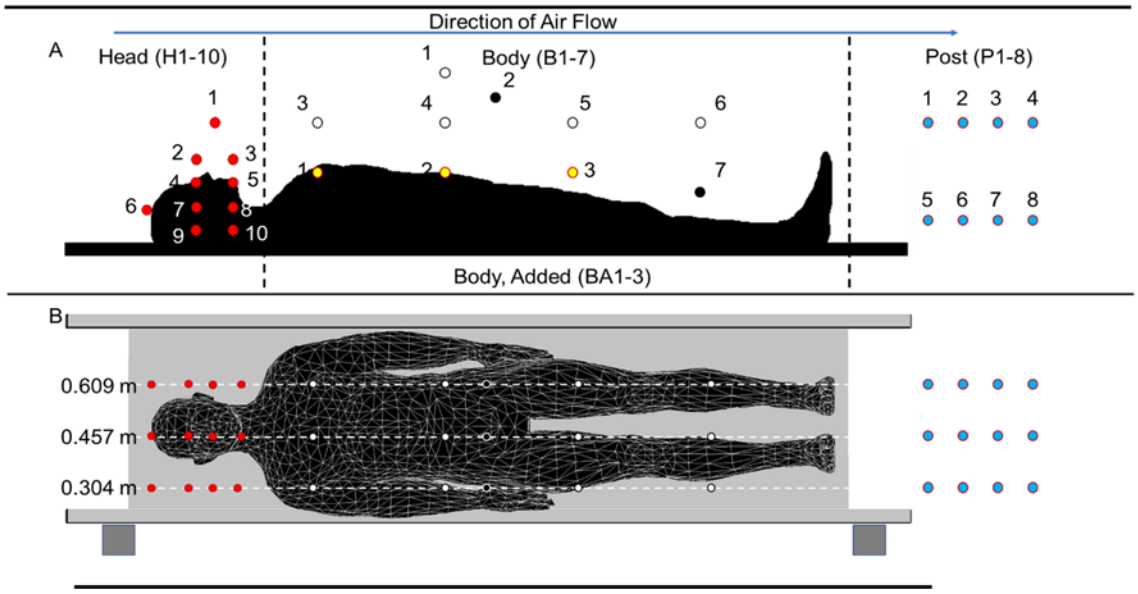

Figure 11. Thermal Image Post Airflow Measurement.

4.3.3. Computational Fluid Dynamics Methods

The fluid and heat transfer domains used the same input values for comparative purposes. The input values were based on experimental conditions so they could be compared except for the trial using C-130 conditions. Select model inputs for initial conditions, module specific inputs, material default values and user defined values are listed on Appendix V. Based on the collected data from the airflow and ambient temperature data the reference temperature for airflow used in modeling was 303 K. By mirroring the conditions during experimentation, it is possible to validate models or portions of models if the measured and modeled values are similar or very near the same.

The model described in Chapter III, and Appendices II & III, retained more of the actual physical characteristics of the exposure chamber modeling the inlets as each of the 9 filters in the

filter bank and accounting for the air leak identified during characterization. The chamber was simplified to representative geometry a cube 0.914 m wide by 0.914 m tall and 4.5 m long to reduce necessary solving time. The inlet and out let boundaries were the entire face of the cube instead of the 9-inlet design with the inlet flow set to 0.2 m/s based on the design specification. COMSOL Multiphysics® does provide default boundary conditions for fans and porous media filtration but those features were not incorporated into the original model and a solvable model with reasonably simple geometry was desired.

The more complex geometry was reserved for the human representation of the manikin in the chamber but even that geometry was simplified, removing complex surface textures of the face but leaving the representative features. The arms had to be repositioned primarily to stay within the profile of the litter. The representation of the original open source model, the modified representation and the imported model can be seen in Figure 4, (TurboSquid.com, 2020). The head of the geometry was oriented towards the inlet so the airflow would be around the simulated patient from head to feet. No clothing or blanket was added to the model so it would resemble the manikin in the experimental portion described above.

The software incorporates many material properties and references for those values in the software and also the individual module user's guides (COMSOL, 2018). These values were assumed to be valid for modeling purposes. When the physics were coupled the several additional properties were added to the model that required user defined values for the ratio of specific heat for air. The 2-D and 3-D heat models used the calculated 101.625 W from the light bulb as the value of the heat source. The ratio of specific heat for air was considered standard air for a value of 1.4 (Engineering Toolbox, 2020). In addition to appropriate initial conditions and

model inputs, the mesh surrounding the geometry impacts a model's ability to converge, resulting in a solved model.

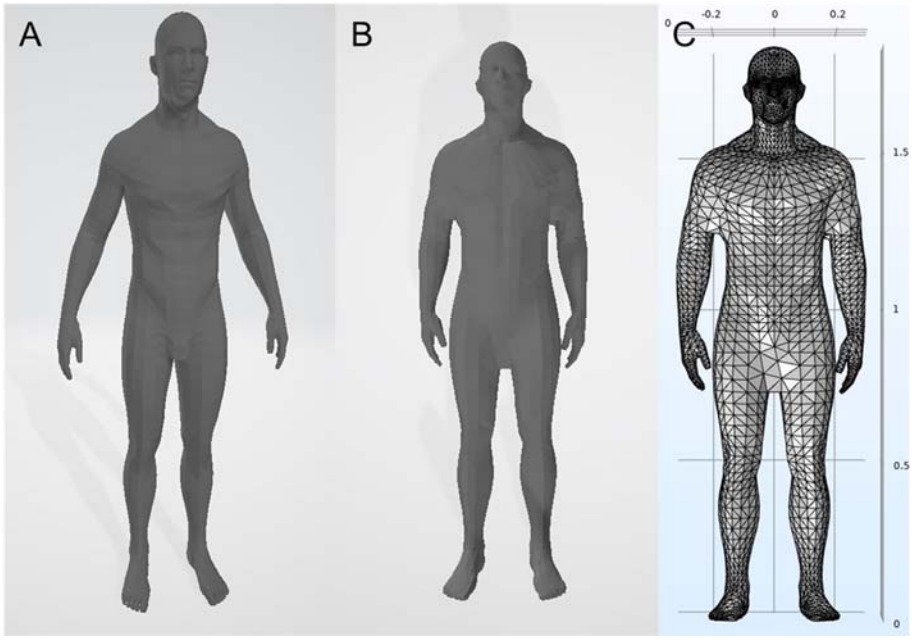

Figure 4. Original Open Source Geometry (A), Modified and Simplified Geometry (B) Imported Geometry (C).

COMSOL Multiphysics® uses the finite element method to solve differential and partial differential equations by creating a mesh or tetrahedral grid over the geometry defined in the computational domain. The mesh can be divided into polygon representations, from quadrilaterals to highly skewed or even folded elements that can impact the ability of the model to be solved. Poor geometry can lead to unsolvable models that can take days to reach the memory limits of a computer or a specified number of solver iterations failing to converge on a solution. A "perfect" model has the least defined mesh necessary to create solved models at the highest resolution necessary to solve the engineering issue at hand. The software provides

algorithms that can automatically mesh the computational domains to specified element sizes. The larger the model and the finer the mesh the more elements that are created potentially creating more accurate and higher resolution solutions but at the cost of computational time (COMSOL, 2018). For this work the provided algorithms were used with 2-D models using the fine mesh setting and 3-D models meshed at a coarse setting due to the size of the geometry. When testing for mesh quality by skewness, a value of 1 represents a perfect element; the distribution of elements is averaged and presented as a histogram by the software. The meshes generated during modeling had 0.66 skewness for 3-D models and 0.84 for 2-D models (Gothäll, 2017).

4.4. Analysis and Results

4.4.1 2-D Model Results

The qualitative analysis shown in Figure 5. does not show major difference in the predicted flow (m/s) around a man shaped object with all 4 models predicting a slowdown (blue color) at the head, behind the chin and before and after the feet. Because of this all future models were performed on 90th percentile geometry. The height of the manikin was 1.842 m placing the 90th percentile within $\pm$ 1 cm of the manikin. The next consideration was heat load from patients impacting the airflow.

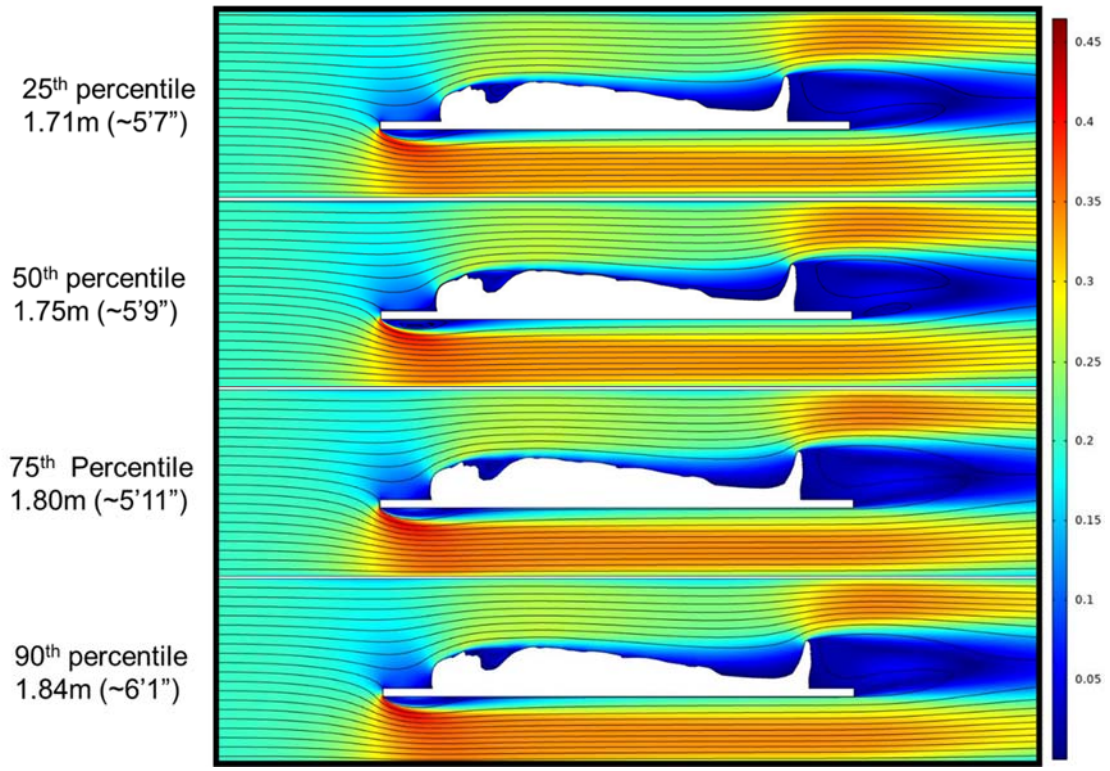

Figure 5. CFD 2-D Evaluations of Height on Flow Around Human Geometry in m/s.

The heat generated from the 2-D patient was set to 101.625 W with all other model parameters for fluid flow matching the inputs for the body size comparison models. The results are shown in Figure 6. The model indicated a slowing in velocity above the manikin and an increase in airflow velocity below for both the geometry and the heat model. The heat model showed a greater slowing of flow velocity seen in the uniform light green color above the heated model. The unheated model also shows higher air velocity downwind and above the geometry. Common model inputs, initial conditions and boundary conditions and material properties are listed in Appendix V. The next model created was a 3-D model.

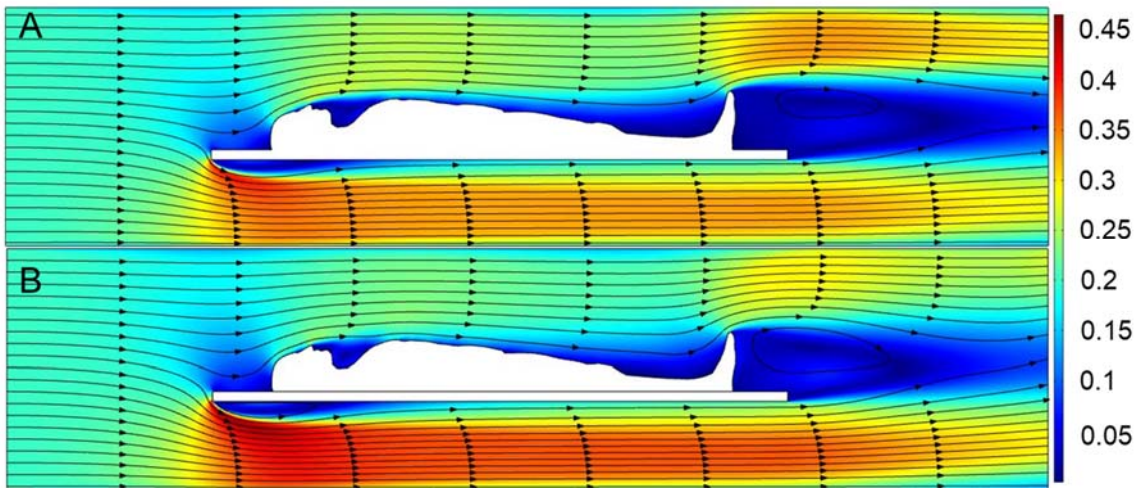

Figure 6. CFD 2-D Airflow Around a Human Geometry (A), and Heated Geometry (B) in m/s.

The examination of the airflow around a patient began with the airflow around the basic human form. The geometry is free floating in a representation of the chamber that is the fluid domain of the model as seen in Figure 7. The human geometry showed the flow slows around the surface of the geometry which represented the boundary layer formed around the geometry. The horizontal plane shows the boundary layer extends around the entire geometry and showed slower airflows between the body and arms. Slowed air was also present between the legs and downwind from each foot. The flow lines are parallel to the direction of airflow except around the feet where the flow lines demonstrated more turbulent flow. The next model was the heated human geometry.

The human geometry with a heat source of 101.625W is Figure 8. The heated geometry was set in place identical to the unheated human geometry. The heated human geometry does not exhibit the same whole body slow down around the geometry as observed in the human geometry. The flow lines parallel to flow until downwind from the chest of the geometry where the flow lines deviated from parallel to the direction of bulk flow to almost perpendicular toward

the top of the chamber. The flow lines indicated that the heat was causing a thermal plume effect. The next model was the human geometry on a plane representing a simplified litter.

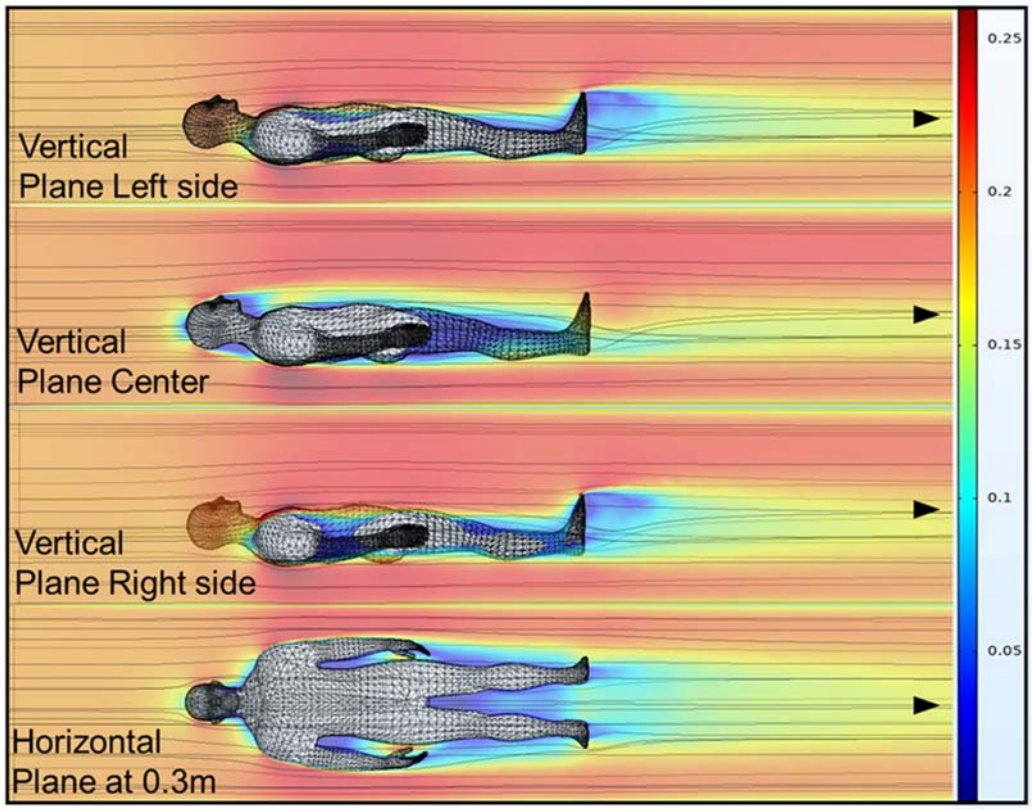

Figure 7. Human Geometry (arrow indicates direction of flow) with Flow Lines Across Four Planes in the Model, m/s.

The human geometry on a simplified litter is shown in Figure 9. The human geometry on litter showed similar pattern in slowing the velocity of the flow around the human form as the human geometry model. The slowed flow around the geometry had larger areas of slow flow between the arms and hands and the torso of the human geometry.

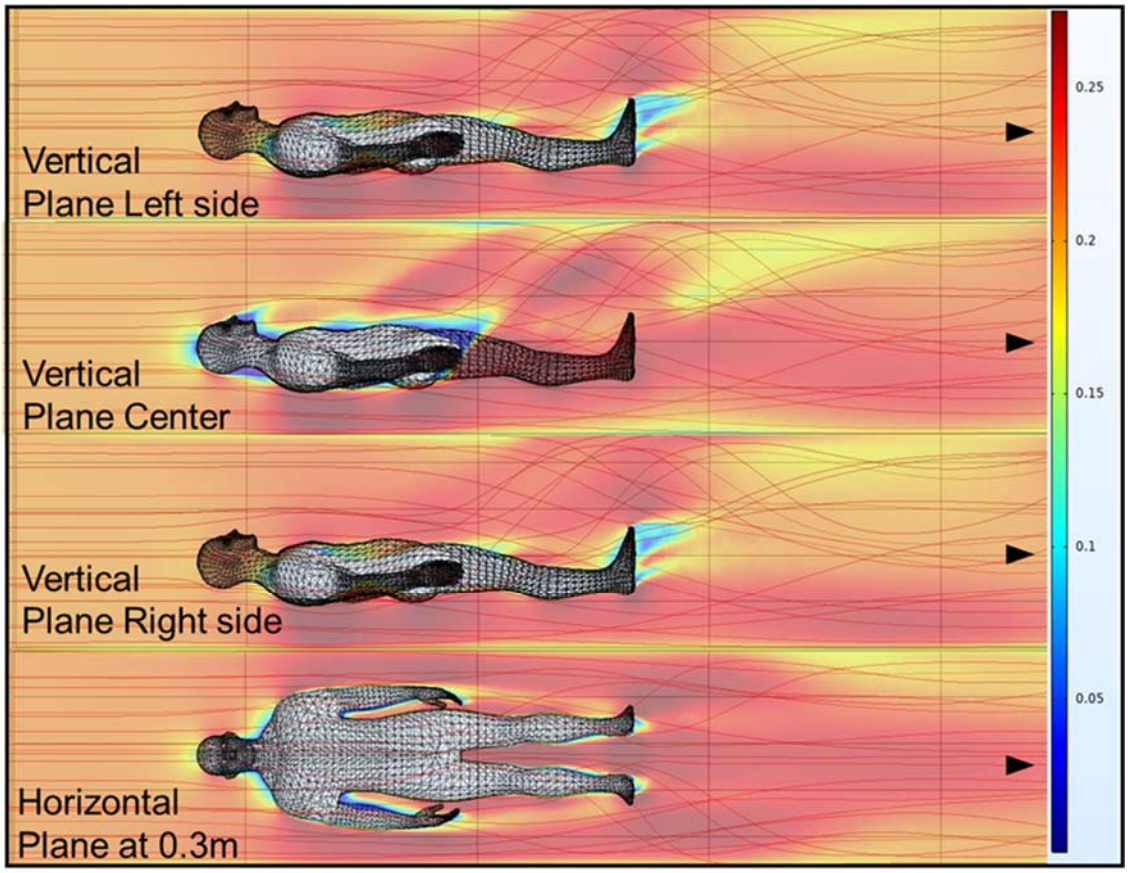

Figure 8. Human Geometry as a Heat Source (Arrows Indicate Direction of Flow) with Flow Lines Across Four Planes in the Model, m/s.

Each figure shows the described geometry, flow stream lines and scale indicating flow velocity. The heat scale for the heat model had to include all values above 0.265 m/s in the color for 0.265 to use the same scale as the other models. The heat model was used to generate a heat flux graph showing the predicted temperature gradient in the fluid flow, see Figure 10.

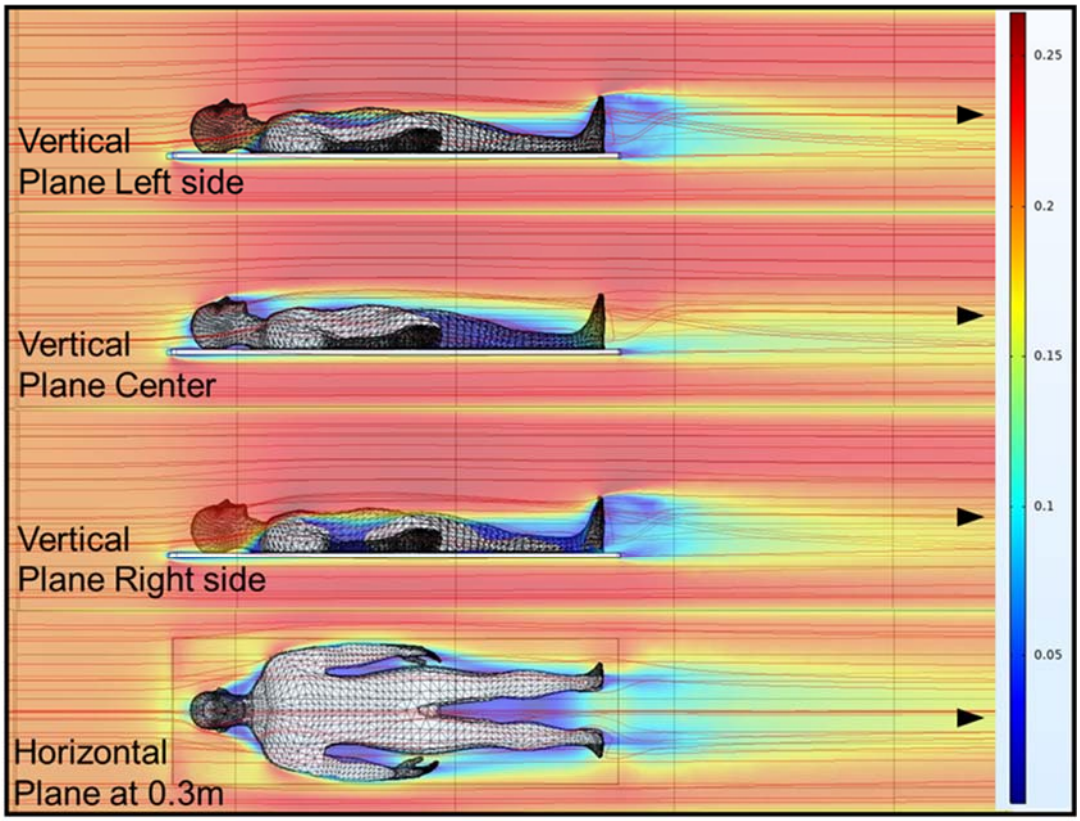

Figure 9. Human Geometry on a Simplified Litter (arrow indicates direction of flow) with Flow Lines Across Four planes in the Model, m/s.

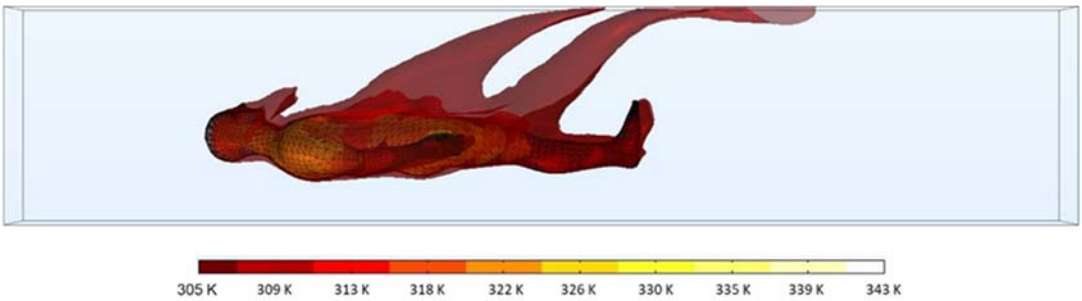

Figure 10. Heat Flux from Heated Human Geometry Model.

4.4.3 Experimental Results

The airflow measurements are presented in Tables 4-7 for chamber measurements without any experimental treatment at 0.20 m/s (Table 4), measurements with the litter and

assembly only at 0.20 m/s (Table 5), the litter assembly with manikin at 0.20m/s (Table 6), selected body locations and heated manikin at 0.20 m/s (Table 7), and selected positions with heated manikin at 0.20 m/s (Table 8). The data recorded for 0.50 m/s (30Hz fan setting) is presented in Appendix VI. The 0.50 m/s data was recorded because it was listed in the range of possible flows within a C-130. Because the airflow at the lower rear litter position had the largest inflight average of 0.29 m/s (Walsh, 1998). It was not likely that the airflow would be sustained at the 0.50 m/s velocity and thus did not warrant the effort, time, and resources to produce additional CFD models that would be of limited value based on the knowledge of the airflow environment within a C-130 during AE operations.

The data collected was analyzed in similar manner as described in Chapter III, Appendix II, and Appendix III by visually inspecting histogram and box plot for qualitative inspection of normality. The null hypothesis for the Shapiro-Wilk test is that the data being compared is from a normal distribution thus rejecting the null hypothesis means the data sets do not come from a normal distribution. The assumption of normally distributed data was checked using Shapiro-Wilk test with python scipy.stats module (Virtanen, 2020) and the results agreed that the p-value was much less than 0.05 for each chamber configuration. The null hypothesis of the Levene test is that data comes from populations that have equal variance. If we reject the null hypothesis then the data is believed to be from populations that do not have equal variance. The Levene test showed there was not equal variance between chamber configurations comparing the empty chamber, chamber with litter assembly and the chamber with the manikin on the litter.

Because the assumptions of normal distribution and equal variance could not be made non-parametric comparison had to be made. The null hypothesis for the Kruskal-Wallis test is that the median between groups is equal; rejecting the null hypothesis indicated that the median

between chamber configurations is not the same. The Kruskal-Wallis test indicated the data were from different distributions based on analysis of the median. The scipy.stats module (Scipy v1.5.2, 2020) returns a p-value for each test; even in cases such as Levene test that would compare a critical value with the test statistic so when reporting values from python you reject the null hypothesis when the p-value is less than the designated alpha value. In all cases alpha was set to 0.05 and the results are reported in Table 9. The results of the Kruskal-Wallis did not indicate which chamber configuration or configurations is different.

The Mann-Whitney U test is a nonparametric test with the null hypothesis being that the distributions of the populations being compared are equal; thus, if we reject the null hypothesis the distributions can be assumed to not be equal. The data collected during heated manikin trials was analyzed using the Mann-Whitney U test against the non-heated trials for each of the sampled positions and for the selected body locations. Significance was determined for all but 5 of the sampling positions, Table 10, and for all but one body location, Table 11.

The temperature was monitored using thermocouples taped to the surface of the manikin just downwind from the desired body location sampling point (chest, thigh, abs, forehead) with the tip of the probe orientated away from the filter bank. The range and average temperature values can be found in Table 12. At completion of wind speed measurement, a thermal image was taken to cross reference surface temperature, see Figure 11.

Table 4. Air Velocities for Positions at 0.20 m/s, empty chamber.

0.20 m/s Chamber Only	Right Side (0.304 m)		Center (0.457 m)		Left Side (0.609 m)	
Position	Mean (m/s)	Standard Deviation	Mean (m/s)	Standard Deviation	Mean (m/s)	Standard Deviation
H1	0.102	0.020	0.138	0.012	0.260	0.011
H2	0.187	0.010	0.219	0.017	0.247	0.007
H3	0.187	0.018	0.230	0.021	0.228	0.016
H4*	0.181	0.014	0.253	0.015	0.216	0.009
H5*	0.190	0.007	0.206	0.019	0.217	0.009
H6	0.180	0.007	0.211	0.011	0.193	0.010
H7*	0.176	0.007	0.208	0.010	0.176	0.007
H8*	0.166	0.007	0.208	0.007	0.200	0.011
H9*	0.158	0.007	0.173	0.014	0.173	0.005
H10**	0.154	0.005	0.172	0.007	0.170	0.007
B1	0.182	0.016	0.194	0.010	0.204	0.015
B2	0.153	0.007	0.177	0.009	0.207	0.011
B3	0.139	0.016	0.176	0.010	0.228	0.016
B4	0.151	0.008	0.197	0.013	0.219	0.008
B5	0.160	0.010	0.176	0.015	0.208	0.010
B6	0.152	0.012	0.187	0.009	0.189	0.008
B7	0.157	0.013	0.189	0.008	0.193	0.017
BA1	0.154	0.023	0.214	0.011	0.238	0.007
BA2	0.159	0.014	0.229	0.012	0.229	0.019
BA3	0.158	0.010	0.216	0.014	0.202	0.007
P1	0.148	0.010	0.182	0.011	0.169	0.006
P2	0.161	0.012	0.183	0.010	0.190	0.007
P3	0.184	0.016	0.189	0.008	0.179	0.008
P4	0.180	0.007	0.187	0.007	0.189	0.011
P5	0.171	0.009	0.184	0.005	0.182	0.007
P6	0.176	0.010	0.210	0.013	0.193	0.010
P7	0.163	0.005	0.204	0.005	0.200	0.009
P8	0.146	0.005	0.180	0.009	0.182	0.007

* Measurement locations at 0.457m is against the manikin head and has no measurement at 0.609m when manikin is in place.

** Measurement location with manikin in place passes under the manikin's neck.

Table 5. Air Velocities Around Litter and Assembly at 0.20 m/s, No Manikin.

0.20 m/s Litter assembly only	Right Side (0.304 m)		Center (0.457 m)		Left Side (0.609 m)	
Position	Mean (m/s)	Standard Deviation	Mean (m/s)	Standard Deviation	Mean (m/s)	Standard Deviation
H1	0.212	0.016	0.078	0.022	0.191	0.012
H2	0.278	0.016	0.262	0.022	0.263	0.019
H3	0.242	0.012	0.213	0.030	0.262	0.016
H4*	0.222	0.007	0.291	0.024	0.282	0.007
H5*	0.224	0.012	0.266	0.009	0.253	0.014
H6	0.178	0.007	0.248	0.022	0.250	0.009
H7*	0.191	0.009	0.249	0.018	0.246	0.017
H8*	0.189	0.011	0.246	0.020	0.240	0.007
H9*	0.189	0.003	0.194	0.005	0.237	0.012
H10**	0.152	0.017	0.166	0.015	0.211	0.015
B1	0.197	0.011	0.189	0.014	0.228	0.007
B2	0.180	0.017	0.202	0.017	0.218	0.007
B3	0.180	0.017	0.143	0.023	0.210	0.022
B4	0.192	0.019	0.193	0.015	0.218	0.008
B5	0.190	0.013	0.202	0.011	0.220	0.007
B6	0.173	0.010	0.193	0.009	0.209	0.008
B7	0.189	0.011	0.191	0.009	0.210	0.007
BA1	0.242	0.012	0.210	0.020	0.241	0.009
BA2	0.197	0.009	0.189	0.018	0.222	0.010
BA3	0.188	0.012	0.194	0.021	0.201	0.012
P1	0.192	0.016	0.197	0.011	0.201	0.006
P2	0.201	0.011	0.201	0.011	0.213	0.005
P3	0.189	0.011	0.199	0.008	0.200	0.007
P4	0.189	0.012	0.200	0.005	0.201	0.008
P5	0.190	0.009	0.168	0.014	0.190	0.010
P6	0.220	0.007	0.170	0.013	0.137	0.013
P7	0.193	0.012	0.189	0.014	0.196	0.010
P8	0.191	0.011	0.170	0.010	0.179	0.008
* Measurement locations at 0.457m is against the manikin head and has no measurement at 0.609m when manikin is in place.						
** Measurement location with manikin in place passes under the manikin's neck.						

Table 6. Air Velocities at Positions Around Litter Assembly with Manikin at 0.20 m/s.

0.20 m/s Manikin, No Heat	Right Side (0.304 m)		Center (0.457 m) *		Left Side (0.609 m)	
Position	Mean (m/s)	Standard Deviation	Mean (m/s)	Standard Deviation	Mean (m/s)	Standard Deviation
H1	0.200	0.015	0.140	0.039	0.240	0.017
H2	0.234	0.045	0.289	0.036	0.271	0.024
H3	0.233	0.032	0.218	0.047	0.262	0.021
H4*	0.227	0.028	0.248	0.034	-	-
H5*	0.210	0.029	0.026	0.026	-	-
H6	0.177	0.012	0.076	0.063	0.261	0.025
H7*	0.182	0.027	0.291	0.100	-	-
H8*	0.157	0.045	0.239	0.120	-	-
H9*	0.177	0.019	0.153	0.032	-	-
H10**	0.119	0.037	0.006	0.005	0.200	0.044
B1	0.216	0.011	0.206	0.011	0.260	0.007
B2	0.219	0.018	0.212	0.010	0.252	0.008
B3	0.253	0.016	0.217	0.011	0.246	0.017
B4	0.229	0.011	0.197	0.005	0.244	0.013
B5	0.210	0.010	0.206	0.010	0.243	0.009
B6	0.186	0.025	0.200	0.016	0.218	0.011
B7	0.073	0.017	0.101	0.043	0.201	0.013
BA1	0.147	0.017	0.163	0.017	0.282	0.010
BA2	0.146	0.011	0.221	0.015	0.251	0.011
BA3	0.101	0.023	0.160	0.010	0.237	0.018
P1	0.236	0.040	0.231	0.023	0.210	0.020
P2	0.237	0.019	0.261	0.015	0.202	0.030
P3	0.209	0.019	0.242	0.062	0.203	0.026
P4	0.183	0.027	0.188	0.082	0.182	0.067
P5	0.141	0.036	0.148	0.080	0.153	0.010
P6	0.144	0.013	0.142	0.048	0.131	0.019
P7	0.147	0.013	0.180	0.021	0.182	0.025
P8	0.156	0.018	0.171	0.012	0.181	0.016
* Measurement locations at 0.457m is against the manikin head and has no measurement at 0.609m when manikin is in place.						
** Measurement location with manikin in place passes under the manikin's neck.						

Table 7. Air Velocities at Positions Around Heated Manikin at 0.20 m/s.

0.20 m/s Heated Manikin Positions	Right Side (0.304m)		Center (0.457m)		Left Side (0.609m)	
Position	Mean (m/s)	Std Dev	Mean (m/s)	Std Dev	Mean (m/s)	Std Dev
BA1	0.24	0.017	0.17	0.010	0.26	0.007
BA2	0.24	0.018	0.19	0.011	0.22	0.015
BA3	0.16	0.014	0.18	0.008	0.20	0.009
P1	0.20	0.011	0.19	0.006	0.23	0.008
P2	0.21	0.005	0.20	0.010	0.22	0.005
P3	0.21	0.007	0.24	0.010	0.23	0.007
P4	0.24	0.012	0.26	0.007	0.26	0.005
P5	0.13	0.014	0.06	0.013	0.18	0.011
P6	0.25	0.013	0.21	0.014	0.16	0.013
P7	0.17	0.015	0.22	0.020	0.18	0.023
P8	0.12	0.024	0.11	0.022	0.11	0.038

Table 8. Air Velocity at Selected Manikin Locations and Sampled Heated Manikin Locations at 0.20 m/s.

0.20 m/s Manikin	Mean (m/s)	Std Dev	0.20 m/s Heated Manikin	Mean (m/s)	Std Dev
Forehead	0.146	0.017			
Chin	0.017	0.009			
Nose	0.156	0.032			
Head, Top	0.008	0.004			
Chest, Left	0.100	0.016	Chest, Left	0.075	0.020
Chest, Right	0.130	0.012	Chest, Right	0.047	0.009
Abs/Hips, Center	0.124	0.007	Abs/Hips, Center	0.098	0.015
Thigh, Left	0.059	0.019	Thigh, Left	0.063	0.017
Thigh, Right	0.024	0.010	Thigh, Right	0.015	0.005

Table 9. Comparison of Chamber Configurations for Normal Distribution, Equal Variance and Population Distribution.

	Shapiro-Wilk (Normality)		Levene (Equal Variance)		Kruskal-Wallis (Sample Distribution)	
	Test Statistic	p-value	Test Statistic	p-value	Test Statistic	p-value
Chamber	0.982	p = 4E-8	175.05	p = 2.57E-71	107.02	p = 5.8E-24
Manikin	0.965	p = 6E-12				
Litter Assembly	0.958	p = 7E-14				

Table 10. Air Velocity at Heated Positions Compared to Unheated Positions, Mann-Whitney U Test (Bold Indicates no Significance).

Positions											
Right Side (0.304 m)				Center (0.457 m)				Left Side (0.609 m)			
	Manikin	Heated Manikin			Manikin	Heated Manikin			Manikin	Heated Manikin	
	Median		p-value		Median		p-value		Median		p-value
BA1	0.14	0.24	p=0.000170	BA1	0.16	0.17	p=0.00117	BA1	0.28	0.26	p=0.000219
BA2	0.15	0.23	p=0.000174	BA2	0.22	0.19	p=0.000469	BA2	0.25	0.21	p=0.000613
BA3	0.11	0.16	p=0.000189	BA3	0.16	0.18	p=0.000691	BA3	0.23	0.20	p=0.000284
P1	0.25	0.20	p=0.0220	P1	0.22	0.19	p=0.000177	P1	0.22	0.23	p=0.00966
P2	0.24	0.21	p=0.00339	P2	0.26	0.20	p=0.000179	P2	0.21	0.22	**p=0.115**
P3	0.21	0.21	**p=0.355**	P3	0.27	0.24	**p=0.123**	P3	0.22	0.23	p=0.00409
P4	0.19	0.23	p=0.000218	P4	0.23	0.26	p=0.00193	P4	0.22	0.26	p=0.000154
P5	0.13	0.13	**p=0.428**	P5	0.12	0.06	p=0.000666	P5	0.15	0.18	p=0.00112
P6	0.14	0.24	p=0.000185	P6	0.12	0.21	p=0.00609	P6	0.13	0.16	p=0.000755
P7	0.15	0.17	p=0.00169	P7	0.17	0.21	p=0.00120	P7	0.20	0.17	**p=0.464**
P8	0.15	0.12	p=0.00117	P8	0.17	0.10	p=0.000186	P8	0.18	0.12	p=0.000277

Table 11. Heated Body Locations Post Hoc Mann-Whitney U Test

Body Locations	Test Statistic	p-value
Chest, Left	15.5	p=0.00463
Chest, Right	0	p=0.0000746
Abs/Center	0	p=0.0000574
Thigh, Left	42.5	**p=0.294**
Thigh, Right	22.5	p=0.0115

Table 12. Surface Temperatures During Sampling.

	0.20 m/s Experiment	Abs	Thigh, Left	Chest, Left	Forehead
Average Temp C	33.3	33.8	32.2	33.9	33.3
Range	31.7-36.6	32.7-35.2	31.7-32.7	32.4-36.6	31.9-35.8

Figure 11. Thermal Image Post Airflow Measurement.

4.4 Comparison of Experimental and Computational Data

The results from the models were compared by using the coordinates for sampling positions to create probes within the model at each corresponding insertion depth; the probes would report velocity in downwind direction. The results for each sampling location in each model are presented in Table 13 and14, for sampling depth 0.304 m (Right Side), 0.457 m (Center) and 0.609m (Left Side) respectively. The heated positions and locations were evaluated in the same manner. The heated locations are compared on table 15. The heated sampling positions are in Table 16. A swarm plot with the heated and unheated experimental positions compared to the modeled values for human geometry on a litter and heated human geometry can be seen in Figure 12. The comparison of experimental and modeled heat positions can be seen in Figure 13, where the mean with 95% confidence interval is compared to the calculated value from the models.

The unheated manikin and models with human geometry and human geometry on simplified litter were compared to determine the relative agreement between measured and modeled values. The measured value was taken at $\pm$ 25%, $\pm$ 10% and $\pm$ 3% (reflecting the hotwire anemometer's measurement accuracy) and compared to each value reported by the probe in the model. There was a total of 75 sample locations compared because of the location of the head sampling positions resulted in no measurements for the left side (0.609 m) and 4 probes were inside the head geometry at the center (0.457 m) positions. The human geometry had 58 of 75 positions within 25%, 32 of those 58 positions were with 10% and 10 of those 32 positions (right side: P1, P2, P7, and P8, center: H3 and P1, left side: H10, B4, B5, and BA3) were within $\pm$ 3%. The human geometry on litter model had 54 of 75 positions within 25%, of those

positions 33 were with 10% and 8 of those positions (right side: P1and P2, center: B2 and P3, left side: B4, B5 and B7) were within ± 3%.

The modeled heated geometry and heated manikin data generally showed an increase in the velocity at the 11 positions measured during modeling and experimental data collection at each of the insertion depths. The measured data did not appear to show a trend however 18 of the 33 positions had higher average air velocity and the modeled data had 26 of 33 positions with higher velocities when measured during heating. Of the positions modeled compared to the heated manikin 24 of 33 are within ± 25% of the average air velocity. From the 24 positions within ± 25%, seven were within ± 10% and one (left side P2) was within the threshold of ± 3%.

Slow velocities were measured on the unheated manikin surface at the chin and top of the head were mirrored in the modeled data, reflecting the boundary layer around the manikin and sufficiently small to not compare further. The measured data shows that there is poor agreement between the model at both thighs and the center of the abs/hips locations. The locations that showed good agreement between the models and measured data for the human geometry was the forehead (± 25%), nose (± 25%), and right chest (±10%). The human geometry on the litter also showed good agreement at the forehead (±10%) and right chest (±3%). The heated manikin locations and model did not show good agreement with all of the measured values being less than 0.1 m/s and only the abs/hips location on the human geometry being less than 0.11m/s.

Table 13. Comparison Between Experimental and Modeled Air Velocity in Direction of Flow Results at Right Side and Center, in m/s.

Right Side (0.304 m)				Center (0.457 m)			
	Experimental Manikin on Litter (m/s)	Model Human Geometry (m/s)	Model Human Geometry on Litter (m/s)		Experimental Manikin on Litter (m/s)	Model Human Geometry (m/s)	Model Human Geometry on Litter (m/s)
H1	0.200	0.217	0.220	H1	0.140	0.217	0.221
H2	0.234	0.213	0.218	H2	0.289	0.216	0.222
H3	0.233	0.220	0.225	H3	0.218	0.222	0.229
H4*	0.227	0.213	0.219	H4*	0.248	0.227	0.234
H5*	0.210	0.218	0.225	H5*	0.026	0.023	0.027
H6	0.177	0.203	0.207	H6	0.076	0.125	0.138
H7*	0.182	0.213	0.220	H7*	0.291	-	-
H8*	0.157	0.209	0.221	H8*	0.239	-	-
H9*	0.177	0.211	0.219	H9*	0.153	-	-
H10**	0.119	0.201	0.219	H10**	0.006	-	-
B1	0.216	0.237	0.239	B1	0.206	0.237	0.239
B2	0.219	0.239	0.241	B2	0.212	0.240	0.241
B3	0.253	0.234	0.236	B3	0.217	0.234	0.236
B4	0.229	0.239	0.241	B4	0.197	0.239	0.241
B5	0.210	0.241	0.243	B5	0.206	0.239	0.242
B6	0.186	0.234	0.238	B6	0.200	0.230	0.236
B7	0.073	0.223	0.214	B7	0.101	0.151	0.149
BA1	0.147	0.242	0.243	BA1	0.163	0.189	0.212
BA2	0.146	0.239	0.241	BA2	0.221	0.193	0.215
BA3	0.101	0.244	0.245	BA3	0.160	0.192	0.215
P1	0.236	0.239	0.243	P1	0.231	0.236	0.241
P2	0.237	0.237	0.239	P2	0.261	0.234	0.238
P3	0.209	0.232	0.234	P3	0.242	0.231	0.235
P4	0.183	0.229	0.231	P4	0.188	0.230	0.233
P5	0.141	0.088	0.060	P5	0.148	0.189	0.190
P6	0.144	0.102	0.088	P6	0.142	0.178	0.179
P7	0.147	0.142	0.137	P7	0.180	0.165	0.163
P8	0.156	0.157	0.158	P8	0.171	0.161	0.159
* Measurement locations that 18" is against the manikin head and has no measurement at 24" when manikin is in place							
** Measurement location with manikin in place passes under the manikin's neck.							

Table 14. Comparison Between Experimental and Modeled Air Velocity in Direction of Flow Results at Left Side, in m/s.

Left Side (0.609 m)			
	Experimental Manikin on Litter (m/s)	Model Human Geometry (m/s)	Model Human Geometry on Litter (m/s)
H1	0.240	0.217	0.220
H2	0.271	0.214	0.218
H3	0.262	0.220	0.225
H4*	-	0.214	0.220
H5*	-	0.218	0.225
H6	0.261	0.202	0.206
H7*	-	0.215	0.222
H8*	-	0.209	0.222
H9*	-	0.213	0.221
H10**	0.200	0.201	0.220
B1	0.260	0.237	0.239
B2	0.252	0.239	0.241
B3	0.246	0.234	0.236
B4	0.244	0.239	0.241
B5	0.243	0.241	0.243
B6	0.218	0.234	0.238
B7	0.201	0.216	0.206
BA1	0.282	0.242	0.243
BA2	0.251	0.240	0.242
BA3	0.237	0.243	0.245
P1	0.210	0.239	0.243
P2	0.202	0.236	0.239
P3	0.203	0.231	0.234
P4	0.182	0.228	0.231
P5	0.153	0.080	0.064
P6	0.131	0.094	0.086
P7	0.182	0.136	0.131
P8	0.181	0.152	0.152
* Measurement locations that 18" is against the manikin head and has no measurement at 24" when manikin is in place			
** Measurement location with manikin in place passes under the manikin's neck.			

Table 15. Comparison Between Experimental and Modeled Air Velocity in Direction of Flow Results between Heated and Unheated Locations, in m/s.

0.20 m/s	Experimental Manikin Mean (m/s)	Model Human Geometry (m/s)	Model Litter & Human Geometry (m/s)	0.20 m/s Heat	Experimental Manikin Mean (m/s)	Model Human Geometry Heat Model
Forehead	0.146	0.117	0.143	Chest, Left	0.075	0.173
Chin	0.017	0.006	0.009	Chest, Right	0.047	0.146
Nose	0.156	0.18	0.206	Abs/Hips, Center	0.098	0.056
Head, Top	0.008	0.031	0.03	Thigh, Left	0.063	0.139
Chest, Left	0.1	0.161	0.152	Thigh, Right	0.015	0.114
Chest, Right	0.13	0.137	0.126			
Abs/Hips, Center	0.124	0.07	0.073			
Thigh, Left	0.059	0.144	0.133			
Thigh, Right	0.024	0.152	0.138			

Table 16. Comparison Between Experimental and Modeled Air Velocity in Direction of Flow Results between Heated and Unheated Positions, in m/s.

Right Side (0.304 m)			Center (0.457m)			Left Side (0.609 m)		
Position	Experiment Heated Manikin (m/s)	Model Heated Human Geometry (m/s)	Position	Experiment Heated Manikin (m/s)	Model Heated Human Geometry (m/s)	Position	Experiment Heated Manikin (m/s)	Model Heated Human Geometry (m/s)
BA1	0.243	0.235	BA1	0.168	0.207	BA1	0.258	0.236
BA2	0.236	0.238	BA2	0.190	0.237	BA2	0.218	0.237
BA3	0.159	0.246	BA3	0.182	0.221	BA3	0.199	0.246
P1	0.199	0.264	P1	0.189	0.238	P1	0.229	0.258
P2	0.214	0.227	P2	0.200	0.174	P2	0.223	0.221
P3	0.213	0.197	P3	0.242	0.186	P3	0.228	0.194
P4	0.237	0.191	P4	0.257	0.208	P4	0.256	0.192
P5	0.127	0.221	P5	0.061	0.254	P5	0.176	0.225
P6	0.246	0.185	P6	0.206	0.252	P6	0.162	0.185
P7	0.172	0.211	P7	0.221	0.244	P7	0.179	0.203
P8	0.117	0.214	P8	0.107	0.238	P8	0.106	0.205

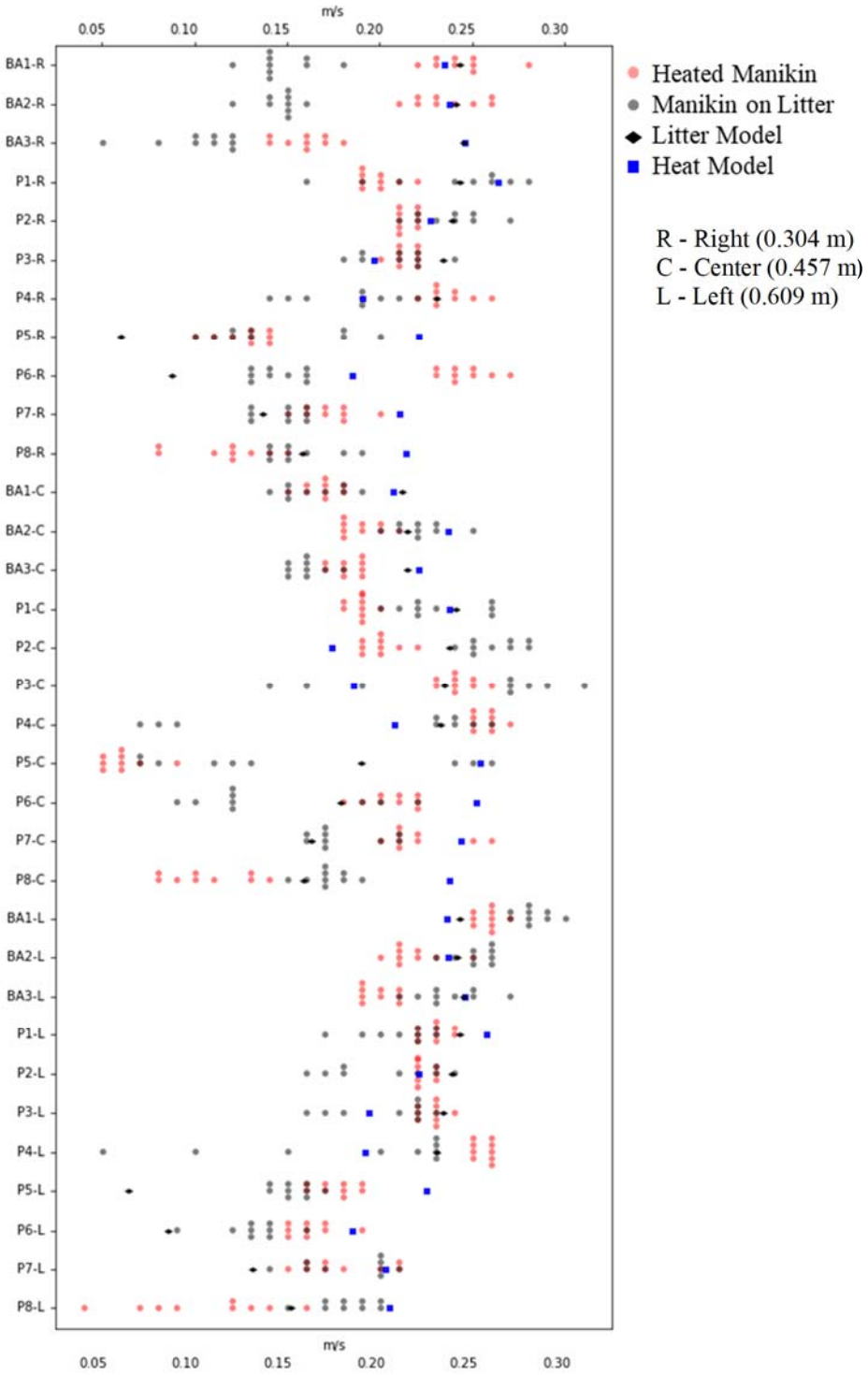

Figure 12. Swarm Plot of Heated and Unheated Positions Compared to Litter and Heat Models, in m/s.

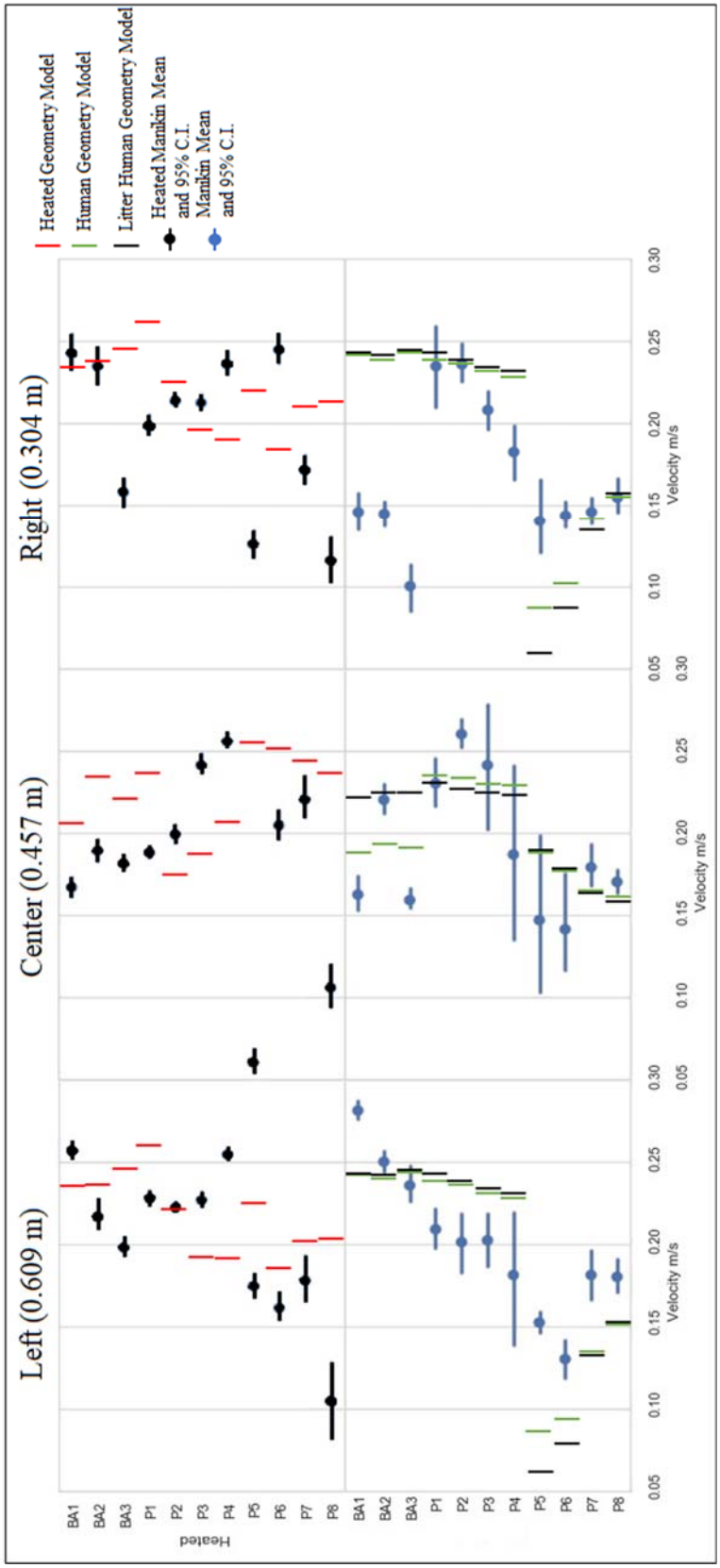

Figure 13. Heated and Unheated Average Velocity with 95% Confidence Interval Compared to Modeled Values, in m/s.

4.5. Discussion

The unheated models showed between 10-13% of the sample positions matched the measured hot wire anemometer readings. There was not a lot of difference between velocities in the models which should be expected because the inputs are the same with the only difference being the geometry or heat transfer. The difference in calculated velocities should be directly related to the litter or heat added to the model. The velocity was higher in all but 12 probe positions when the litter to the human geometry models are compared; indicating the air velocity increased at more positions with the litter model.

When the manikin is compared to a modeled geometry the body locations can indicate whether the manikin and geometry are representative of each other if they are in agreement when flow velocities are compared. When the values are not similar the geometries should be considered not to be representative of each other because the boundary layers will be in different locations. Only one location on the human geometry ($\pm$10%) and for human on litter geometry ($\pm$3%) showed agreement, right chest, with locations sampled during heating. Because none of the heated locations were in agreement and only one unheated body location was in agreement the geometry should be refined if measurements near the manikin or geometry surface will be considered.

When comparing the sampling positions the general human shape impacted the flow around the manikin or geometry when the flow velocity is measured. Since there is reasonable agreement from the measured and modeled positions without heat the manikin and human geometry had less impact at the whole chamber scale than measured near the surface. The heated positions showed less agreement between the modeled and experimental values.

The model reflects that the thermal plume from a modeled human geometry changed the airflow around the geometry within the chamber. The flow lines indicate that the thermal plume does impact the velocity downwind from the patient differently than the litter or just the human geometry. The statistical analysis showed the heated and unheated measurements from the same position to be significantly different for most of the 'BA' and 'P' positions. The heated experimental trial showed that further work examining the effect of heat on particle transport should investigated in the MURPHEE aerosol chamber.

The particle transport in a C-130 and within all aircraft considered for AE should be further studied. The general droplet precautions prescribed do not differentiate between aerosols and droplets but state that particles of 5 μm will not travel greater than 3 feet (US Department of the Air Force, 2017). Considering certain aspects of aerosols, droplet evaporation and particle terminal settling velocity at a minimum (Hinds, 1999) and reported particle transport inside a C-130E with bacterial spores and smoke reaching the flight deck (Clayton, 1976) the general precautions should be further refined based on a detailed airflow characterization and particle transport within a C-130 during AE operations. The impact of AE configuration should be considered as it determines the number of patients (US Department of the Air Force, 2009) which could be represented by heated manikins to measure patient heat load on particle transport.

The heated manikin and heated human geometry model both agreed that the airflow velocity increased downstream from the heated human form. Increased velocity of the airflow will impact aerosols generated by infectious patients and the off gassing from CBRN casualties. Aerosols that are sufficiently small will become entrained in the bulk flow and be transported from the patient throughout the aircraft. Because of the complex nature of turbulent flow, the

assumptions that can be drawn are limited without modeling and experimentation. The low relative humidity will reduce the particle size from water vapor or droplets in an AE environment on board a C-130. Smaller particles can become entrained in airflows facilitating transport and possible infection or cross contamination. Higher airflow velocities, after being heated from a manikin or patient, can be expected to transport particles further in the direction of the bulk flow and has the potential to entrain larger particles.

V. Conclusion and Recommendations

The C-130 cargo environment airflow is not expected to act like the MURPHEE chamber but it is sufficient to simulate the airflow around a simulated patient on a litter. The lower rear litter position, based on the available data, most closely resembled the experimental setup as reported during measuring the thermal environment (Walsh, 1998). The orientation of the patient was based on the bulk flow traveling head to toe across the patient assuming no other obstructions in flow aside from the human form and the litter. This is based on the descriptions of the airflow within an aircraft as turbulent based on smoke tests (Clayton, 1976) and The flow in a C-130 is expected to be similar to other aircraft in that the flow from top to bottom will follow the shape of the skin of the aircraft creating a circular flow internal to the aircraft (Withers, 2000) and are clearly not present in the MURPHEE Chamber.

There is a clear gap in information regarding the airflow and possible contaminant transport within a C-130 in part because of the different modifications to the airframe since first production and how each change impacts the flow within the aircraft. The major changes impacting the airflow characteristic is making the aircraft longer (Martin, 2013) and the engines being replaced with new models that introduce more air into the conditioned air and heat

systems. Adding to the gap is not reliably knowing the configuration of the aircraft's air conditioning systems and if that data can be applied from one C-130 to another of the same model let alone between model of aircraft (Roy, 1975; Matulich, 1991; Roy, 1976; Wood, 1989).

5.1 Conclusion of Research

The fan from the exposure chamber supplied a constant flow condition to measure the airflow around and downstream from a simulated patient. The data shows that the human form on a litter impacts the airflow downstream. The sampled data indicates that each of the configurations with a patient or just a litter do not exhibit normal distribution or equal variance which seems to be a characteristic of the airflow in the chamber itself. It should be noted that the stretcher used had a mesh-like fabric, such that you could see through the weave of the fabric and had the support brackets attached underneath. The litter also had a bar that fixed the litter in the unfolded position below the litter that would impact the airflow below the litter and was largely the reason for not sampling below the litter. This could inform choosing litter configurations for AE operations and the type of litter if the type of litter and fabric impact the airflow around them. The litter was represented in the model as a solid plane thus a solid object not porous like the litter used.

The results of the Mann-Whitney U test showed significance between most heated locations on the manikin surface and also the sampling positions just above and downwind from the manikin. The heat is creating an altered flow condition caused by the thermal plume around the manikin and produced a measurable difference in flow velocity. The data from the heated manikin experimental trials showed average increase in air velocity of 4% when compared to the unheated experiment across all positions (BA1-3 and P1-8). From the heated positions 18

showed an increase in air velocity, 14 showed a decrease in velocity and one was the same. The average increase in velocity was 24% and the average decrease was 22% when compared to unheated positions. The experimental results indicated that the investigative question regarding thermal plume slowing the airflow was incorrect based on the velocity increasing by 4% when compared to the manikin alone. The average increase or decrease air velocity demonstrated that the heated manikin created a more dynamic impact on air velocity then increasing airflow velocity by 4% across all positions. This indicated that studying the effect of the thermal plume from a litter bound patient is worth further study to measure its impact on particle transport during C-130 AE operations.

Computational Fluid Dynamics can solve complex fluid flow problems but require experimental validation to measure the overall usefulness of the simulated conditions. A variety of conditions were modeled with airflow around human geometry and human geometry on a simplified litter showing the best agreement with experimental data. The heated model showed the least agreement with the measured data but the human geometry need more refinement to better resemble the manikin. The 2-D models were not time intensive and provided predictive value that heat would impact the airflow. The 3-D models when compared to the experimental data showed that the heated model and heated manikin impact the airflow in the MURPHEE aerosol chamber.

5.2. Study Limitations

Some limitations of the experiment are the lack of comparison studies but sampling position B4 was placed at the location previously described for taking ambient temperatures and airflow measurements (Walsh, 1998). The chamber is designed to provide consistent but

turbulent flow making it a much more controlled environment than one inside a C-130. The chamber also lacks the ability to hold more than one litter easily other than in an inline position limiting the ability to study effects of a pallet of litters.

This study did not focus on actual particle transport by generating aerosols and measuring deposition or exposure within the chamber. Additionally, the modeling did not include particle tracing. The use of an aerosol generating device such as rotating brush generator as described in Chapter III could be used to investigate the effects of heating and particle deposition on to a manikin or measure the assumption that a mask would not be required outside of 10 feet of an infectious patient (US Department of the Air Force, 2017). Further characterization of the chamber would be required to investigate at lower windspeeds as reported in other work (Walsh, 1998).

The ambient conditions during data collection were drastically different than those used during development of the heated manikin. The chamber location is not climate controlled during the summer making the ambient temperature a factor when conducting experiments. The temperature averaged 29.4° C during data collection putting it in the range of skin temperatures collected during the characterization of the thermal environment in a C-130 (Walsh, 1998). The characterization of the heat generated on the surface of the manikin was performed at about 73° F (~23.7° C) and could retain temperature within the desired range for at least 20 minutes after warming up to the minimum temperature desired of 29° C. The heated manikin performed as desired but the design could be improved to deliver more uniform heat throughout the body and extremities.

CFD software makes solving complex fluid problems more accessible but requires a lot of time to compute the solution especially as complexity of the problem grows. The mesh for

each 3-D model did not go beyond coarse and resulted in mesh elements with poor quality and adjacent to short faces. The models would benefit from more refined meshing and additional geometry refinement. That said, the poor-quality elements did not result in a failure to mesh all domains or to solve the fluid flow problem thus the models were deemed acceptable.

The manikin was a fashion manikin and not a research manikin with desired anthropomorphic characteristics or built in sensors or sampling apparatus. The manikin can best be described as tall and thin and has a rigid posture so it does not mold or lay flat on a surface allowing air to flow under the back and legs where it would not be able to flow on an actual stretcher bound patient.

5.3 Sources of Uncertainty

One of the largest sources of error is likely the orientation and placement of the hotwire anemometer. The hot wire anemometer used for measurements has a probe that allows for a 90° bend when sampling. While it was not loose at the pivot point it did not lock into position and would need periodic readjustment. The probe was inserted at each position on a telescoping rod with measurement in inches but it was difficult to ensure that it aligned identically for each measurement between the pivot point and not rotating the handle to misalign the probe. For future work it is recommended to use anemometers that can be fixed in place with fewer total sampling locations and consider using measuring devices capable of measuring the velocity field in all 3 dimensions.

The heated manikin could be better characterized with a better understanding of the range of temperatures it can reach and maintain based on ambient conditions in the chamber, but also to increase the circulation within the manikin itself or to add localized heat at specific wattage to

better resemble a desired temperature distribution on the surface of the manikin. The manikin used was made of plastic and for certain studies that surface may not be ideal or representative of human skin for surface roughness or other physical characteristics of plastic.

The chamber is much smaller and square instead of round like a C-130 cargo bay. The chamber is a confining space best shown in Figure 10, the heat from the heated human geometry reaches the top of the chamber when in a C-130 it would be an open boundary or another litter. The chamber is limited to ambient conditions as such desired temperature conditions may not be present year-round.

The simplified models add uncertainty because characteristics are lost such as the litter fabric being a mesh weave instead of a solid plane as depicted in the model geometry. All of the litter brackets were not modeled that paired with the fabric could produce much slower air velocities below the litter from turbulent mixing. The heat model appeared to generate surface temperatures greater than those of the manikin and found on the human body.

Bibliography

Arinami, Y., Akabayashi, S. I., Mizutani, K., & Sakaguchi, J. Airflow Distribution Measurements around the Human Body Using a Thermal Manikin by Particle Image Velocimetry. Journal of Flow Control, Measurement & Visualization, 5(3), pp 65-72. (2017).

Church, A.M.U. USAF & USSF Almanac 2020 Weapons & Platforms. Air Force Magazine, 110(6), 146. (2020). https://www.airforcemag.com/app/uploads/2020/06/Weapons.pdf [Accessed 29 July 2020]

Cignoni, P., Callieri, M., Corsini, M., Dellepiane, M., Ganovelli, F., Ranzuglia, G. MeshLab: An Open-Source Mesh Processing Tool Sixth Eurographics Italian Chapter Conference, pp 129-136, (2008).

Clayton, A. J., O'Connell, D. C., Gaunt, R. A., & Clarke, R. E. Study of the Microbiological Environment within Long-and Medium-Range Canadian Forces Aircraft. Aviation, Space, and Environmental Medicine, 47(5), pp 471-482. (1976).

COMSOL Multiphysics® 5.4 Heat Transfer Module User's Guide. 2018.

COMSOL Multiphysics® 5.4 CFD Module User's Guide. 2018.

COMSOL Multiphysics® 5.4 Material Library User's Guide. 2018.

Duran, C., & Reilly, D. Computational Airflow Models to Evaluate Biological Agent Transport in Cargo Aircraft. 711 HPW/RHM (AFRL-RH-WP-TR-2019-0085) Wright-Patterson, AFB United States. (2019).

Engineering Toolbox. Ratios of specific heat for gases in constant pressure and volume processes https://www.engineeringtoolbox.com/specific-heat-ratio-d_608.html. [Accessed on: 28 July 2020]

Gordon, C. C., Blackwell, C. L., Bradtmiller, B., Parham, J. L., Barrientos, P., Paquette, S. P., ... & Mucher, M. 2012 Anthropometric Survey of US Army Personnel: Methods and Summary Statistics. Army Natick Soldier Research Development and Engineering Center MA. (2014).

Gothäll, H., How to Inspect Your Mesh in COMSOL Multiphysics® COMSOL Blog. https://www.comsol.com/blogs/how-to-inspect-your-mesh-in-comsol-multiphysics/ (2017). [Accessed on: 1 Aug 2020]

Hinds, W., C. Aerosol Technology: Properties, Behavior, and Measurement of Airborne Particles, 2nd Ed. New York, NY: John Wiley & Sons. (1999).

Kelly, G. Body temperature variability (Part 1): a review of the history of body temperature and its variability due to site selection, biological rhythms, fitness, and aging. Alternative medicine review, 11(4). (2006).

Lake, W., Schulze, P., & Gougelet, R. Guidelines for Mass Casualty Decontamination During a HAZMAT/Weapon of Mass Destruction Incident. Volumes 1 and 2 (No. ECBC-SP-024). Edgewood Chemical Biological Center Aberdeen Proving Ground, MD. (2009).

Li, J., Yavuz, I., Celik, I., & Guffey, S. Predicting Worker Exposure—the Effect of Ventilation Velocity, Free-Stream Turbulence and Thermal Condition. Journal of Occupational and Environmental Hygiene, 4(11), pp 864-874. (2007).

Liu, J., Wang, H., & Wen, W. Numerical Simulation on a Horizontal Airflow for Airborne Particles Control in Hospital Operating Room. Building and Environment, 44(11), pp 2284-2289. (2009).

Martin, L. C-130J Super Hercules. Whatever the Situation, We'll be There. https://www.lockheedmartin.com/content/dam/lockheed-martin/aero/documents/C-130J/C130JPocketGuide.pdf, (2013). [Accessed on: 8 Aug 2020]

Matulich, D., & Finstad, R. Evolutionary Upgrade and Application of the C-130H Simple-Cycle Refrigeration System. SAE Transactions, pp 1283-1293. (1991).

NATO. NATO Standard AMedP-2.1, Stretchers, Bear Brackets and Attachment Supports. North Atlantic Treaty Organization NATO Standardization Agency, pp 1-22. (2013).

Roy, J., V. Hercules Air Conditioning. Service News: Vol. 3 No. 2 April-June, pp 2. (1976).

Roy, J., V. Lockheed Aircraft Serial Numbers. Service News: Volume 2, no. 2, April-June, pp 19. (1975).

Scipy v1.5.2 Reference Guide. Statistical Functions https://docs.scipy.org/doc/scipy/reference/generated/scipy.stats.levene.html#scipy.stats.levene. [Accessed 4 Aug 2020]

TurboSquid – www.turbosquid.com/3d-models/free-obj-model-realistic-white-male-female/1094197. [Accessed: 17 July 2020]

US Department of Defense. Anthropometry of US military personnel (Metric). Military Handbook, DOD-HDBK-743A. (1991).

US Department of the Air Force. C-130J Operations Configuration/Mission Planning. Washington, DC: USAF; AFI 11-2C-130J Volume 3, Addenda A. (2009).

US Department of the Air Force. Critical Care Air Transport Teams (CCATT). Washington, DC: USAF; AFTTP 3-42.51. (2015).

US Department of the Air Force. En Route Care and Aeromedical Evacuation Medical Operations. Washington, DC: USAF, AFI 48-301 Volume 1. (2017).

US Department of the Air Force Technical Order: TO 1C-130H-2-21JG-30-01.

Virtanen, P., Gommers, R., Oliphant, T. E., Haberland, M., Reddy, T., Cournapeau, D., ... & van der Walt, S. J. SciPy 1.0: Fundamental Algorithms for Scientific Computing in Python. Nature methods, 17(3), pp 261-272. (2020).

Walsh, M. M. Thermal Environment of Litter Positions and Human Responses Onboard Hercules C-130 Aircraft (No. AFIT-98-011). Air Force Institute of Technology Wright-Patterson, AFB United States. (1998).

Withers, M. R., & Christopher, G. W. Aeromedical evacuation of biological warfare casualties: a treatise on infectious diseases on aircraft. Military medicine, 165(suppl_3), pp 1-21. (2000).

Wood, W. Trouble Shooting Hercules Air Conditioning. Service News: Vol 16 no. 2, April-June, pp 3-12. (1989).

Yan, Y., Li, X., & Tu, J. Thermal Effect of Human Body on Cough Droplets Evaporation and Dispersion in an Enclosed Space. Building and Environment, 148, pp 96-106. (2019).

Appendix I Publication: A Review of CBRN topics related to military and civilian patient exposure and decontamination.

Page intentionally left blank.

DM

REVIEW ARTICLE

A review of CBRN topics related to military and civilian patient exposure and decontamination

Emily Titus, BS; George Lemmer, BS; Jeremy Slagley, PhD; Robert Eninger, PhD

Abstract

Chemical and biological (CB) warfare have long been practiced, and although these types of warfare are not acceptable in modern times, this does not prevent them from occurring. This makes it important for societies to be able to appropriately respond to these events, including the best way to decontaminate victims to keep them and emergency responders safe. Decontamination methods such as chemical, physical, wet, and dry methods are discussed, as well as their downsides. Secondary contamination, which played a significant role in the Tokyo sarin attacks, has long been noted by anecdotal evidence, although it has been little studied. Biological agents cause more problems after infection has taken place, and thus preventing the spread of infection is the largest concern. There are many differences between military and civilian populations, and the response to mass casualty attacks differs accordingly. There are several emerging technologies that can make this process easier on all parties, such as bioscavengers, antitoxins, and color changing bleach for visualization. A reliable way to quantify decontamination is also needed, which would allow for better care of victims both in normal hospital situations, as well as during aeromedical transport. In addition, several gaps were identified, such as the lack of scientific basis for 90 percent reduction during decontamination, a way to quantify decontamination, and the lack of studies on toxic industrial chemicals and secondary contamination.

The views expressed in this article are the work of the authors and do not necessarily reflect the official policy or position of the US Government, the US Department of Defense, or the US Air Force.

Key words: CBRN, decontamination, biological, chemical, decontaminants

Introduction

History of CBRN

Chemical and biological (CB) threats have been recorded throughout the history of warfare using a variety of agents and methods. This has included the use of venom on arrowheads or burning sulfur or mustard plants as irritants to slow the digging of siege tunnels.[1] A complete history of the use of CB agents and toxins is beyond the intent of the current work. Modern warfare draws battle lines under such agreements as the Geneva Convention and the Convention on the Prohibition of the Development, Production, Stockpiling, and Use of Chemical Weapons and on their Destruction administered by the Organisation for the Prohibition of Chemical Weapons to eliminate the use of chemical warfare agents (CWAs) on the battlefield and against dissident civilian populations. Under the convention, the use of toxic chemicals with the specific intent to harm or kill is prohibited, as well as the munitions that aid in delivery and dispersal of these chemicals.[2]

The Department of Defense (DOD) recognizes the threats posed by toxic industrial chemicals and materials (TICs/TIMs) in addition to threats posed by chemical, biological, radiological, and nuclear (CBRN) agents. AFTTP 3-2.55 lists the civilian references applicable to TIC/TIM response.[3] The DOD is focused on CWAs because they are intended to be highly lethal at very low concentrations, even immediately after exposure. Specially designed personal protective

DOI:10.5055/ajdm.2019.0324

equipment (PPE) such as Mission Oriented Protective Posture (MOPP) gear and specific Tactics, Techniques, and Procedures (TTPs) for delineating decontamination operations are the primary means of counter CBRN activities.

After a chemical or biological warfare attack, there is a need to decontaminate victims in order to reduce the negative physiological effects from prolonged exposure to these agents. This work reviewed literature on decontaminants and attempts to understand the current state of the science as well as gaps in the knowledge. The scholarly literature was searched from September 2018 to February 2019 for works relating to CB decontamination and relevant topics. In addition, some relevant military literature and TTPs were reviewed.

Decontamination

The current US doctrine on decontamination during mass casualty events is summarized in a 2013 report from Edgewood Chemical and Biological Center (ECBC).[4] This report suggests that moving victims from the "Hot Zone," followed by the immediate removal of clothing and flushing with water at 50-60 psi should remove 80-90 percent of contamination. This document is the basis for mass casualty response and describes in detail the requirements for zoning and decontamination. Mass decontamination processes require controlled access to and exit from the contamination source and should be oriented in ways that account for weather conditions. They also rely on a flow through line system to allow for mass washing of victims. Decontamination is clearly defined in this report as making any personnel, material, or area safe by neutralizing or removing CB agents or nuclear material. Quantification of contamination or decontamination is not covered by the document.

Broadly, decontamination is the removal or neutralization of hazardous agents on people, equipment, or surfaces.[5-11] Decontamination is important to protect both victims and first responders as well as future users of contaminated equipment.[5,12-21] Decontamination processes can be classified by whether they are chemical or physical or whether they are wet or dry.

Chemical decontamination uses a chemical agent which can degrade or neutralize the contaminant into a less toxic form. This can be done by hydrolysis (washing with water and soap), oxidation (oxidative chlorination is common), or by acid or base hydrolysis (although this can be very caustic to the skin, as is the case with sodium hydroxide or concentrated bleach).[6,9,22]

Physical decontamination is the physical removal of a contaminant from the skin by washing with water, mechanical brushing, or adsorption onto a decontaminant. It is very important for biological decontamination to prevent later infection.[11] One advantage of physical decontaminants is that the agent does not have to be known for physical decontamination to be effective.[22] However, there are disadvantages to both chemical and physical decontamination methods. Chemical methods can be slow as they rely on chemical reactions.[6,22] On the other hand, while physical methods are much quicker, they merely relocate the hazardous agent from the victim to the decontaminant. This creates a great deal of contaminated waste that must be managed appropriately.[7]

Decontamination methods may also be distinguished by whether they are a wet or dry method. Dry decontaminants are absorbent materials used to soak up contaminants, making them most useful for liquids, oils, fatty, or greasy contaminants.[5,19] Dry decontaminants can be commercial off-the-shelf (COTS) products such as Fuller's Earth or M291 resin, or they may be improvised decontaminants such as paper towels, cloths, baking powder, or talc.[19,22]

Wet decontamination consists of washing the affected area with plain or soapy water to remove the chemical agent. Showering is the most recommended decontamination method.[15,19,23-26] However, it should not be used for water reactive agents, or during cold weather to protect against hypothermia.[5,18,19,27]

There are several principles of conventional wisdom pertaining to decontamination. Disrobing is considered the first crucial step, followed by showering. Ventilation to promote off-gassing is also occasionally suggested, although not as widely as disrobing or showering. Finally, it is recommended to start decontamination as soon as possible after being exposed to a hazardous agent.

It is often stated that disrobing will remove between 70 and 90 percent of contamination.[5,18,21,23,28] This is widely accepted to be true and informs many official CBRN decontamination and response guidelines. However, during the course of this review, no definitive scientific basis was found.

Showering to remove contaminants is highly recommended during decontamination.[7,18,19,22,23,25] However, it has been shown that the efficacy of showering may depend on water pressure, temperature, flow rate, the use of detergents, and presence of clothing.[6,21-24,29] In addition, there is some evidence that showering may increase absorption due to the "wash-in" effect.[19,24,30,31] The "wash-in" effect is the enhancement of dermal penetration of a chemical due to washing, although it has not been well characterized. One review proposes that the effect may stem from degradation of the barrier qualities of the stratum corneum due to hydration, surfactants, acidic, or basic qualities of washing aids or liquid decontaminants, or friction from physical washing.[31] They also note that the majority of studies have been done in vitro, so the effect may be an artifact of the methodology.[31]

Ventilation of the body or clothing may be helpful if the exposure was to a gaseous agent, although few sources considered this.[25] In addition, if there were high levels of exposure with the potential for off-gassing, ventilation could be recommended to avoid trapping contaminants between clothes and creating continuing exposure. However, ventilation of areas is often recommended as a protective measure for both victims and first responders. Ventilating decontamination, triage, or care areas when chemically contaminated patients are involved is important in order to minimize risk of gas build-up and creating a secondary exposure source for parties in the area.[13,16,18-20] In addition, patients suspected to be exposed to highly infectious biowarfare agents (or those obviously showing symptoms) should be isolated from workers and other patients by having separate ventilation.[32]

Decontamination is recommended to start as soon as possible, although the importance of this timing has not been well characterized.[8,10,30,33] One research group demonstrates that starting decontamination sooner increases the decontamination efficiency by showing that the penetration rate of VX decreases more quickly the sooner decontamination is started.[8]

Decontamination method efficacy differs depending on contaminating agent, countermeasures employed, and duration of exposure before commencing decontamination procedures. Efficacy of decontamination of soman was studied comparing treatments with 0.5 percent bleach, 1 percent soapy water, Reactive Skin Decontamination Lotion (RSDL), and M291 skin decontamination kit (M291 SDK) on the skin of exposed guinea pigs. Each decontamination was performed 2 minutes following soman challenge and efficacy was measured by calculating a protection ratio (PR) from the adjusted LD_{50} after decontamination. RSDL, with a PR of 14, provided the best PR under the experimental design, however, subsequent delayed decontamination trials showed greatly reduced efficacy.[34] The other decontaminants tested showed significantly smaller protections factors with 1 percent soapy water having a PR of 2.18, 0.5 percent bleach having a PR of 2.63, and M291 SDK having a PR of 2.73.[34]

Discussion

Secondary contamination

Secondary contamination is the spread of contamination to people who were not present during the initial attack, such as emergency responders, by contact with victims who were.[5,12,16,24] This is often cited as a potential threat to first responders and emergency department healthcare workers due to contact or inhalation of vapors from contaminated patients. It is widely recognized as a risk from anecdotal evidence but has been little studied or quantified.

One study simulated decontamination of a patient and measured the breathing zone concentrations of vapor and particulate contaminants.[17] The authors simulated a "worst-case" scenario where decontamination was undertaken in a room with blocked ventilation. The clothing of a mannequin was saturated with an organic solvent or metal oxide particles and the air in the room was sampled, as well as the breathing zone of both physicians performing

the decontamination and that of the mannequin.[17] The physicians had breathing zone values which were about a third of the American Conference of Governmental Industrial Hygienists (ACGIH) short-term exposure limit (STEL) for the organic solvents and significantly less than the available Occupational Safety and Health Administration permissible exposure limits for the particulates.[17] Although the ACGIH STELs have been revised since the original study, the exposures would be below the 2018 STELs. However, when the researchers extrapolated to more hazardous chemicals, the predicted exposures were much higher than the relevant STELs.[17] In addition, the authors point out the uncertainty about the linearity of the relationship between relative evaporation rates and vapor pressure and recommend further testing be done on different chemicals to determine this.

A subsequent article cited this study and extrapolated the results to sarin. This extrapolation predicted a sarin concentration maximum of no more than 50 ppm.[16] The authors note that the saturation volumes used in the original study would likely be a significant overestimation of a true exposure during a mass casualty situation and thus this maximum concentration would likely not be reached.[16] However, according to the US Environmental Protection Agency's Acute Exposure Guideline Levels, the nondisabling 10-minute exposure to sarin should be less than 0.0012 ppm.[35] The authors also point out that if healthcare workers wear respirators with organic vapor cartridges, there should be little risk, based on the findings of an ECBC study which tested organic vapor cartridge respirators against sarin for up to 6 hours and exhibited no breakthrough of the cartridges.[36]

Another study was reviewed, in which the author exposed different types of clothing to a high concentration of methyl salicylate (MeS), a sulfur mustard simulant. The air near the clothing was periodically measured for MeS until the concentration was 0.[37] This author found that lightweight clothing, such as cotton t-shirts or jeans reached a zero concentration very quickly, with an average of 7 minutes, while down-filled outerwear took much longer, a mean of 42 minutes to reach 0.[37] Mass decontamination showers take significant amounts of time to set up, up to 30 minutes by some estimations.[15,27] From this, the author concluded that decontamination showers may be unnecessary for victims only exposed to vapor as all contamination likely would have dissipated before showers were set up.[37] However, decontamination showers are still recommended for patients exposed to liquid or solid contaminants. While decontamination may not be necessary for victims waiting outdoors, if patients enter enclosed spaces, such as an ambulance, within 35 minutes of exposure, there could be significant risk of vapor accumulation from clothing off-gassing, thus contaminating the space or emergency responders.[37] Due to unique chemical properties between even chemicals in the same family, there is a need for further studies examining the off-gas potential for different chemical agents, as well as for testing different clothing types.

Decontaminants

There are a variety of COTS decontaminants available. The two most widely used are RSDL and Fuller's Earth. In addition, some US Air Force instructions recommend the use of M291 skin decontamination kits. These decontaminants have mainly been tested against CWAs and may not have the same efficacy against TIC/TIMs or biological agents.

RSDL is a unique decontaminant because it utilizes both chemical and physical methods of decontamination. It contains a reactive oxime (diacetyl monoxime, DAM) along with the potassium salt of DAM which is used to neutralize chemical agents as well as polyethylene glycol monomethyl ether (mPEG) which is used to absorb them.[5,7,8,38] RSDL has a low water content, which may increase solubilization of lipophilic compounds such as the organophosphate (OP) VX.[7]

The shelf-life of a product is important to consider when it is purchased for emergency situations and may not be replenished frequently, as is the case with decontaminants. The shelf-life of RSDL was evaluated in a 2018 study.[38] Due to its use in military campaigns, RSDL may not always be stored under ideal conditions. To understand the shelf-life under nonideal conditions, they evaluated the stability and degradation

of DAM, as well as the formation of dimethylglyoxime (DMG), a degradation product of DAM. They stress-tested the product through short-term storage at very high temperatures in order to determine the kinetics. DAM degradation followed first-order kinetics, while DMG formation followed zero-order kinetics.[38] These constants were used to predict the shelf-life of stored military samples. These samples were taken from a military storage depot where the product was kept at 20°C, within the manufacturer's specifications, and from a training mission in Mali, where it was kept at ambient temperature.[38] The mean kinetic temperature during this training mission was 31°C, above the manufacturer's specifications.[38] The stress testing showed that even short-term periods of storage above the manufacturer's specifications can significantly degrade DAM, although the infrequent fluctuations in temperature above the manufacturer's specifications during the training mission did not significantly affect the active ingredient.[38] This study shows the importance of evaluating storage and mission conditions to understand the impact of temperature on decontaminants vital to personnel survival in emergency situations.

RSDL has been reported by the manufacturer to be effective against most CWAs and one biological warfare agent.[6] One lab group evaluated the decontamination efficacy of RSDL against neat VX, VX diluted in water to 20, 75, or 90 percent, and a hydrophilic organophosphorus compound.[7,8] In one study, they tested three formulations of RSDL: RSDL as a concentrated lotion, RSDL as a diluted lotion, or RSDL delivered by a sponge against neat VX or 20 percent VX.[7] Three other decontaminants (alldecontMED, Fuller's Earth, and PS104) were tested in addition to the different formulations of RSDL. These were tested for varying contact times, decontamination start times, and removal protocols. Overall, concentrated RSDL lotion was the most effective at reducing the penetration rate of VX into human skin. However, the concentrated and dilute RSDL lotions were left on the skin for 30 minutes, while the sponge was used to swab the skin for a 2-minute contact time, which could bias the results toward the lotion. A different study from the same group evaluated the decontamination efficiency of concentrated RSDL lotion against neat or dilute VX or triethyl phosphonoacetate (TEPA).[8] TEPA is a hydrophilic organophosphorus compound, while VX is a lipophilic compound.[8] RSDL significantly reduced the penetration of VX while there was not a significant decrease for TEPA. This signals that solubility in RSDL may increase the efficacy of decontamination for lipophilic compounds.[8]

Another common decontaminant is Fuller's Earth. Unlike RSDL, Fuller's Earth is purely a physical decontaminant. It is also considered a dry decontaminant as it is a highly absorbent, nonplastic type of clay which contains aluminum-magnesium silicate and can easily adsorb fats, greases, and oils but has no degradation properties.[5-7] A downside of this decontaminant is that prolonged contact may cause skin irritation and inhalation is a potential hazard.[6]

One study compared the efficacy of Fuller's Earth to hemostatic (clotting) agents on damaged and undamaged skin.[39] This study evaluated Fuller's Earth, QuikClot Advanced Clotting Sponge Plus, ProQR, and WoundStat against the CWAs VX, HD, and GD.[39] The authors found that both Fuller's Earth and WoundStat reduced penetration significantly and at similar rates.[39] One limitation of this study, however, was that total recovery of the dose of chemical agent was low, less than 40 percent.[39] In addition, the study used porcine skin rather than human, so the results must be extrapolated which introduces error. Finally, the amount of chemical agent present in various fractions was measured by analyzing radioactivity by Liquid Scintillation Counting which cannot distinguish between the original CWA and metabolites. However, this would assume a worst-case scenario so it should not be considered a significant shortfall.

In a previously discussed study, Fuller's Earth was compared to RSDL, PS104, and alldecontMED for reduction of penetration efficiency against VX.[7] In this study, decontamination was started either 5 or 30 minutes after exposure to the agent and Fuller's Earth was left on the exposure site for 30 minutes.[7] In this scenario, Fuller's Earth was least effective at reducing the penetration of VX when applied 5 minutes after exposure, but was the most effective product tested when applied 30 minutes after VX exposure.[7]

A study evaluated two COTS decontaminants (Fuller's Earth and Fast-Act) along with three novel polymers (itaconic acid, *N,N*-methylenebisacrylamide, and 2-trifluoromethylacrylic acid) for decontamination efficiency against sulfur mustard, soman, or VX.[9] The decontaminants were all applied 5 minutes after exposure to the CWA and left on for 24 hours while penetration rate was measured. The authors found that Fuller's Earth, itaconic acid, and 2-trifluoromethylacrylic acid all significantly reduced the total penetration of all three CWAs tested.[9] One limitation of the study is that the amount of sulfur mustard recovered was very low, around 2 percent, while around 70 percent of VX was recovered.[9] This could limit the significance of the conclusions drawn for sulfur mustard.

Recently, it has been recognized that the scalp could provide a significant exposure pathway for CWAs. In addition, contaminants could be trapped in the hair, prolonging exposure to the agent or creating a reservoir for secondary contamination. One study exposed locks of hair to one of two sulfur mustard simulants, MeS or 2-chloroethyl ethyl sulfide (CEES).[26] The hair was exposed to the vapor for 2 hours, then Fuller's Earth or RSDL was used to decontaminate the hair prior to washing with soap and water. This study revealed that using a decontaminant resulted in significantly less MeS or CEES remaining in the hair compared to just soap and water.[26] However, there was still a significant mass of both CEES and MeS present after decontamination, showering, and drying, which could lead to secondary exposure by off-gassing. Overall, decontamination efficiency was higher for CEES than MeS.[26] This is promising because although MeS is a favored sulfur mustard simulant, the physical structure of CEES is much closer to that of sulfur mustard, differing only by the presence of one chlorine atom.[26] One limitation of this study was that the decontaminants were applied and then removed without mechanical washing. This was important to the authors to reduce tester variability, although this variability would be present in real-world scenarios so it should be incorporated into testing.

A second study aimed to understand the permeability of human scalp skin to VX compared to human abdominal skin and porcine ear and scalp skin. The scalp is likely to be more exposed than other parts of the body, and may be easier to penetrate due to the number of hair follicles which can aid chemical penetration of the stratum corneum, as well as act as reservoirs.[40] This study showed that porcine ear skin could be used as a model for human scalp permeability studies due to the statistically similar penetration rates of VX, the similar stratum corneum thickness, and the similar follicle diameter.[40] The follicle density was higher in the human scalp than porcine ear, but the reservoir capacity was similar, indicating that the number of follicles is less important than the diameter.[40] This was also shown to be true for penetration ability. The authors noted that many studies ignore hair follicles due to the assumption that the number of follicles is negligible compared to the skin surface area, however, in the case of the scalp and face, this is false.[40] This is important because the head and face are often left uncovered in most populations.

Selected case studies

Japan, Sarin. In 1994 and 1995, separate CWA attacks occurred on civilian populations using sarin gas. The 1994 incident took place in Matsumoto, Japan, dispersing an impure form of sarin from a truck, which affected approximately 600 people, seven of whom died and 58 of whom were admitted to the hospital.[41] The 1995 incident, in which sarin gas was released on the Tokyo subway, resulted in 12 deaths and around 5,500 people exposed. During this incident, it is estimated that roughly 20 percent of emergency department workers and 10 percent of emergency first responders suffered symptoms resulting from secondary exposure.[41] Eight of 53 personnel deemed rescuers, along with one doctor, reported mild symptoms resulting from patient interaction. After exposure, it was determined that 124 patients had miosis that adversely affected vision with some cases lasting 30 days post exposure.[42]

The sarin gas attacks in Tokyo in 1995 resulted in significant civilian and healthcare worker casualties.[16] The majority of patients who entered emergency departments in the aftermath of the attacks had self-presented, meaning that they had no decontamination

prior to care at the hospital.[16] In addition, healthcare workers who treated these patients did so in poorly ventilated rooms without wearing any respiratory protective equipment.[16] This resulted in ~20 percent of healthcare workers (over 100 workers) who treated patients after this attack becoming contaminated and showing symptoms of sarin exposure.[16,37]

Gulf War, Sarin. The DOD reported exposure of service members to sarin and cyclosarin during the 1991 Gulf War during munitions dump detonation at Khamisiyah, Iraq. Reported exposures were modeled with high dose ranging from 0.072 to 0.144 mg min/m^3 to no exposure depending on the proximity of the unit during the depot destruction. Neurobehavioral evaluation was performed on soldiers with known exposures prior to public acknowledgement of the event for comparison with follow up testing to evaluate long-term effects of exposure to survivable doses of sarin and cyclosarin.[43] The results indicate reduced visuospatial and manual dexterity in a dose dependent manner but lack pre-deployment baseline evaluations. This case study indicated the importance of thorough medical screening prior to deployment of US forces due to unforeseen exposures that could be encountered in future theatres of operation.

Biologicals

Responding to biological warfare agents often focuses on treating clinical symptoms to prevent the spread of infection, rather than on decontamination.[5] In addition, decontamination after a biological attack is not as time critical because most biological agents are not able to penetrate the skin the way chemical agents can.[22,28] Thus, recommendations for biological attacks are to wash the hands with soap and water or a 0.5 percent hypochlorite solution to remove microorganisms and prevent the risk of ingestion or inhalation later.[22] While outside the scope of this article, it is worth noting that although there is little literature on how to decontaminate a patient after a biological attack, there is a wealth of information within the medical community on how to decontaminate surfaces and materials after highly infectious patients have used them.

Patients who have been infected with biological warfare agents should be handled similarly to treatment of highly infectious patients (such as severe acute respiratory syndrome or Ebolavirus). Depending on treatment availability and patient condition, highly infectious patients may need to be transported between medical facilities. This is called medical evacuation if patients are transported by ground vehicle or aeromedical evacuation (AE) if they are transported by aircraft.[44] The US Air Force routinely flies AE missions. Critical Care Air Transport Teams (CCATT), which include critical care nurses, physicians, and respiratory therapists, accompany patients to provide medical care.[45] These healthcare providers receive special training to understand the physiological stresses imparted by air transport.[45]

During flight, highly infectious patients should be isolated to prevent the spread of disease to the CCATT team, the aircrew, or any other patients.[44,46] Care members or patients may also need to wear appropriate PPE such as air purifying respirators to protect themselves and those around them.[32,44]

Civilian versus military populations

Several factors separate military from civilian populations. The scale of an attack, the amount of training, the location of equipment used for decontamination, and the make-up of the populations are all different. Military personnel undergo training for emergency situations such as CBRN attacks and decontamination, whereas this is not present in the general population.[14,28]

There are many considerations when preparing for mass casualty or mass decontamination events. Due to the nature of military operations, they must be prepared for events both in the field as well as at home bases. The home base preparations are similar to those made by civilian hospitals. Fixed decontamination facilities located at hospitals should be located near, but not within the emergency department in order to allow contaminated patients to pass through the decontamination facility prior to entering the emergency department.[15] These facilities should have exterior ventilation in order to prevent build-up of hazardous gases and vapors and subsequent secondary contamination from these vapors.[15,18]

Mobile decontamination shelters should be stored where they are easily accessible during an emergency situation.[15] Other considerations for mobile shelters include clean water sources and hook-ups, capture and storage of contaminated water, water heaters, and light sources both inside and outside the shelters.[15,18,19] In addition, personnel are needed to set up and man these mobile decontamination systems.[15]

Another difference between civilian and military groups responding to a CBRN situation is the culture and chain of command present within military units.[14] Discipline is a key facet of the military culture and it is expected that military members comply with decontamination procedures. On the other hand, civilian populations lack the command and control possessed by military organizations, thus making them less likely to comply with procedures, particularly if they are contrary to cultural norms. Public compliance with instructions during a mass decontamination situation depends on the perception of risk and amount of trust in the authorities who are asking for their cooperation.[47] Of particular concern is the issue of privacy. Doffing clothing is generally the first step in an effective decontamination response. However, this creates privacy concerns in the general population. If this issue is not adequately addressed, public compliance during a situation will be reluctant at best.[14,15,19]

The military population is much more homogenous than the general public. Civilian populations include children, the elderly, and people with illnesses and physical or mental disabilities, while the military excludes these more vulnerable groups.[14] This heterogeneity of civilian populations can also impede compliance to decontamination procedures. If young, elderly, disabled, or people who do not speak the language well are affected by a CBRN attack, they may need help to respond to decontamination instructions properly.[14,19]

Military decontamination standard operating procedures include protective outer garment decontamination as specified by AFTTP 3-2.60 and the detailed specification stated in MIL-DTL-32102, that delineates all specification and construction standards required for MOPP gear.[48,49] The most notable specifications are the duration of impermeability, 45 days of wear during a liquid challenge to HD, GD, and VX and the dispersal concentration of 10 g/m^2. The garment must also be able to withstand six launderings after exposure to a variety of contaminants found in an operational environment.

Selected emergent technologies

Bioscavengers. Bioscavengers are enzymes which prevent OP chemicals from disrupting natural cholinesterase activity leading to the accumulation of neurotransmitters which cause cholinergic crisis and, if severe enough, death. Bioscavengers are characterized as stoichiometric, pseudocatalytic, or catalytic depending on their quantity or enzymatic activity to prevent systemic nerve agent poisoning.[50] Stoichiometric bioscavengers can be artificially produced or isolated from organisms, such as butyrylcholinesterase which is collected from plasma fractionation and harvested for prophylactic treatments. Stoichiometric bioscavengers react irreversibly with OPs and are inhibited in the process of phosphorylation of OPs. Pseudocatalytic bioscavengers are oxime reactivated stoichiometric bioscavengers that are regenerated to cycle through the process of OP bonding and degradation. Catalytic bioscavengers function to break down OPs without a separate reactivation enzyme.[51]

Ricin antitoxin. Ricin toxin has long been a concern due to its relative ease to acquire and high toxicity. Antitoxin has been derived from equine serum inoculated with monomerized toxin that elicits greater antibody production with less toxicity. The antitoxin was able to afford a greater than 60 percent survival rate in mice from a challenge to lethal dose of ricin toxin when administered 24 hours post challenge and 35 percent survival rate when administered 48 hours post challenge.[52] Previous antitoxin derived from rabbits had shown a survival rate of 34 percent at 24 hours with greater cytokine levels in bronchoalveolar lavage fluid.[53]

Nanotube-lined PPE. Research has shown that single-wall carbon nanotubes with an embedded

catalytic copper functional group can breakdown OP simulants as proof-of-concept that future PPE could self-decontaminate. Structurally and chemically active nanomaterials expressed kinetic activity that was evidence of breakdown of the CWA simulant 4-nitrophenol phosphate sodium in water. Spectral absorbance was used to measure *p*-nitrophenol, the hydrolyzed product of 4-nitrophenol phosphate sodium, and the material continued to be kinetically active following 18 days of continuous exposure to CWA simulants.[54]

Nanomaterial Decon Wipes. A multipurpose dry decontamination wipe has been proposed and tested against various CB agents using a multilayer design incorporating zinc ($ZnTiO_3$) and silver ($AgNO_3$) nanoparticles and a layer of activated carbon. The wipe was tested against diethyl chlorophosphate (DCP) and CEES to decontaminate rats and separately to test inhibition of *E. coli* and *S. aureus* bacteria and Penicillium species with reported greater than 95 percent efficacy. Dermal exposures to DCP and CEES were evaluated using Ache inhibition assay (90 percent less inhibition than exposed group), and histopathological examination, respectively.[55]

Mid wave infrared detection of chemical agents. Demonstrating instrument parameters regarding field of view, detection threshold, and data processing are critical to future development of instruments that can meet the requirements for low limit, highly accurate agent identification in a field setting. Mid wave infrared (IR) laser sources target the 2.5-3.7 µm range, which covers the absorption bands of oxygen-hydrogen and carbon-hydrogen bonds. These can be used to identify CWAs or other chemical. A device using active hyperspectral mid wave IR in combination with an intra-cavity optical parametric oscillator IR laser source was used to cover the 2.5-3.7 µm range in 10-nm steps. Benchmark tests and calibration of M Squared Lasers Ltd Negative Contract Imager consisted of three modules: laser source, scanner/detector, and electronics. The laser source is a Q-switched laser with repetition rate of 150 kHz and nominal power output of 90 mW. The system weighed 15 kg and was battery operated. After determining reference spectra for CWA simulants, the system was used to identify VX and O-Mustard on various substrates in varying volumes. The limit of detection for VX on metal and glass was 1008 and 962 mg/m^2 for O-Mustard on sand.[56]

Color change bleach. Highlight® is a chemical additive to chlorine disinfecting solutions that imparts color which fades to transparent. The proprietary formula is designed to retain its color for desired dwell time based on the concentration of the solution. Recently, funding from a USAID grant allowed the use in Guinea in response to the Ebola outbreak of 2014-2015 to examine healthcare workers adherence to decontamination during PPE doff procedures.

Pickering emulsions. Pickering emulsions are emulsions stabilized by solid particles rather than the usual method of stabilization by surfactants.[10] Solid particles adsorb to the surface of oil particles to stabilize the oil-water interface. This may decrease the risk of the wash-in effect by not having a surfactant present. In addition, they may have increased sorbency due to having both an oil and water phase for adsorption of both hydrophilic and lipophilic compounds.[10] One research group dispersed silica and Fuller's Earth into water, then used those particles to stabilize an oil-in-water emulsion which was used to decontaminate VX.[10] Fuller's Earth in Pickering emulsion was the most effective, as the larger oil droplets were able to disperse more VX.[10] However, silica dispersed in water, as well as in the Pickering emulsion were both highly effective. The authors believed this was due to the pH of the solution being acidic, thus allowing VX to be in a majority positively charged state. In addition, silica can form both acidic and basic polar interactions.[10]

Further discussion

There is no standard methodology for testing so it may be difficult to determine the best decontaminant in scholarly literature. The ECBC published the 2007 Source Document to implement improved and rigorous test methodology in order to standardize DOD evaluation efforts.

It is difficult to draw conclusions from the numerous papers which have studied the efficacy of various commercial decontaminants. There is no standard methodology between research groups for the different factors which may affect decontamination efficacy, such as the time when decontamination starts after exposure, the contact time for decontaminants, or the amount of decontaminant applied. Some decontaminants, like RSDL, work best when applied within seconds or minutes after exposure, while others, like Fuller's Earth may have a higher efficacy when applied longer after exposure. Many studies also use a much longer contact time for decontamination than would be likely in a real-world scenario. In an emergency situation, it is likely that decontaminants would only be allowed to work on the skin for a few minutes, while many studies leave the decontaminant on the skin for hours. These differences between the chaos of a real-world situation and the studies conducted make it difficult to determine which decontaminant may be the best.

In addition, there is no standard for quantification of decontamination. In most studies, high pressure liquid chromatography, gas chromatography (with mass spectrometry or flame ionization detector) or liquid scintillation counting are used to analyze the amount of chemical remaining after decontamination, however, these methods are not practical for field use. There is a need for a reliable and precise way to measure whether decontamination of personnel or equipment in the field has been done to a protective extent. Laser or IR detectors may be useful field tools if they can be developed to meet the required limits of detection.

Another limitation of the many studies that have been conducted is that they have focused on CWAs or similar compounds, such as OP pesticides or chemical agent simulants. With the exception of pesticides, these agents are banned from use or manufacture except by specially authorized groups. This makes them unlikely, though not impossible, to be used as a weapon. However, there are numerous industrially produced chemicals which may pose a significant hazard to civilian or military populations. Called toxic industrial chemicals (or materials, TIC or TIM), these chemicals may be more easily weaponized. A chemical can be classified as a TIC if it has a lethal concentration in air to 50 percent of the test population multiplied by exposure time (LCt_{50}) of less than 10^5 mg min/m^3 or is produced in quantities greater than 30 tons/year in a single facility.[6] These chemicals are recognized by OSHA and other regulatory agencies to pose a significant threat to public welfare if they are released, yet they have not been well studied for their response to standard decontamination procedures.

Use of CB warfare agents is a low incidence-high consequence event for military operations or against a civilian population that can have long-term implications for those affected. The abundance of emergency management and military-specific operation manuals highlights the seriousness of such an event occurring. The differences between military and civilian responses to mass casualty CB events have been discussed. It is logical that a military population would be more capable to respond to such an event. However, although military units must undergo training, the quality of the training may affect the response to an event. Military TTPs are written assuming that the people performing them are complying perfectly in order to reduce the risk for all affected personnel. However, human nature makes it likely that not all people in the decontamination line are perfectly effective at decontaminating themselves and others. It is easy to imagine that in the panic created by a situation that spots would be missed, leading to imperfect decontamination and the potential for secondary contamination of unaffected spaces or personnel. This makes human behavior an important element to plan for during emergency situations.

The use of protection factors when measuring decontamination efficacy indicates that the current state of defining "decontamination" is directly related to surviving the incident. Future technology in the form of universal detectors with the ability to accurately identify and quantify extremely low concentrations at a distance should be the focus to change the current state of decontamination as a survived exposure event. The DOD maintains several technology surveys of COTS detectors for CBRN and rates them based on manufacturer specifications to determine their suitability for diagnostics and use in a field environment.

The 2017 survey, which covered the period between January and March 2014, had 138 biological, 72 chemical, 49 radiological, and 44 combinational detectors and 12 that claimed to detect biological, chemical, and radiological agents, though failed to rate any single detector as top tier across all the categories covered in the survey. Because there is no single detector that can successfully detect all CBRN agents, the DOD must maintain multiple devices and the technical documentation to field an array of technology and research and development goals.

The DOD maintains a huge repository of information on all CBRN topics from open source to classified information. With this information being compartmentalized within the DOD, it does not always flow freely into the academic realm which creates an information gap of peer reviewed literature open to the public. The ability to methodically and reproducibly quantify decontamination is critical to scientific research of the subject matter. The quantification of decontamination needs to be standardized across methods and materials. The Defense Technical Information Center query for "decontamination" resulted in 58,079 entries and the earliest document from 1965, all results were from unclassified sources. The same search terms in EBSCO Academic Search Complete returned 10,535 from 1943 to present; while ScienceDirect had 52,328 articles returned.

While AEs are generally used to transport patients who have been stabilized, it is possible that patients may need to be transported soon after having been injured. If the injury occurred from a CBRN mass casualty attack, this could cause a significant problem for the aircrews. Although the assumption is that a patient will have been decontaminated prior to air evacuation, there is no way to quantify whether or how well decontamination has been done. If air crews assume that a patient is perfectly clean (as far as chemical contamination goes), they may not properly protect themselves from potential hazards. Off-gassing has been identified as a potential source of secondary contamination which is a risk for medical professionals. However, there has been little work done on whether a patient who has been decontaminated can still present an off-gas hazard. In addition, if decontamination is not done soon after an exposure, the chemical agent may have already entered the skin, which acts as a dermal reservoir. No evidence has been found for effects of changing altitude and pressure on this dermal reservoir which could significantly impact flight crews.

Secondary contamination of healthcare workers from care of chemically contaminated patients has been well documented but little studied. This could be an inhalational hazard in the form of trapped gas or vapor from patients clothing or hair, as well as a dermal hazard from liquid soaked clothing. Future research should further characterize this exposure and focus on understanding the risks to healthcare providers and how to mitigate this risk.

Another gap identified during this literature review was the assumption that decontamination always results in a 90 percent reduction in contamination level. Disrobing prior to decontamination is deemed important because of the fact it is assumed to remove roughly 90 percent of the contamination. It was also assumed that moving through a mass decontamination shower would result in a 90 percent reduction in contamination levels. This 90 percent rule is the basis for most military and civilian disaster response protocols, yet there seems to be little evidence to back it.

Conclusion

Although CB warfare has been practiced for centuries, the risk of these types of terrorist attacks is increasing. This makes it extremely important to understand the implications of these types of attacks, as well as the proper decontamination response procedures. Response to a mass casualty attack will depend on what type of agent is used and what decontamination procedures are available. It will also depend on the population which has been targeted, with significant differences between the responses for military and civilian populations. Several gaps were identified during the course of this review, such as the assumption of 90 percent decontamination, an adequate way to quickly quantify decontamination, and the need for further study on different toxic industrial chemicals, as well as secondary contamination risks.

Funding: *The authors declare no conflict of interest. This study was funded by a grant from the US Air Force School of Aerospace Medicine, # 2018-178R.*

Emily Titus, BS, Graduate Student Researcher, Department of Systems Engineering and Management, Air Force Institute of Technology, Wright-Patterson AFB, Ohio.

George Lemmer, BS, Graduate Student Researcher, Department of Systems Engineering and Management, Air Force Institute of Technology, Wright-Patterson AFB, Ohio.

Jeremy Slagley, PhD, Assistant Professor, Department of Systems Engineering and Management, Air Force Institute of Technology, Wright-Patterson AFB, Ohio.

Robert Eninger, PhD, Colonel, Assistant Professor, Department of Systems Engineering and Management, Air Force Institute of Technology, Wright-Patterson AFB, Ohio.

References

1. Salem H, Ternay Jr AL, Smart JK: Brief history and use of chemical warfare agents in warfare and terrorism. In Romano JAJ, Lukey BJ, Salem H (eds.): *Chemical Warfare Agents: Chemistry, Pharmacology, Toxicology, and Therapeutics*. 2nd ed. Boca Raton, FL: Taylor & Francis Group, 2013: 1-20.
2. OPCW: Convention on the prohibition of the development, production, stockpiling and use of chemical weapons and on their destruction. *Organisation for the Prohibition of Chemical Weapons*. The Hague, The Netherlands: Technical Secretariat of the Organisation for the Prohibition of Chemical Weapons, 2005: 1-181. Available at *https://www.opcw.org/sites/default/files/documents/CWC/CWC_en.pdf*. Accessed May 22, 2019.
3. US Department of Air Force: *Potential Military Chemical/Biological Agents and Compounds*. AFTTP(I) 3-2.55. Washington, DC: US Department of Air Force, 2005: V1-V6. Available at *https://fas.org/irp/doddir/army/fm3-11-9.pdf*. Accessed May 22, 2019.
4. Lake W, Divarco S, Schulze P, et al.: *Updated Guidelines for Mass Casualty Decontamination During a HAZMAT/Weapon of Mass Destruction Incident, Volumes I and II*. ECBC-SP-036. Aberdeen Proving Ground, MD: Edgewood Chemical Biological Center, 2013: 1-302.
5. Koenig KL, Boatright CJ, Hancock JA, et al.: Health care facility-based decontamination of victims exposed to chemical, biological, and radiological materials. *Am J Emerg Med*. 2008; 26(1): 71-80. doi:10.1016/j.ajem.2007.07.004.
6. Fatah AA, Arcilesi RD, Judd AK, et al.: *Guide for the Selection of Chemical, Biological, Radiological, and Nuclear Decontamination Equipment for Emergency First Responders*. Washington, DC: US Department of Homeland Security, 2007. Available at *https://ws680.nist.gov/publication/get_pdf.cfm?pub_id=911304*. Accessed October 28, 2018.
7. Thors L, Koch M, Wigenstam E, et al.: Comparison of skin decontamination efficacy of commercial decontamination products following exposure to VX on human skin. *Chem Biol Interact*. 2017; 273: 82-89. doi:10.1016/j.cbi.2017.06.002.
8. Thors L, Lindberg S, Johansson S, et al.: RSDL decontamination of human skin contaminated with the nerve agent VX. *Toxicol Lett*. 2017; 269: 47-54. doi:10.1016/j.toxlet.2017.02.001.
9. Matar H, Price SC, Chilcott RP: Further studies of the efficacy of military, commercial and novel skin decontaminants against the chemical warfare agents sulphur Mustard, Soman and VX. *Toxicol In Vitro*. 2019; 54: 263-268. doi:10.1016/j.tiv.2018.10.008.
10. Salerno A, Bolzinger M-A, Rolland P, et al.: Pickering emulsions for skin decontamination. *Toxicol In Vitro*. 2016; 34: 45-54. doi:10.1016/j.tiv.2016.03.005.
11. Solon JG, Killeen S: Decontamination and sterilization. *Surgery*. 2015; 33(11): 572-578. doi:10.1016/J.MPSUR.2015.08.006.
12. McGlone MM, Teece SC: Management of the poisoned patient. *Anaesth Intensive Care Med*. 2016; 17(10): 506-509. doi:10.1016/j.mpaic.2016.07.004.
13. D'Amelio E, Gentile B, Lista F, et al.: Historical evolution of human anthrax from occupational disease to potentially global threat as bioweapon. *Environ Int*. 2015; 85: 133-146. doi:10.1016/j.envint.2015.09.009.
14. Currie J, Heslop DJ: Operational systems evaluation of a large scale multi-agency decontamination exercise. *Int J Disaster Risk Reduct*. 2018; 31: 1054-1061. doi:10.1016/j.ijdrr.2018.03.027.
15. Hudson TL, Reilly K, Dulaigh J: Considerations for chemical decontamination shelters. *Disaster Manag Response*. 2003; 1(4): 110-113. doi:10.1016/j.dmr.2003.10.001.
16. Hick JL, Hanfling D, Burstein JL, et al.: Protective equipment for health care facility decontamination personnel: Regulations, risks, and recommendations. *Ann Emerg Med*. 2003; 42(3): 370-380. doi:10.1067/mem.2003.305.
17. Schultz M, Cisek J, Wabeke R: Simulated exposure of hospital emergency personnel to solvent vapors and respirable dust during decontamination of chemically exposed patients. *Ann Emerg Med*. 1995; 26(3): 324-329. doi:10.1016/S0196-0644(95)70081-1.
18. Cox RD: Decontamination and management of hazardous materials exposure victims in the emergency department. *Ann Emerg Med*. 1994; 23(4): 761-770. doi:10.1016/S0196-0644(94)70312-4.
19. Chilcott RP, Amlôt R: *Primary Response Incident Scene Management (PRISM) Guidance for Chemical Incidents, Volume 1: Strategic Guidance for Mass Casualty Disrobe and Decontamination*. Washington, DC: US Department of Health and Human Services, 2015. Available at *https://www.hsdl.org/?view&did=792704*. Accessed May 23, 2019.
20. Horton DK, Berkowitz Z, Kaye WE: Secondary contamination of ED personnel from hazardous materials events, 1995-2001. *Am J Emerg Med*. 2003; 21(3): 199-204. doi:10.1016/S0735-6757(02)42245-0.
21. Wolbarst AB, Wiley AL, Nemhauser JB, et al.: Medical response to a major radiologic emergency: A primer for medical and public health practitioners. *Radiology*. 2010; 254(3): 660-677. doi:10.1148/radiol.09090330/-/DC1.
22. Hurst CG: Decontamination. In Sidell FR, Takafuji ET, Franz DR (eds.): *Medical Aspects of Chemical and Biological Warfare*. Washington, DC: Office of The Surgeon General at TMM Publications, 1997: 351-359. doi:10.1016/B978-0-08-044529-8.50018-5.
23. Matar H, Larner J, Kansagra S, et al.: Design and characterisation of a novel in vitro skin diffusion cell system for assessing mass casualty decontamination systems. *Toxicol In Vitro*. 2014; 28(4): 492-501. doi:10.1016/j.tiv.2014.01.001.
24. Caneva DC, Kirk MA, Delaney JB: General approach to chemical attack. In Ciottone GR, Biddinger PD, Darling RG, et al. (eds.): *Ciottone's Disaster Medicine*. 2nd ed. Philadelphia, PA: Elsevier, 2016: 471-479. doi:10.1016/B978-0-323-28665-7.00078-9.
25. Gaskin S, Pisaniello D, Edwards JW, et al.: Chlorine and hydrogen cyanide gas interactions with human skin: In vitro studies to inform skin permeation and decontamination in HAZMAT incidents. *J Hazard Mater*. 2013; 262: 759-765. doi:10.1016/j.jhazmat.2013.09.040.
26. Spiandore M, Piram A, Lacoste A, et al.: Efficacy of scalp hair decontamination following exposure to vapours of sulphur mustard simulants 2-chloroethyl ethyl sulphide and methyl salicylate. *Chem Biol Interact*. 2017; 267: 74-79. doi:10.1016/j.cbi.2016.07.018.

27. Okumura T, Seto Y, Fuse A: Countermeasures against chemical terrorism in Japan. *Forensic Sci Int*. 2013; 227(1-3): 2-6. doi:10.1016/j.forsciint.2012.11.008.
28. Chilcott RP: Managing mass casualties and decontamination. *Environ Int*. 2014; 72: 37-45. doi:10.1016/j.envint.2014.02.006.
29. Farra S, Smith S, French D, et al.: Development of an assessment instrument to evaluate performance of the skill of decontamination. *Nurse Educ Today*. 2015; 35: 1016-1022. doi:10.1016/j.nedt.2015.04.010.
30. Loke WK, U SH, Lau SK, et al.: Wet decontamination-induced stratum corneum hydration—Effects on the skin barrier function to diethylmalonate. *J Appl Toxicol*. 1999; 19(4): 285-290. doi:10.1002/(SICI)1099-1263(199907/08)19:4<285::AID-JAT580>3.0.CO;2-X.
31. Moody RP, Maibach HI: Skin decontamination: Importance of the wash-in effect. *Food Chem Toxicol*. 2006; 44: 1783-1788. doi:10.1016/j.fct.2006.05.020.
32. Vinson E: Managing bioterrorism mass casualties in an emergency department: Lessons learned from a rural community hospital disaster drill. *Disaster Manag Response*. 2007; 5(1): 18-21. doi:10.1016/j.dmr.2006.11.003.
33. Mikler J, Tenn C, Worek F, et al.: Immobilization of Russian VX skin depots by localized cooling: Implications for decontamination and medical countermeasures. *Toxicol Lett*. 2011; 206: 47-53. doi:10.1016/j.toxlet.2011.05.1047.
34. Braue EHJ, Smith KH, Doxzon BF, et al.: Efficacy studies of reactive skin decontamination lotion, M291 skin decontamination kit, 0.5% bleach, 1% soapy water, and skin exposure reduction paste against chemical warfare agents, Part 2: Guinea pigs challenged with soman. *Cutan Ocul Toxicol*. 2010; 30(1): 29-37. doi:10.3109/15569527.2010.515281.
35. National Research Council: *Acute Exposure Guideline Levels for Selected Airborne Chemicals: Volume 3*. Washington, DC: The National Academies Press, 2003. Available at *https://doi.org/10.17226/10672*. Accessed June 7, 2019.
36. Campbell LE, Lins RR, Pappas AG: *Domestic Preparedness: Sarin Vapor Challenge and Corn Oil Protection Factor (PF) Testing of 3M BE10 Powered Air Purifying Respirator (PAPR) with AP3 Cartridge*. Aberdeen Proving Groung, MD: Soldier and Biological Chemical Command, 2001.
37. Feldman RJ: Chemical agent simulant release from clothing following vapor exposure. *Acad Emerg Med*. 2010; 17(2): 221-224. doi:10.1111/j.1553-2712.2009.00650.x.
38. Bogan R, Maas HJ, Zimmermann T: Chemical stability of reactive skin decontamination lotion (RSDL®). *Toxicol Lett*. 2018; 293: 264-268. doi:10.1016/j.toxlet.2017.09.016.
39. Lydon HL, Hall CA, Dalton CH, et al.: Development of haemostatic decontaminants for treatment of wounds contaminated with chemical warfare agents. 3: Evaluation of in vitro topical decontamination efficacy using damaged skin. *J Appl Toxicol*. 2017; 37(8): 976-984. doi:10.1002/jat.3446.
40. Rolland P, Bolzinger M-A, Cruz C, et al.: Human scalp permeability to the chemical warfare agent VX. *Toxicol In Vitro*. 2011; 25: 1974-1980. doi:10.1016/j.tiv.2011.06.021.
41. Tokuda Y, Kikuchi M, Takahashi O, et al.: Prehospital management of sarin nerve gas terrorism in urban settings: 10 years of progress after the Tokyo subway sarin attack. *Resuscitation*. 2006; 68: 193-202. doi:10.1016/j.resuscitation.2005.05.023.
42. Morita H, Yanagisawa N, Nakajima T, et al.: Sarin poisoning in Matsumoto, Japan. *Lancet*. 1995; 346: 290-293. doi:10.1016/S0140-6736(95)92170-2.
43. Proctor SP, Heaton KJ, Heeren T, et al.: Effects of sarin and cyclosarin exposure during the 1991 Gulf War on neurobehavioral functioning in US army veterans. *Neurotoxicology*. 2006; 27(6): 931-939. doi:10.1016/j.neuro.2006.08.001.
44. Schilling S, Follin P, Jarhall B, et al.: European concepts for the domestic transport of highly infectious patients. *Clin Microbiol Infect*. 2009; 15(8): 727-733. doi:10.1111/j.1469-0691.2009.02871.x.
45. Mason PE, Eadie JS, Holder AD: Prospective observational study of United States (US) Air Force Critical Care Air Transport Team Operations in Iraq. *J Emerg Med*. 2011; 41(1): 8-13. doi:10.1016/j.jemermed.2008.06.032.
46. US Department of Air Force: *En Route Care and Aeromedical Evacuation Medical Operations*. AFI 48-307. Vol. 1. Washington, DC: US Department of Air Force, 2017: 1-250. Available at *https://static.e-publishing.af.mil/production/1/af_sg/publication/afi48-307v1/afi48-307v1.pdf*. Accessed May 22, 2019.
47. Krieger K, Amlôt R, Rogers MB: Understanding public responses to chemical, biological, radiological and nuclear incidents—Driving factors, emerging themes and research gaps. *Environ Int*. 2014; 72: 66-74. doi:10.1016/j.envint.2014.04.017.
48. US Department of Defense: *Detailed Specification: Joint Service Lightweight Integrated Suit Technology (JSLIST) Coat and Trouser, Chemical Protective*. MILDTL-32102. Washington, DC: US Department of Defense, 2002: 1-61. Available at *https://quicksearch.dla.mil/qsDocDetails.aspx?ident_number=211488*. Accessed May 22, 2019.
49. US Army Medical Deparment Center and School: *CBRN Decontamination: Multiservice Tactics, Techniques, and Procedures for Chemical, Biological, Radiological, and Nuclear Decontamination*. Fort Sam Houston, TX: US Army Medical Deparment Center and School, 2006.
50. Timperley CM, Abdollahi M, Al-Amri AS, et al.: Advice on assistance and protection from the Scientific Advisory Board of the Organisation for the Prohibition of Chemical Weapons: Part 2. On preventing and treating health effects from acute, prolonged, and repeated nerve agent exposure, and the identif. *Toxicology*. 2019; 413: 13-23. doi:10.1016/j.tox.2018.11.009.
51. Masson P, Lushchekina SV: Emergence of catalytic bioscavengers against organophosphorus agents. *Chem Biol Interact*. 2016; 259: 319-326. doi:10.1016/j.cbi.2016.02.010.
52. Falach R, Sapoznikov A, Alcalay R, et al.: Generation of highly efficient equine-derived antibodies for post-exposure treatment of ricin intoxications by vaccination with monomerized ricin. *Toxins*. 2018; 10(11): 466. doi:10.3390/toxins10110466.
53. Gal Y, Mazor O, Alcalay R, et al.: Antibody/doxycycline combined therapy for pulmonary ricinosis: Attenuation of inflammation improves survival of ricin-intoxicated mice. *Toxicol Rep*. 2014; 1: 496-504. doi:10.1016/j.toxrep.2014.07.013.
54. Bailey MM, Heddleston JM, Davis J, et al.: Functionalized, carbon nanotube material for the catalytic degradation of organophosphate nerve agents. *Nano Res*. 2014; 7: 2-12. doi:10.1007/s12274.
55. Sharma N, Chaudhary M, Butola BS, et al.: Preparation, characterization and evaluation of the zinc titanate and silver nitrate incorporated wipes for topical chemical and biological decontamination. *Mater Sci Eng C*. 2019; 96: 183-196. doi:10.1016/j.msec.2018.10.056.
56. Ruxton K, Head CR, Clewes RJ, et al.: Detection and identification of chemical warfare agents using mid wave infrared active hyperspectral imaging. *Proc SPIE*. 2018; 10629: 1062904-1-18. doi:10.1117/12.2302519.

Appendix II Article as Submitted

Original Article

Design and characterization of multi-use research for particulate hazards and environmental exposures (MURPHEE) aerosol test chamber

Megan L. Steele[a], Emily M. Titus[b], George P. Lemmer[b], Jacob M. Denney[c], Jeremy M. Slagley[c], Casey W. Cooper[c], Robert M. Eninger[d]

[a]Integrative Health & Performance Sciences, UES, Inc, Beavercreek, OH, USA, [b]Department of Systems Engineering and Management, Air Force Institute of Technology, Centauri Contractor, Wright-Patterson AFB, OH, USA, [c]Department of Systems Engineering and Management, Air Force Institute of Technology, Wright-Patterson AFB, OH, USA, [d]HQ Air Force Materiel Command, Office of the Command Surgeon, Wright-Patterson, AFB, USA

CONTACT Megan L. Steele msteele@ues.com Integrative Health & Performance Sciences, UES, Inc, Beavercreek, OH, 45432, USA.

ABSTRACT

Aerosol test chambers are used to contain aerosols during experiments to protect researchers and provide a stable research environment. This work describes the design and characterization of a novel test chamber, the Multi-Use Research for Particulate Hazards and Environmental Exposures (MURPHEE) Chamber. Design was made modular to accommodate current and future research needs, although it was not possible to ensure laminar airflow. Characterization methods consisted of air velocity mapping as well as spatial variability of ultrafine particulate aerosols. Air speeds within the chamber varied but were homogenous enough for confidence in data collection. Particulate size distributions were similar, but there was high variability in the counts, leading experiments to require large sample sizes. In addition, a computational fluid dynamics model was created and validated using the data to guide future work and allow planning and pilot tests to be conducted more swiftly and with less cost.

1. Introduction

Test chambers are used when conducting aerosol research to protect the health of researchers, prevent cross contamination of the lab and test environment, and maintain the aerosol in a well-defined space. Based on the ultimate aims of the research, chamber design must consider materials of construction, the point of introduction of study aerosols, and location of any sampling ports (Lidén et al. 1998; Lundgren 2006). Temperature, pressure, and relative humidity can all have substantial effects on aerosol characteristics so researchers must decide from the outset if the chamber should be designed to control these parameter or if it is sufficient to simply monitor them (Hagerman et al. 2014; Isaxon et al. 2013; Lidén et al. 1998; Lundgren 2006; Rønborg et al. 1996). Even after construction, work cannot begin without a thorough understanding of the chamber characteristics, to include the achievable air velocities, airflow patterns, spatial and temporal variability of particle movement, and air exchange rates and mixing behavior of the chamber (Isaxon et al. 2013; Lidén et al. 1998; Lundgren 2006; Lundgren et al. 2006; Pieretti and Hammad 2018).

Environmental test chambers are commonly characterized in conjunction with computational fluid dynamics (CFD) techniques to verify and validate models and code (Li et al. 2007; Lin et al. 2005; Lucci et al. 2018; Zhang et al. 2005). Computational fluid dynamics has been used to model fluid flow of indoor environments for several decades, with the work of Nielsen (1974) being the oft cited dissertation regarding flow in air-conditioned environments using full scale models and numerical solutions as the basis for CFD models in the present day. When considering any fluid flow, the fundamental set of equations used to describe the conservation of momentum and mass transport are the Navier-Stokes equations, specifically in regard to incompressible turbulent flows (White 2011).

Common concerns when modeling fluid flow are turbulence intensity, fluid density and temperature, inlet velocity, and outlet conditions, along with other environmental impacts of concern (such as respiring workers, typically represented as heated manikins) (Elnahas 2005). Indoor environments are commonly modeled with comfort or contaminant mass transport as the subject of concern. Both issues are affected by fluid temperature, relative humidity, bulk air flow, contaminant

2. Chamber Design Considerations

The chamber design focused on three near-term research projects: testing the operational parameters of the Institute of Occupational Medicine (IOM) inhalable samplers, measurement of airflows and aerosol transport around a litter-bound patient, and decontamination of the same litter-bound patient. As these projects had varied requirements and future needs are unknown, design of the chamber was meant to maximize flexibility by modularity of design. Due to the size of a standard NATO litter (0.584 m wide) and space available at the research facility, it was decided that 0.762 m by 0.762 m would be the minimum cross section considered to avoid boundary effects (NATO 2013). Air velocities inside the chamber needed to be similar to those encountered in common indoor workplaces, from office spaces which approach calm environments (<0.3 m s^{-1}) to those spaces which require robust ventilation to protect against particulate hazards (≥ 0.5 m s^{-1}) (Baldwin and Maynard 1998; Bennett et al. 2018). Considering the desire to mimic workplace environments, it was determined that ambient air conditions would be suitable and no effort was made to control temperature or humidity.

Early designs aimed for laminar flow inside the chamber and basic fluid dynamics calculations were undertaken to determine if this would be possible within the space constraints. A range of air temperatures, air velocities, and chamber cross-sections were considered although

ultimately, it was determined to be impossible to achieve laminar or fully developed turbulent flow. Further information on calculations and design are included in the Supplemental Information.

As calculations indicated that achieving laminar and fully developed turbulent flow would be impossible within the real-world space constraints, the final design was a rectangular chamber with dimensions of 0.914 x 0.914 x 6.401 meters. Polycarbonate was chosen as the material for the walls, to allow researchers to monitor experiments. Though the chamber was designed to operate under negative pressure, a 0.762 cm wall thickness was deemed adequate as the magnitude of the pressure would be small. The frame was constructed out of aluminum (80/20 Inc, Columbia City, IN). The final chamber design and fabrication was conducted by the AFIT Model shop in three seven-foot sections which could be joined at the seams to form a single continuous chamber (Figure 1). The middle section included a door to allow access to the interior of the chamber. Air enters and is exhausted through banks of high efficiency particulate air (HEPA) filters. Air is moved through the chamber by a centrifugal fan equipped with a variable frequency drive located downstream (Model HDBI-120, Cincinnati Fans, Cincinnati, OH).

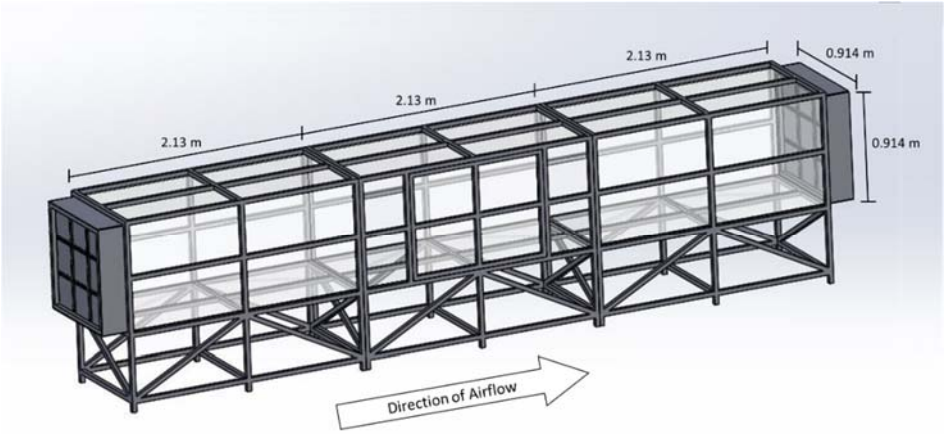

Figure 3. Final Chamber Design

After construction, all inside seams were caulked to seal them and the seams between chamber sections were sealed with Gorilla Tape® to facilitate detachment for cleaning or relocation. Once these activities were completed, characterization of the chamber could begin.

As turbulence was expected, some characterization was conducted with a flow straightener (Model: AS100, Ruskin, Kansas City, MO) in place. It was located just upstream of the door, at the seam between the first and middle chambers. All tests without the flow straightener included measurements from all three chambers, while those with the flow straightener only measured locations downstream of the flow straightener placement.

3. Chamber Characterization Methodology

3.1 Velocity Mapping

Velocity mapping was done to understand the air speed characteristics along the face of each plane and longitudinally along the length of the chamber. Mapping was done using a VelGrid attached to an AirData Multimeter data logger (Model: ADM-880c, Shortridge Instruments, Inc, Scottsdale, AZ).

The VelGrid is designed to measure the face velocity profile by covering a 0.356 x 0.356 m^2 area and recording the average velocity from 16 points within this area. In this experiment, three VelGrids were stacked and used simultaneously to cover a vertical slice of a plane in the chamber (Figure S1 in the Supplemental Information). Data were recorded using the ADM-880c in automatic mode, which were downloaded from the device at regular intervals. The ADM-880c has the capability to automatically correct measured velocities for atmospheric temperature and pressure variations, although it cannot account for fluctuation in relative humidity. This was done manually (see Supplemental Information) by using the air temperature and relative humidity collected by a Kestrel 4000 Pocket Weather Tracker (KestrelMeter.com, Boothwyn, PA) which was set to record data every 20 minutes.

To measure the velocity in the aerosol chamber, it was divided into imaginary blocks of 0.305 m x 0.305 m x 0.305 m. Starting in chamber 1, the chamber was labelled in 0.305-meter (1-foot) increments along the z-axis (Figure 2). The chamber was lettered along the x-axis, with the cube on the side of the chamber furthest from the door being labelled 'A', the middle labelled 'B', and the one nearest the door labelled 'C'. In addition, each VelGrid was given a number, used to designate the height it measured within the chamber, although the words 'high', 'middle', and 'low' are used for clarity.

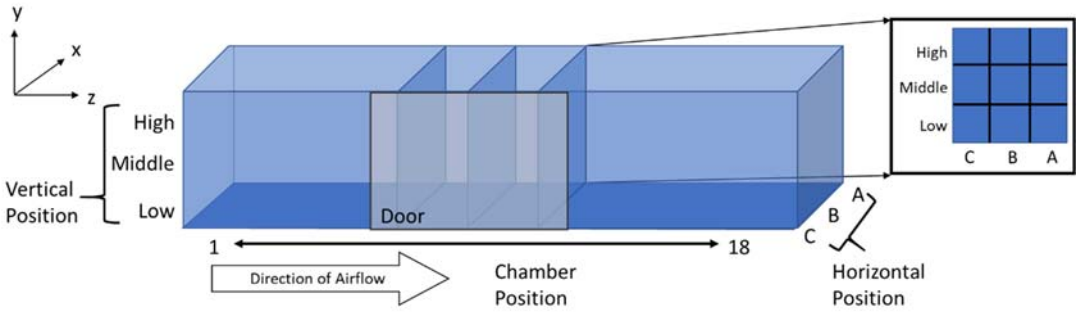

Figure 4. Chamber Measurement Locations

In the initial measurement of air velocity, the three VelGrids were stacked by attachment to a ring stand. The face of the VelGrids was positioned at each measurement location in the chamber, using tape marks on the chamber to ensure alignment. Once the VelGrids were positioned, the ADM-880c data loggers were attached and turned on to begin recording data. The chamber door was closed, the two side seams were sealed with tape, and the fan was turned on.

For each run, the fan was dialed up through the desired speeds using the variable frequency drive. In order to characterize the velocity across the full range of the fan, three frequencies were chosen: 16 Hz, 30 Hz, and 60 Hz. It was determined that 60 Hz would provide an air speed of 1 m s^{-1}, 30 Hz would provide 0.5 m s^{-1}, and 16 Hz would provide 0.2 m s^{-1}. From this point on, the fan settings will be referred to by the speed, rather than the frequency. The lower end was chosen to be slightly above the limit of detection of the ADM-880c data logger (0.127 m s^{-1}). For each run, the fan was dialed to 0.2 m s^{-1} and allowed to stabilize for a minute before a three-minute measurement period began. After the measurement period, the fan was dialed to 0.5 m s^{-1}, given a minute to stabilize and then measured for three minutes. Finally, the fan was dialed to 1 m s^{-1} and the stabilization and measurement periods were repeated. Once the measurements for 1 m s^{-1} were taken, the fan was turned off, the chamber opened, and the VelGrids were moved to the next measurement location along the x-axis. For the initial set of data, measurement locations were done sequentially (1A, 1B, 1C, 3A, 3B, 3C, etc.).

To validate the repeatability of measurements, certain locations within the chamber were selected for duplicate measurements on different days. One third of the original sampling locations were sampled for repeatability (14 of 39 without the flow straightener, and 9 of 27 with the flow straightener in place). Further information on sampling locations and methods are found in the Supplemental Information.

In addition to the initial air speed characterization, the air velocities were measured while clean air ran through the dust generator to ensure that the introduction of another air stream did not significantly disrupt the established airflow patterns. Sampling planes were chosen based on those planes with the most consistent air velocities. Two planes were chosen for use when the flow straightener was not present (5 and 7) and two planes which could be used when the flow straightener was in place (8 and 10). These measurements were repeated with two different settings on the dust generator, a high and low flow, to ensure that the full operational range of the dust generator could be used without significant effect on the established airflow patterns. Final analysis showed no impact to the established patterns so aerosol studies commenced.

3.2 Spatial Variability

Spatial variability of the chamber was examined using UltraFine Arizona Road Dust (ARD) (Particle Technology Inc., Arden Hills, MN) lofted by a rotating brush generator (RBG) 1000 dust generator (Palas GMBH, Karlsruhe, Germany) while real-time measurements were obtained with a particle counter. Measurements were taken in the same planes as were sampled with clean air (5 and 7 without the flow straightener, and 8 and 10 with the flow straightener in place).

Sampling probes channeled dust from the chamber to an optical particle sizer, OPS model 3330 (TSI, Inc., Shoreview, MN) to obtain particle distribution and concentration. One OPS reading was taken for two minutes, then the probe was moved to a new location (Figure 5). The end of the sampling probe was positioned in the center of each grid square. Sampling was not isokinetic as the opening of the probe was perpendicular to airflow, though any errors due to this would be equivalent for each location.

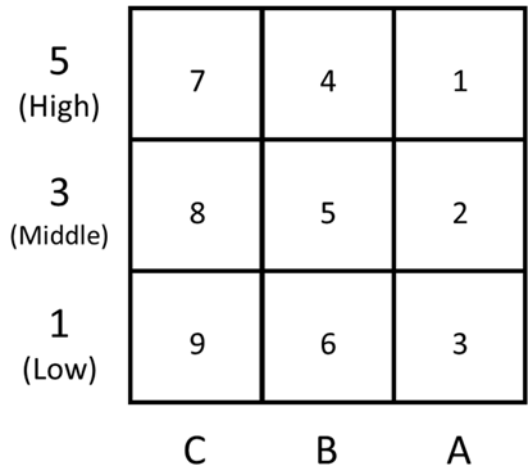

Figure 5. OPS Reading Positions in a Cross-Sectional Plane

For initial tests, the fan was set to 0.5 m s^{-1}. After the fan was turned on, the RBG dust generator was turned on. The compressed air line was set to 80 psi (5.51 x 10^5 Pa), and the pressure regulator on the RBG was set to 1 bar (10^5 Pa). The feed rate was set to 60 mm/hr. This gave a run time of approximately 40 minutes in most cases based on the amount of the reservoir filled. The brush speed was set to 1200 revolutions per minute per the manufacturer recommendation. Fifteen samples were taken per plane and experiments repeated on multiple days to capture inter-day variability.

3.3 Computational Fluid Dynamics Model Development

This study used COMSOL Multiphysics® (version 5.4), a multiphysics solver which uses a finite element method (COMSOL 2018). The model was a standard k-ε turbulence method with steady state conditions considering gravity. To account for hydrostatic pressure, a two-equation model using Reynolds Averaged Navier-Stokes (RANS) and wall functions was used. This model is recommended for used with high Reynolds numbers and low Mach numbers indicating incompressible flow, which is representative of the exposure chamber flow conditions (CFD

Module User's Guide 2018). The standard k-ε model is robust and commonly used to model airflow around bluff bodies which is an important consideration for future work.

The aerosol chamber was imported to COMSOL software from a 3-dimensional computer-aided design (CAD) file that allowed for an accurate digital representation of the chamber as the computational domain. The model was created full size and used the HEPA filter bank as the inlets, one for each filter, with additional inlets at the door to account for improper seals. An 11-inlet model was designed which accounted for leaks in the door as recorded with hot wire anemometer described below. This model was deemed to be the best representative model of the exposure chamber based on the velocity profile obtained during characterization.

The model considered each of the 9 HEPA filters as an inlet boundary condition with the velocity determined by measuring face velocity at the filter exterior with a hot wire anemometer (Table 1). During the process of model development, the best results applied a 10% increase to the observed face velocity measurement. An additional 2 inlets were included at the bottom of the door to represent leaks. The outlet boundary condition was constant pressure set at the location of plane 21. The initial conditions were set by the experimentally determined conditions at plane 1 with pressure set to 0.971 atm, temperature set to 294 K and velocity of 0.51 m s^{-1} (representative of average chamber velocity).

Table 16. Exterior Filter Face Velocity

Filter Location	Average Velocity (fpm)	[m s^{-1}]	Standard Deviation
A-Low	144.6	[0.735]	1.67
B-Low	136.0	[0.691]	2.12
C-Low	124.0	[0.630]	1.22

A-Middle	126.0	[0.640]	2.35
B-Middle	112.4	[0.571]	1.14
C-Middle	116.0	[0.589]	2.24
A-High	130.8	[0.664]	3.63
B-High	123.2	[0.626]	1.10
C-High	130.0	[0.660]	1.22

The governing equations are the RANS equations with transport equations for k and ε shown (Equation 1 and 2). The experimental conditions reflected steady temperature as there were no heat sources or sinks within the exposure chamber. Gravity was considered to account for hydrostatic pressure and larger particle settling for applicability to future experiment. The geometry for the exposure chamber was created using CAD software with the design specifications and post-construction measurements. The mesh consisted of 1,262,836 elements with 1,040,112 tetrahedral, 11,418 pyramid, and 211,306 prism elements.

$$\rho \frac{\partial k}{\partial t} + \rho \boldsymbol{u} \cdot \nabla \mathrm{k} = \nabla \cdot \left(\left(\mu + \frac{\mu_T}{\sigma_k} \right) \nabla k \right) + P_k - \rho \varepsilon \quad \textbf{(1)}$$

$$\rho \frac{\partial \varepsilon}{\partial t} + \rho \boldsymbol{u} \cdot \nabla \varepsilon = \nabla \cdot \left(\left(\mu + \frac{\mu_T}{\sigma_\varepsilon} \right) \nabla \varepsilon \right) + C_{\varepsilon 1} \frac{\varepsilon}{k} P_k - C_{\varepsilon 2} \rho \frac{\varepsilon^2}{k} \quad \textbf{(2)}$$

Table 17. Nomenclature for Equation 1 and 2

Variable	Definition	Equation/Value
μ_T	Turbulent Viscosity	$\mu_T = \rho * C_\mu \left(\frac{k^2}{\epsilon} \right)$
ρ	Fluid Density - depends on	Constant for incompressible flow

	temperature, pressure, and fluid	
C_μ	Constant	0.09
k	Turbulent Kinetic Energy	Equation 1
ε	Turbulent Dissipation Rate	Equation 2
u	Velocity Field	User Input
∇	Gradient/Partial Differential	
μ	Fluid Dynamic Viscosity - relates the shear stress and shear rates of a liquid	
σ_k	Constant	1.0
P_k	Production Term	$P_k = \mu_T \left(\nabla \mathbf{u} : (\nabla \mathbf{u} + (\nabla \mathbf{u})^T) - \frac{2}{3}(\nabla \cdot \mathbf{u})^2 \right) - \frac{2}{3}\rho k \nabla \cdot \mathbf{u}$
T	Temperature - user defined reference temperature or calculated from other model inputs	
σ_ε	Constant	1.3

$C_{\varepsilon 1}$	Constant	1.44
$C_{\varepsilon 2}$	Constant	1.92
B	Surface roughness (Constant or user defined)	5.2
κ_v	von Kárman constant	0.41

The measured velocity profile was compared to numerical simulation by averaging the computed solutions across the face of the imaginary blocks (i.e. 1A-low, with 9 blocks per plane). The velocity field solutions were exported from COMSOL Multiphysics® and sorted, filtered, and averaged using Python (version 3.7.1, Jupyter Notebook version 5.7.4) to return the velocity profile average for each block. When comparing measured and simulated values, a total of 117 squares were considered from the characterization. The comparison was made based on the confidence interval (C.I.) of measurements from the ADM-880c. Locations that were measured multiple times were considered highly variable if repeated measurements fell outside the C.I. of the original measurement and thus were not considered ideal for model verification and validation. Locations where repeated measurements all fell within the respective C.I.s were considered good locations for validation and weighted more heavily in analysis. Locations that were only measured once were considered based on the C.I. of the single measurement.

Of 117 squares, 9 were considered highly variable based on the criteria (7.70%). There were a remaining 54 squares (46.15%) with multiple measurements and 54 (46.15%) with only a single measurement. For model validation purposes, if the simulated value fell within the

observed range with C.I., it was considered a valid simulated value with less emphasis given to highly variable locations due to the larger inclusion range.

4. Analysis and Results

4.1 Chamber Measurement Results

Velocity data were visualized as contour plots using the open source software R (Version 3.6.0). Breakpoints for the velocity were chosen based on the VelGrid's precision, ± 3% ± 7 fpm (± 3% ± 0.03556 m s^{-1}) (Shortridge Instruments 2015). When plotted, data for the entire chamber without a flow straightener showed unevenness of flow throughout the chamber, though the least variability was observed in the middle slice of the chamber, away from horizontal position C (Figure **6**4). Velocity plots for when the fan operated at 0.2 m s^{-1} and 1 m s^{-1} are available in the

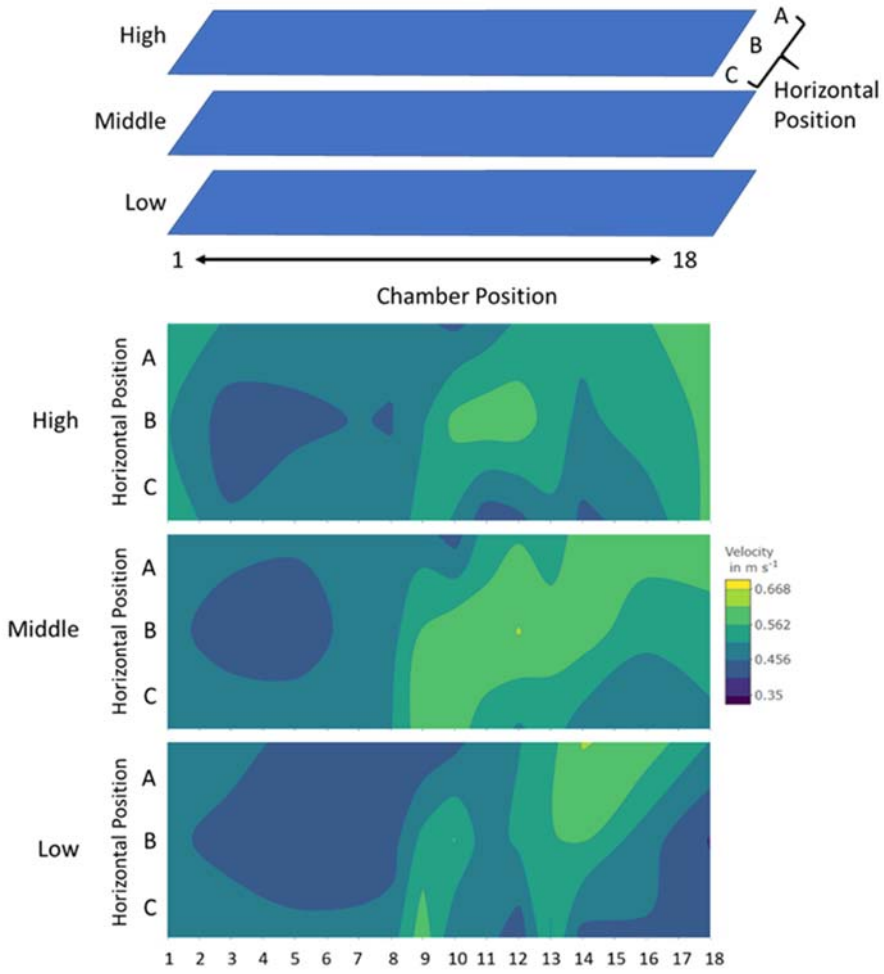

Supplemental Information. All three fan speeds showed velocity extremes at chamber locations 9 and 12, indicating gaps in the door.

Figure 6. Vertical Velocity Profiles in the Chamber at 0.5 m s^{-1}, no Flow Straightener

Plotted data for flow-straightened air followed the same pattern observed without the flow straightener (Figure 5). The straightener was placed at chamber position 7, in hopes that it would improve stability in sections 8 – 13, allowing for experiments to take place within easy reach of the only access point, the door. Despite the flow straightener, disturbances at chamber positions 9 – 12 persisted. For this reason, data are only presented moving forward for the cases when the flow straightener was not in place. Profiles for 0.2 m s^{-1} and 1 m s^{-1} and all other figures pertaining to measurements taken with the flow straightener in place are available in the Supplemental Information.

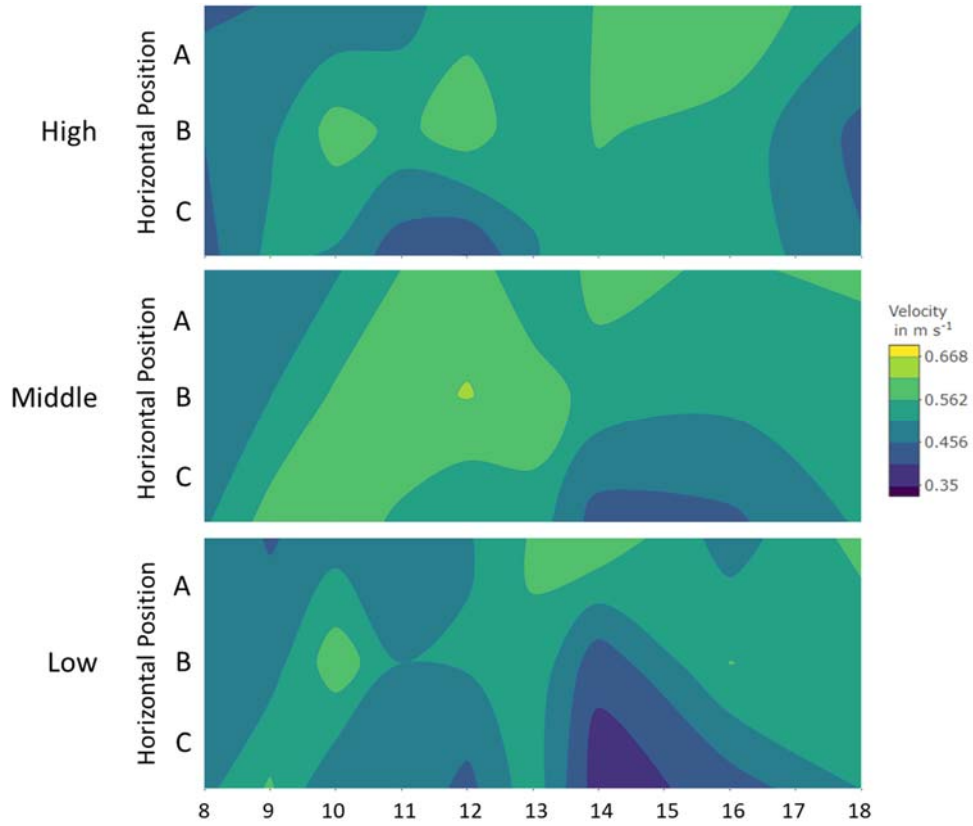

Figure 7. Vertical Velocity Profiles in the Chamber at 0.5 m s^{-1}, with Flow Straightener

Considering the uneven profiles collected along the chamber length, measurements were taken across different days to verify the repeatability of measurements. In Figure **8**, the initial

measurements are shown as black dots. Measurements collected on subsequent days are shown as red and blue dots. The pink ribbon shows the uncertainty surrounding the initial measurements. The Grubbs' test was used to determine any data points that were outliers (α = 0.05). The only outliers found were in the 0.2 m s^{-1} data (see Supplemental Information). Results were similar for velocities measured with the flow straightener. Repeated measurements at 0.2 m s^{-1} and 1 m s^{-1} are available in the Supplemental Information. The variability observed was deemed controlled enough to proceed with further characterization without modification of the chamber.

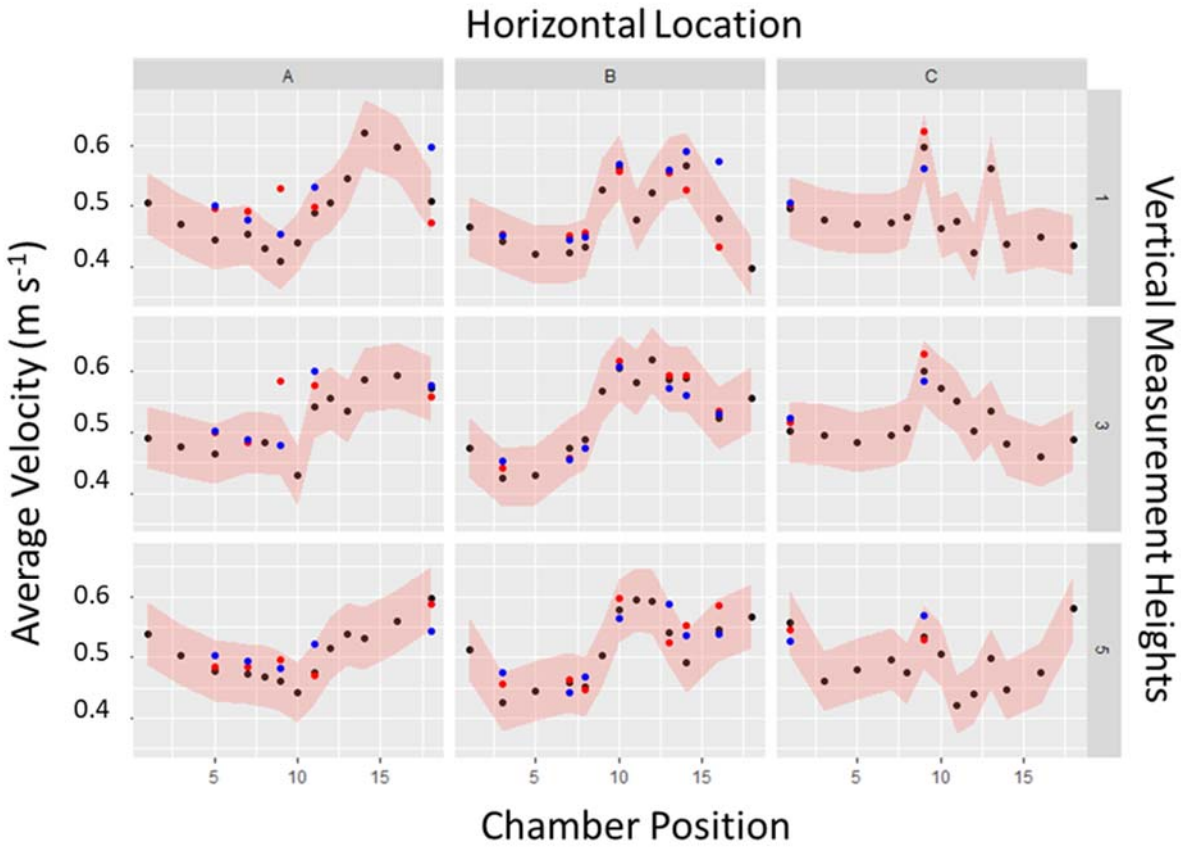

Figure 8. Day-to-Day Variability in Average Velocity at 0.5 m s^{-1}, no Flow Straightener

Velocity data were evaluated qualitatively and quantitatively for normality using quantile-quantile plots and the Shapiro-Wilk test. Data collected without a flow straightener did not behave normally; however, those collected with the flow straightener in place did behave normally (Figure 9).

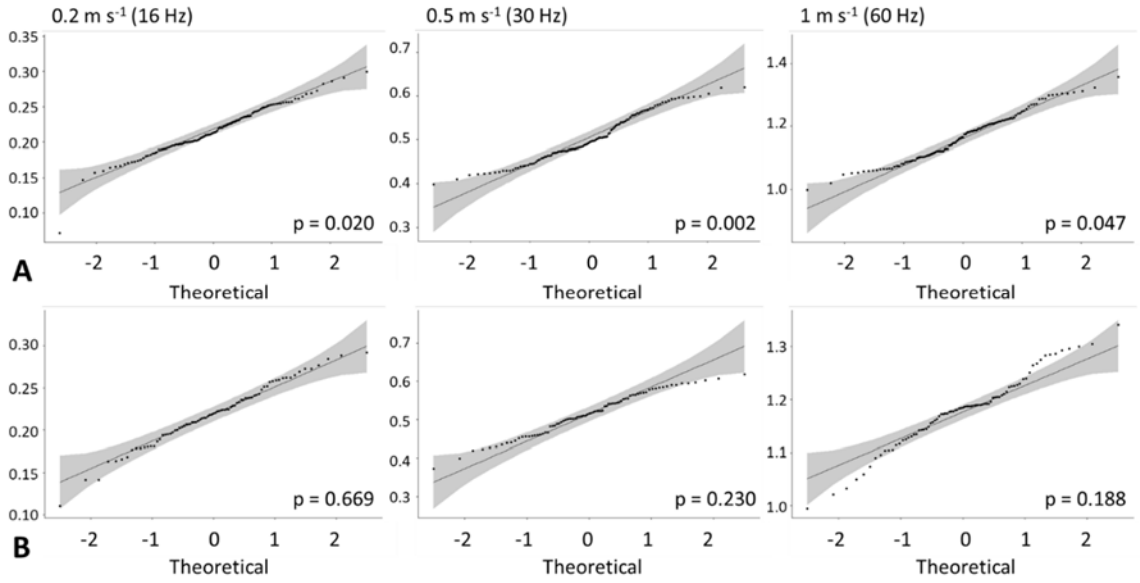

Figure 9. Quantile-Quantile Plots of Velocity Measurements: A) no Flow Straightener; B) with Flow Straightener

Data were tested for equal variance using Levene's test for data procured without the flow straightener and Bartlett's test for those procured with the flow straightener. A significance of 0.05 was chosen as the cutoff. **Error! Reference source not found.** shows the results of Levene's test for a variety of conditions: the longitudinal chamber position alone, the chamber position with regard to the vertical position, the chamber position with regard to the horizontal position, and the horizontal position with regard to the vertical position. Of these conditions, it was desirable to achieve either equal variance along the chamber length or equal variance within one plane at a specific chamber position. With respect to only the chamber position, equal

variance could not be assumed for fan speeds 0.5 and 1 m s^{-1}. The null hypothesis could not be rejected for any fan speed when considering the horizontal and vertical position, suggesting that in a plane at a specific chamber location, equal variance exists. While equal variance for chamber position with respect to the vertical or horizontal positions failed to reject the null, these conditions were not physically meaningful as they implied a long rectangular prism with equal variance, but unequal velocities. It is unlikely any sampling scenario would rely on that specific combination of conditions.

Table 18. Results of Levene's Test for Equal Variance for Velocity Data without Flow Straightener

Air Velocity, m s^{-1} (Fan Frequency, Hz)	Chamber Position only			Chamber Position, Vertical Position			Chamber Position, Horizontal Position			Horizontal Position, Vertical Position		
	Df	F	Pr(>F)	Df	F	Pr(>F)	Df	F	Pr(>F)	Df	F	Pr(>F)
0.2 (16)	12	1.7	0.077	38	0.502	0.990	38	0.502	0.990	8	0.771	0.629
0.5 (30)	12	3.200	0.0006	38	0.597	0.959	38	0.597	0.959	8	1.100	0.370
1.0 (60)	12	2.705	0.0032	38	0.528	0.984	38	0.528	0.984	8	0.558	0.810

These results for the horizontal and vertical position interaction were qualitatively evaluated through boxplots (Figure 10). The conclusion remains the same though the extent of the variances is visually more apparent.

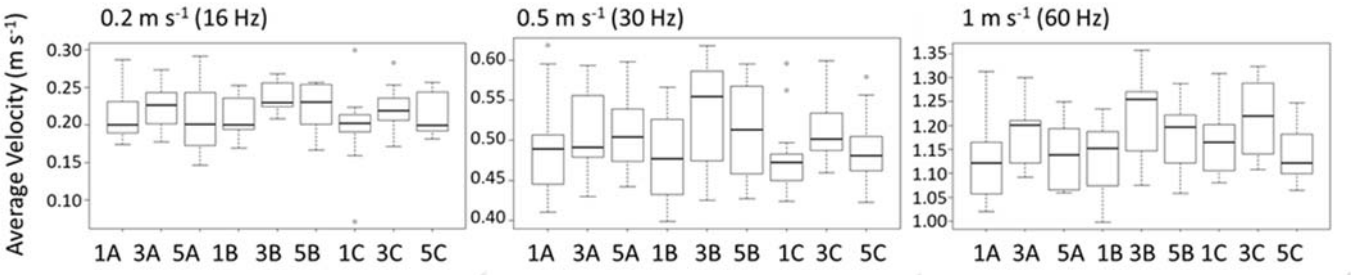

Figure 10. Variance of Velocity Profiles for without Flow Straightener Data

Planes 5 and 7 without the flow straightener and planes 8 and 10 with the flow straightener were chosen for further characterization. Every two-minute sample at a single

location in the plane was transformed from raw counts to the mass mean diameter through the process described below. Next, the geometric mean of each bin was computed (Equation 3) where d_i is the midpoint of the ith bin and n_i is the number of particles in that bin. N represents the total number of bins.

$$\text{Geometric Mean} = \left(\prod_{i=1}^{N} d_i^{n_i}\right)^{\frac{1}{N}} \quad \textbf{(3)}$$

The midpoint for each particle size bin of the optical particle counter (OPC) was determined by averaging the extremes of the range. The volume of the particle this midpoint represented was calculated using Equation 4 where $d_{midpoint}$ is the diameter of the midpoint of the bin in meters, assuming a spherical particle shape.

Equation 1. Volume of Particle

$$\text{V}(\text{m}^3) = \frac{\pi\left(d_{midpoint} * 10^{-6}\right)^3}{6} \quad \textbf{(4)}$$

The mass of the particles counted in each bin was computed with Equation 5, which assumed a particle density (ρ) of 500 kg/m^3 per the manufacturer's safety data sheet (SDS).

$$\text{Mass (mg)} = (\rho * count * particle\ volume) * 10^6 \quad \textbf{(5)}$$

Each bin was normalized by dividing the mass by the bin width, resulting in a frequency/µm. The frequency was converted to a fraction by dividing the previous value by the total mass observed in all bins. The cumulative mass was calculated by dividing the mass per bin by the total mass of all bins.

The natural log of the midpoint diameter per bin was taken and this value multiplied by the number of particles in the bin. The average of this column was the count mean diameter (CMD) (Equation 6).

$$\text{CMD (µm)} = \frac{\sum_{i=1}^{N} n_{particles,bin\ i} * \ln\left(d_{midpoint\ of\ bin\ i}\right)}{N} \quad \textbf{(6)}$$

For the mass mean diameter (MMD), the natural log of the midpoint particle diameter for the bin was multiplied by the mass in the bin. The average of all the bin values was the MMD (Equation 7).

$$\text{MMD } (\mu\text{m}) = \frac{\sum_{i=1}^{N} mass_{particles,bin\ i} * \ln\left(d_{midpoint\ of\ bin\ i}\right)}{N} \quad \textbf{(7)}$$

The geometric standard deviation (GSD) for the CMD was calculated using Equation 8.

$$GSD_{CMD} = e^{\left(\frac{\sum_{i=1}^{N}\left(n_{particles,bin\ i} * \left(\ln\left(\frac{d_{midpoint,bin\ i}}{d_{CMD}}\right)\right)^2\right)}{\left(\sum_{i=1}^{N} n_{particles,bin\ i}\right)-1}\right)^{0.5}} \quad \textbf{(8)}$$

The GSD for the MMD followed a very similar process, with the exception of substituting in the MMD and mass instead of CMD and number of particles (Equation 9). Results of the preceding equations are shown in the Supplemental Information.

Equation 2. Calculation of GSD for MMD

$$GSD_{MMD} = e^{\left(\frac{\sum_{i=1}^{N}\left(mass_{particles,bin\ i} * \left(\ln\left(\frac{d_{midpoint,bin\ i}}{d_{MMD}}\right)\right)^2\right)}{\left(\sum_{i=1}^{N} mass_{particles,bin\ i}\right)-1}\right)^{0.5}} \quad \textbf{(9)}$$

The MMD calculated from each reading was plotted by horizontal position, then vertical position to discern if aerosol distribution was more stable from side-to-side or top-to-bottom in the plane. The 0.5 m s^{-1} setting yielded the most consistent results though the MMD reported at any fan setting and any location only ranged from 3.5 – 4.25 µm. The boxplots for planes 7, 8, and 10 are available in the Supplemental Information.

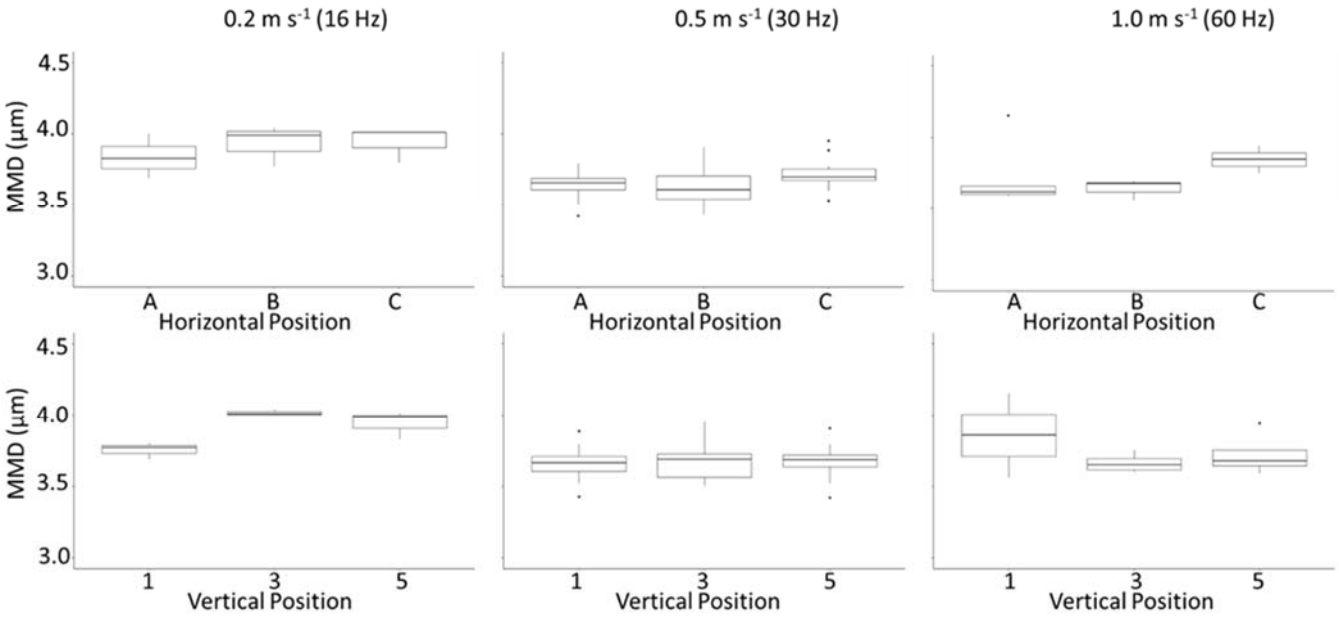

Figure 11. MMD Boxplots for Plane 5

Considering the MMD boxplots, contours of the velocity and particle count profiles were generated to visualize airflow and aerosol patterns by plane (Figure 120). These final contours served as guidelines for follow-on research sampler placement. The complete set of contour maps by plane and fan setting are found in the Supplemental Information.

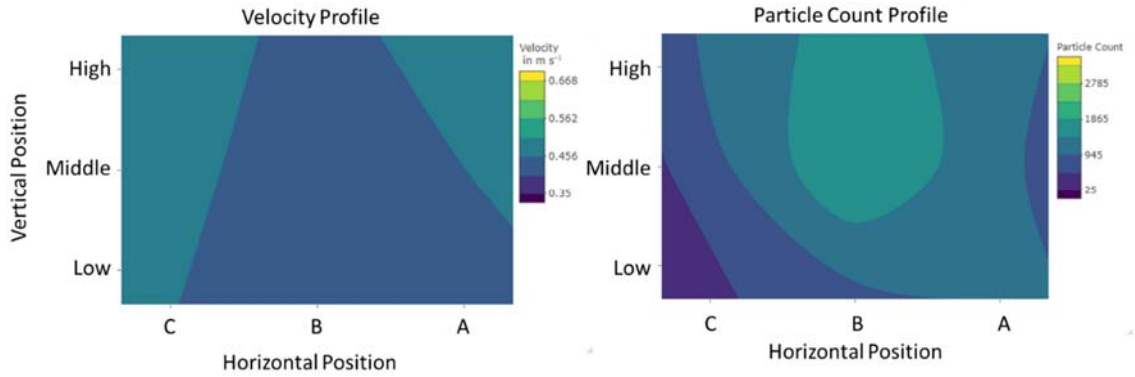

Figure 12. Velocity and Particle Count Profiles in Plane 5 at 0.5 m s^{-1}

All data gathered and analyzed confirmed initial design expectations, in that flow was turbulent and irregular along any plane of interest. Aerosol distribution data were encouraging as the distribution, if not the raw counts, were similar at all nine points sampled for each plane.

4.2 CFD Model Results

The simulation results (selected results in Table 3, see Supplemental Information for full results) fell within measurement confidence intervals as observed in experiments for 90/117 (76.92%) squares overall and 47/54 (87.04%) of the squares with multiple measurements. Four of the forty-five locations shown had model values which fell outside of the measurement C.I.s (shown in bold). Five of the nine highly variable locations (indicated by *) occurred in either plane 9 or 10, indicating the door leak was impacting consistent measurements in those locations. The model reasonably simulated the characterization based on velocity profile at each plane (Figure 11). In contrast to figures showing measured values, simulated values are only from a slice at the precise height indicated.

The mesh was left in free tetrahedral form generated by the software algorithm but had a finer mesh along the walls due to concerns with element size compared to the corners and inlet geometries. The mesh would need to be refined for future work that included more complex geometries inside the chamber but was adequate for validation of velocity profiles at each chamber location.

Table 19. Validation Points for Planes of Interest

Plane	Grid Square	Velocity ($m\ s^{-1}$)				Percent Difference
		Measured Velocity	Min (Lower	Max (Upper	Model Value	

			C.I.)	C.I.)		
5	A-Low	0.445	0.396	0.550	0.546	23%
	A-Middle	0.464	0.415	0.554	0.536	15%
	A-High	0.478	0.423	0.568	0.464	-3%
	B-Low	0.420	0.372	0.555	0.492	17%
	B-Middle*	0.430	0.381	0.605	0.496	15%
	B-High	0.446	0.397	0.562	0.451	1%
	C-Low*	0.471	0.293	0.521	0.492	4%
	C-Middle	0.483	0.433	0.573	0.484	0%
	C-High	0.481	0.431	0.551	0.487	1%
7	A-Low	0.455	0.405	0.545	0.539	19%
	A-Middle	0.484	0.408	0.542	0.533	10%
	A-High	0.473	0.403	0.546	0.458	-3%
	B-Low	0.423	0.375	0.523	0.496	17%
	B-Middle	0.474	0.405	0.577	0.505	6%
	B-High	0.458	0.393	0.534	0.457	0%
	C-Low	0.472	0.364	0.522	0.491	4%
	C-Middle	0.495	0.444	0.562	0.484	-2%
	C-High	0.497	0.414	0.547	0.488	-2%
8	A-Low	0.430	0.381	0.546	0.531	24%
	A-Middle	0.483	0.398	0.533	0.520	8%

	A-High	0.469	0.365	0.519	0.435	-7%
	B-Low	0.432	0.383	0.552	0.504	17%
	B-Middle	0.489	0.424	0.556	0.511	4%
	B-High	0.453	0.398	0.518	0.461	2%
	C-Low	0.483	0.433	0.586	0.492	2%
	C-Middle	0.506	0.453	0.580	0.492	-3%
	C-High	0.474	0.395	0.524	0.485	2%
9	A-Low*	0.410	0.362	0.579	0.522	27%
	A-Middle*	0.479	0.428	0.636	0.468	-2%
	A-High	0.462	0.412	0.548	0.694	50%
	B-Low	0.526	0.475	0.578	0.502	-5%
	B-Middle	0.568	0.516	0.621	0.525	-8%
	B-High	0.504	0.453	0.554	0.480	-5%
	C-Low	0.596	0.509	0.676	0.492	-17%
	C-Middle	0.599	0.530	0.684	0.496	-17%
	C-High	0.534	0.478	0.622	0.495	-7%
10	A-Low*	0.440	0.391	0.656	0.515	17%
	A-Middle*	0.429	0.381	0.616	0.534	24%
	A-High	0.442	0.393	0.545	0.533	21%
	B-Low	0.565	0.488	0.696	0.513	-9%
	B-Middle	0.605	0.533	0.678	0.546	-10%
	B-High	0.577	0.468	0.651	0.487	-16%

	C-Low*	0.464	0.360	0.602	0.498	7%
	C-Middle	0.572	0.519	0.671	0.501	-12%
	C-High	0.505	0.439	0.559	0.497	-2%

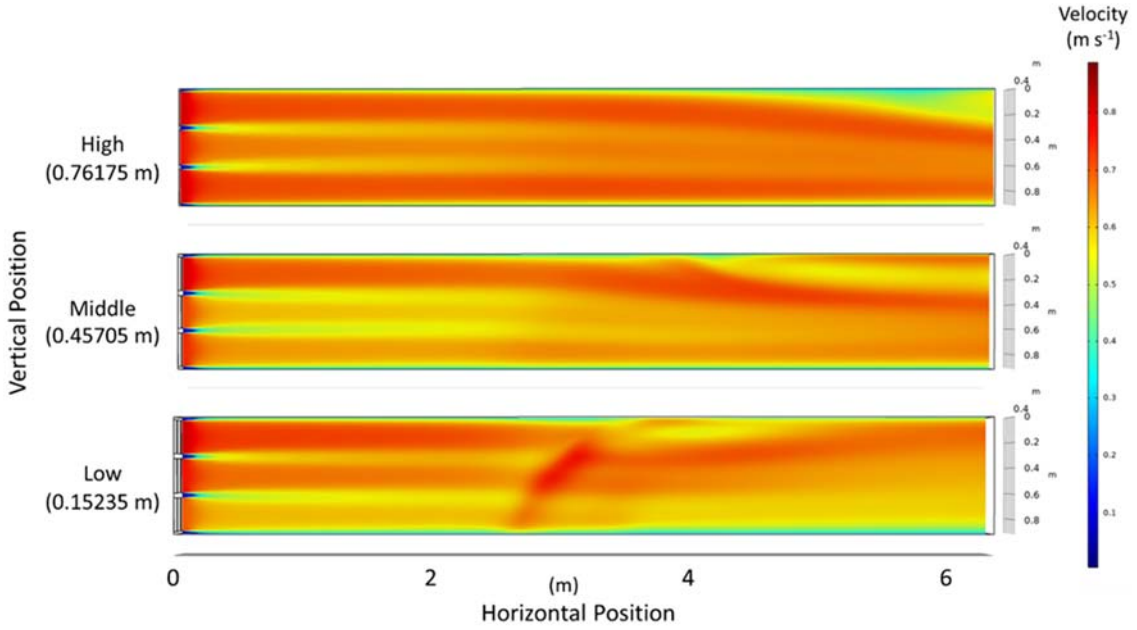

Figure 13. Airflow Visualization from CFD Model

5. Conclusions and Recommendations

A 6.401-m chamber with 0.835 m^2 cross-section was constructed to serve as a test space for aerosol studies. Air flow profiles were generated by measuring velocity at prescribed locations along the x-, y-, and z-axes. Aerosol size distribution profiles were created for the four planes identified as most stable with and without the flow straightener. Inter-day variability was deemed acceptable considering the limitations of the anemometer. This finding supports the use of the chamber for future studies without modification. While equal variance existed across x-y planes in the chamber, the magnitude of the variance was considerable. This considerable

variance suggests researchers must either collect large sample sets to detect significance among the data or restrict their activities to a smaller, better defined subsection of a given plane.

The creation of a computational fluid dynamics model validated by physical measurements will be a great asset to future research projects. It will allow researchers to predict the impact to flow behavior when different sampling apparatus are in place prior to conducting pilot research. It is apparent that improvements to the door's seal could be made and CFD models could inform an improved design as well as behavior after modification. Finally, the air flow was only characterized at three fan settings, and aerosol behavior at a single fan speed. It stands to reason that subsequent research may rely on intermediate velocities to achieve their research aims. Refinement of the current model would allow predictions to be made of flow behavior that could easily be validated with judicious sampling, rather than a repeat of the entire characterization outlined in this report. This CFD model will ultimately help save researchers time and funds.

The data collected and analyzed in this study confirm the chamber performance is stable enough for a variety of research aims. Periodic confirmation of chamber performance is recommended. Any significant changes to the setup, including replacement of the access door require a complete recharacterization. With the present setup, researchers will need to conduct pilot studies to capture any bias inherent in the selected chamber location before proceeding to full scale studies, though use of the CFD model will aid this process.

Acknowledgements

The authors would like to thank Stephanie Ohms for her help in chamber set-up, as well as UES, Inc. for their support and use of equipment and lab space.

Disclosure
No financial interest or benefit has arisen from the direct applications of this research.

References

Baldwin, P. E. J. and A. D. Maynard. 1998. A survey of wind speeds in indoor workplaces. *Annals of Occupational Hygiene* 42 (5):303–313. doi: https://doi.org/10.1016/S0003-4878(98)00031-3.

Bennett, J., D. Marlow, F. Nourian, J. Breay, A. Feng, and M. Methner. 2018. Effect of ventilation velocity on hexavalent chromium and isocyanate exposures in aircraft paint spraying. *Journal of Occupational and Environmental Hygiene* 15 (3):167-181. doi: 10.1080/15459624.2017.1401710.

CFD Module User's Guide. *COMSOL Multiphysics®*. (version 5.4). 2018. Stockholm, Sweden: COMSOL AB.

COMSOL Multiphysics®. (version 5.4). 2018. Stockholm, Sweden: COMSOL AB.

Elnahas, W. M. 2005. Effects of heating, breathing, hair style, posture, and air velocity on breathing zone concentrations for an anthropometrically-correct manikin in a wind tunnel. PhD diss., West Virginia University.

Engineers Edge, LLC. (no date) Viscosity of Air, Dynamic and Kinematic. Accessed January 3, 2020. https://www.engineersedge.com/physics/viscosity_of_air_dynamic_and_kinematic_14483.htm

Hagerman, I., C. Isaxon, A. Gudmundsson, A. Wierzbicka, K. Dierschke, M. Berglund, J. Pagels, J. Nielsen, E. Assarsson, U. B. K. Andersson, et al. 2014. Effects on heart rate variability

by artificially generated indoor nano-sized particles in a chamber study. *Atmospheric Environment* 88:165–171. doi: 10.1016/j.atmosenv.2014.02.003.

Isaxon, C., K. Dierschke, J. H. Pagels, A. Wierszbicka, A. Gudmundsson, J. Löndahl, I. Hagerman, M. Berglund, E. Assarsson, U. B. Andersson, et al. 2013. Realistic indoor nano-aerosols for a human exposure facility. *Journal of Aerosol Science* 60:55–66. doi: 10.1016/j.jaerosci.2013.02.003.

Li, J., I. Yavuz, I. Celik, and S. Guffey. 2007. Predicting worker exposure—the effect of ventilation velocity, free-stream turbulence and thermal condition. *Journal of occupational and environmental hygiene* 4 (11):864-874. doi: https://doi.org/10.1080/15459620701665688.

Lidén, C., L. Lundgren, L. Skare, G. Lidén, G. Tornling, and S. Krantz. 1998. A new whole-body exposure chamber for human skin and lung challenge experiments - the generation of wheat flour aerosols. *Annals of Occupational Hygiene* 42 (8):541–547. doi: 10.1016/S0003-4878(98)00063-5.

Lin, C. H., K. H. Dunn, R. H. Horstman, J. L. Topmiller, M. F. Ahlers, J. S. Bennett, L. M. Sedgwick, and S. Wirogo. 2005. Numerical simulation of airflow and airborne pathogen transport in aircraft cabins – part I: numerical simulation of the flow field. *ASHRAE Transactions* 111 (1):755-763.

Lucci, F., N. D. Castro, A. A. Rostami, M. J. Oldham, J. Hoeng, Y. B. Pithawalla, and A. K. Kuczaj. 2018. Characterization and modeling of aerosol deposition in Vitrocell® exposure systems - exposure well chamber deposition efficiency. *Journal of Aerosol Science* 123:141-160. doi: https://doi.org/10.1016/j.jaerosci.2018.06.015.

Lundgren, L. 2006. Large organic aerosols in a human exposure chamber: Applications in occupational dermatology and lung medicine. Thesis, Karolinska Institutet.

Lundgren, L., L. Skare, C. Lidén, and G. Tornling. 2006. Large organic aerosols in a dynamic and continuous whole-body exposure chamber tested on humans and on a heated mannequin. *Annals of Occupational Hygiene* 50 (7):705–715. doi: 10.1093/annhyg/mel027.

NATO (National Atlantic Treaty Organization). 2013. Stretchers, bearing brackets and attachment supports. NATO Standard AMedP-2.1, NATO Standardization Agency.

de Nevers, N. 2005. *Fluid Mechanics for Chemical Engineers*. 3rd ed. New York, NY: McGraw-Hill Companies.

Nielsen, P. V. 1974. Flow in air conditioned rooms: Model experiments and numerical solution of the flow equations. Ph.D. thesis, Technical University of Denmark (Aalborg Universitet).

Pieretti, L. F. and Y. Y. Hammad. 2018. Performance of a whole-body human dust inhalation challenge exposure chamber. *Toxicology Reports* 5:793–799. doi: 10.1016/j.toxrep.2018.07.004.

Rønborg, S. M., H. Mosbech, C. R. Johnsen, and L. K. Poulsen. 1996. Exposure chamber for allergen challenge: The development and validation of a new concept. *Allergy: European Journal of Allergy and Clinical Immunology* 51 (2):82–88. doi: 10.1111/j.1398-9995.1996.tb04562.x.

Shortridge Instruments (2015) Airdata Multimeter ADM-880c Manual. Scottsdale, AZ: Shortridge Instruments, Inc.

Srebric, J. and Q. Chen. 2002. An example of verification, validation, and reporting of indoor environment CFD analyses (RP-1133). *ASHRAE Transactions* 108 (2):185-194.

White, F. M. 2011. *Fluid Mechanics.* 7th ed. New York, NY: McGraw-Hill.

Zhang, Y., Y. Sun, A. Wang, J. L. Topmiller, and J. S. Bennett. 2005. Experimental characterization of airflows in aircraft cabins, part II: results and research recommendations. *ASHRAE Transactions* 111 (2):53-59.

Appendix III Supplement as Submitted

Design and characterization of multi-use research for particulate hazards and environmental exposures (MURPHEE) aerosol test chamber – Supplemental Information

Megan L. Steele[a], Emily M. Titus[b], George P. Lemmer[b], Jacob M. Denney[c], Jeremy M. Slagley[c], Casey W. Cooper[c], Robert M. Eninger[d]

[a]Integrative Health & Performance Sciences, UES, Inc, Beavercreek, OH, USA, [b]Department of Systems Engineering and Management, Air Force Institute of Technology, Centauri Contractor, Wright-Patterson AFB, OH, USA, [c]Department of Systems Engineering and Management, Air Force Institute of Technology, Wright-Patterson AFB, OH, USA, [d]HQ Air Force Materiel Command, Office of the Command Surgeon, Wright-Patterson, AFB, USA

CONTACT Megan L. Steele msteele@ues.com Integrative Health & Performance Sciences, UES, Inc, Beavercreek, OH, 45432, USA.

S2. Chamber Design Considerations

Early designs aimed for laminar flow inside the chamber and basic fluid dynamics calculations were undertaken to determine if this would be possible within the space constraints. First, the effect of temperature was considered, and the Reynolds number (Re) was determined for a range of temperatures from 55-85°F, as this represented what could reasonably be expected in indoor workplaces. For each temperature, the appropriate density and dynamic viscosity were used (Engineers' Edge no date). The square cross-section of 2.5 feet was converted to equivalent pipe diameter and air velocities from 0.1-1 m s^{-1} were considered. The Re was calculated using Equation S1.

Equation S3. Reynolds Number

$$\mathrm{Re} = \frac{Du\rho}{\mu}$$

where,

$\mathrm{Re} = Reynolds\ number$

$D = the\ pipe's\ diameter\ (m)$

$u = fluid\ velocity\ \left(\frac{m}{s}\right)$

$\mu = the\ fluid's\ \ viscosity\ (\frac{N * s}{m^2})$

$\rho = the\ fluid's\ \ density\ (\frac{kg}{m^3})$

This resulted in Reynolds number ranging from 4,265 to 59,468 (conditions of T = 85°F, u = 0.1 m s^{-1} and T = 55°F, u = 1 m s^{-1} respectively). No conditions considered resulted in laminar flow, thus turbulent flow equations were used for subsequent design iterations.

While lacking the consistent uniformity of laminar flow, it has been documented that turbulent flow can fully develop to approximate predictable behavior. For the purpose of this design, flow was considered fully developed if the boundary layers converged (de Nevers 2005). In order to determine if this condition could be met, boundary layer calculations for smooth surface with 2.5-foot cross-section were carried out. A simplified equation for boundary layer thickness on a flat plate was used, due to the difficulties involved in determining numerical solutions for turbulent airflow (Equation S2) (de Nevers 2005). Air temperature was assumed to be 21°C (the midpoint of the range tested for the Re), giving air a kinematic viscosity of 1.156 x

10-5 m2/s. The same air velocities were used as for the Re calculations and the value of z was varied from 0.5 to 12 feet.

Equation S4. Boundary Layer Thickness

$$\delta = 0.37z\left(\frac{\upsilon}{u_{infinity}z}\right)^{\frac{1}{5}}$$

where,

$\delta = boundary\ layer\ thickness\ (m)$

$z = distance\ along\ z-axis\ (m)$

$\upsilon = kinematic\ viscosity\ of\ the\ fluid\ (\frac{m^2}{s})$

$u_{infinity} = final\ velocity\ (\frac{m}{s})$

These conditions resulted in boundary layer thicknesses ranging from 0.35 to 7.08 inches (corresponding to u = 1 m s^{-1}, z = 0.5 feet and u = 0.1 m s^{-1}, z = 12 feet respectively). These calculations show that fully developed flow does not occur by the midpoint of a 2.5 ft square chamber, which adds an additional degree of difficulty, due to the need to carefully characterize all locations within the chamber in order to conduct reproducible experiments.

S3.1. Velocity Mapping

The VelGrid consists of two crossed pieces, each with a smaller crossed piece near the end of each arm which covers an area 14 x 14 inches2. There are 16 holes to capture air, four on each arm of the device as shown in Figure S1.

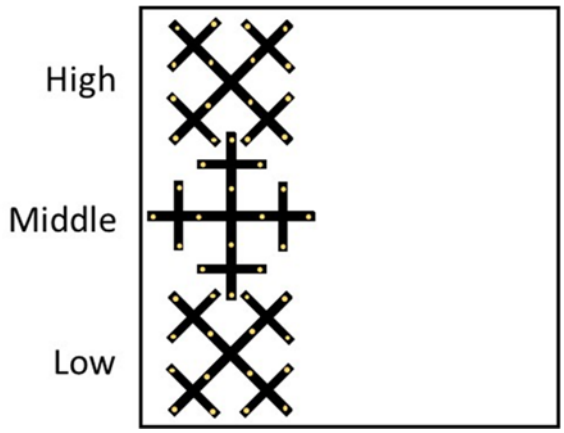

Figure S14. VelGrid Configuration in Chamber Cross-Section

The VelGrid poles were clamped at the break between the second and third sections to avoid any backwash turbulence from disturbing the velocity measurements. This was done for all measurement locations except 18 as the poles were too long so the third section was removed and the pole was clamped a third of the way from the end. For A and C positions, the middle VelGrid was positioned to touch the wall. For B position, the lowest VelGrid was positioned so the two cross arms were centered on the lower support bar of the chamber.

To determine which locations would be measured multiple times, measurement locations were sequentially assigned a number and then Excel was used to generate a random number which was then used as the location. For the third round of measurements, the same locations were sampled a third time, by sequentially assigning each one a number and then using Excel to generate a random number for the sample order.

The automatic data logging mode of the ADM-880c records data points as quickly as the machine can process them, no more than 10 seconds apart. The ADM-880c automatically corrects for temperature as shown in Equation S3.

Equation S5. Temperature Correction for Velocity

$$Local\ Density\ Velocity = Velocity\ in\ local\ density\ mode * \sqrt{\frac{460 + °F}{530}}$$

S3.1.a. Chamber Characterization Data Processing

In order to know where the three-minute measurement period started and ended in the Excel file, the data line off the ADM-880c display was recorded. The data line was recorded in an Excel sheet both when the thee-minute timer was started and when it finished.

For the initial measurements, data was downloaded from the ADM-880c after every plane (the location was known because locations were always sampled A to C). For the random measurements, data was downloaded after every location in order to maintain data integrity. Downloaded files were named by the location (distance from inlet, horizontal letter, and height, i.e. 18A-3).

There were several steps taken during the data processing. First, the CSV files retrieved from the ADM-880c were converted to Excel files and the unused columns were deleted (mainly those for other ADM-880c recording functionalities). Then the data file was cross-referenced with the data lines recorded during measurement and the measurement rows were highlighted. During this process the time for the first and last measurements were compared to ensure that a 3-minute window had been recorded. In all cases at least a 3-minute window was recorded. In a couple of instances, the end timer was not heard due to environmental noise and more than 3-minutes of data were collected. In these cases, the start time was used to determine an end row of 3-minutes.

After all of the measurement rows were marked, they were copied to a third Excel workbook to consolidate all data in one place. The location and fan setting information were input manually from the file name and then all data were copied to the new workbook. The columns containing only units were deleted as they were captured in the column headings.

Next, the recorded velocities were corrected for the relative humidity of the workspace. This was done by inserting 7 columns between the existing Temperature (°F) column and the Abs Pres (in Hg) column. These were used to convert temperature to degrees Celsius, calculate the Saturation Vapor Pressure (P_{sat}) and Vapor Pressure (P_{vapor}), contain the relative humidity data, and then calculate the corrected velocity (Equations S4, S5, and S6). The relative humidity data was copied from the downloaded Kestrel data sheet or from manually recorded points. The Kestrel was set to log data every 20 minutes. The following convention was used to assign relative humidity data to velocity readings. If a Kestrel reading was taken at 9:20:00, it was associated with ADM-880c readings between 9:20:00 and 9:39:59. Then the Kestrel reading for 9:40:00 was associated with velocity readings taken between 9:40:00 and 9:59:59. In addition, a column was added to capture the difference between the original value and the corrected value. The calculation of P_{sat} was done by using the equation behind the National Weather Services Vapor Pressure Calculator (Equation S6) (Brice and Hall No Date). After the saturation vapor pressure was calculated, it was used to calculate the vapor pressure by the relationship between relative humidity and P_{sat} (Equation S7) (Engineering Toolbox 2004). Finally, the barometric pressure (Abs Pres, recorded by the ADM-880c), recorded velocity, and vapor pressure were used to determine the corrected velocity (Equation S8).

Equation S6. Saturation Vapor Pressure

$$\mathrm{P_{sat}} = 6.11 * 10^{\frac{7.5*T}{237.3+T}}, \;\; P_{sat} = [mbar]$$

$$\mathrm{P_{[inHg]}} = 0.0295300 * P_{[mbar]}$$

Equation S7. Relative Humidity, Vapor Pressure, and Saturation Vapor Pressure Relationship

$$\mathrm{RH} = \left(\frac{P_{vapor}}{P_{sat}}\right) * 100\% \rightarrow P_{vapor} = \left(\frac{\mathrm{RH}}{100}\right) * P_{sat}$$

Equation S8. Corrected Velocity for Moist Air

$$\mathrm{V_{moist\ air}} = \frac{P_b * V_{dry}}{P_b - P_{vapor}},$$

Where:

$V_{moist\ air}$ = velocity corrected for moist air

P_b = local barometric pressure,

V_{dry} = velocity corrected for local density (T & barometric pressure)

P_{vapor}=vapor pressure

S4.1. Chamber Characterization Data Processing

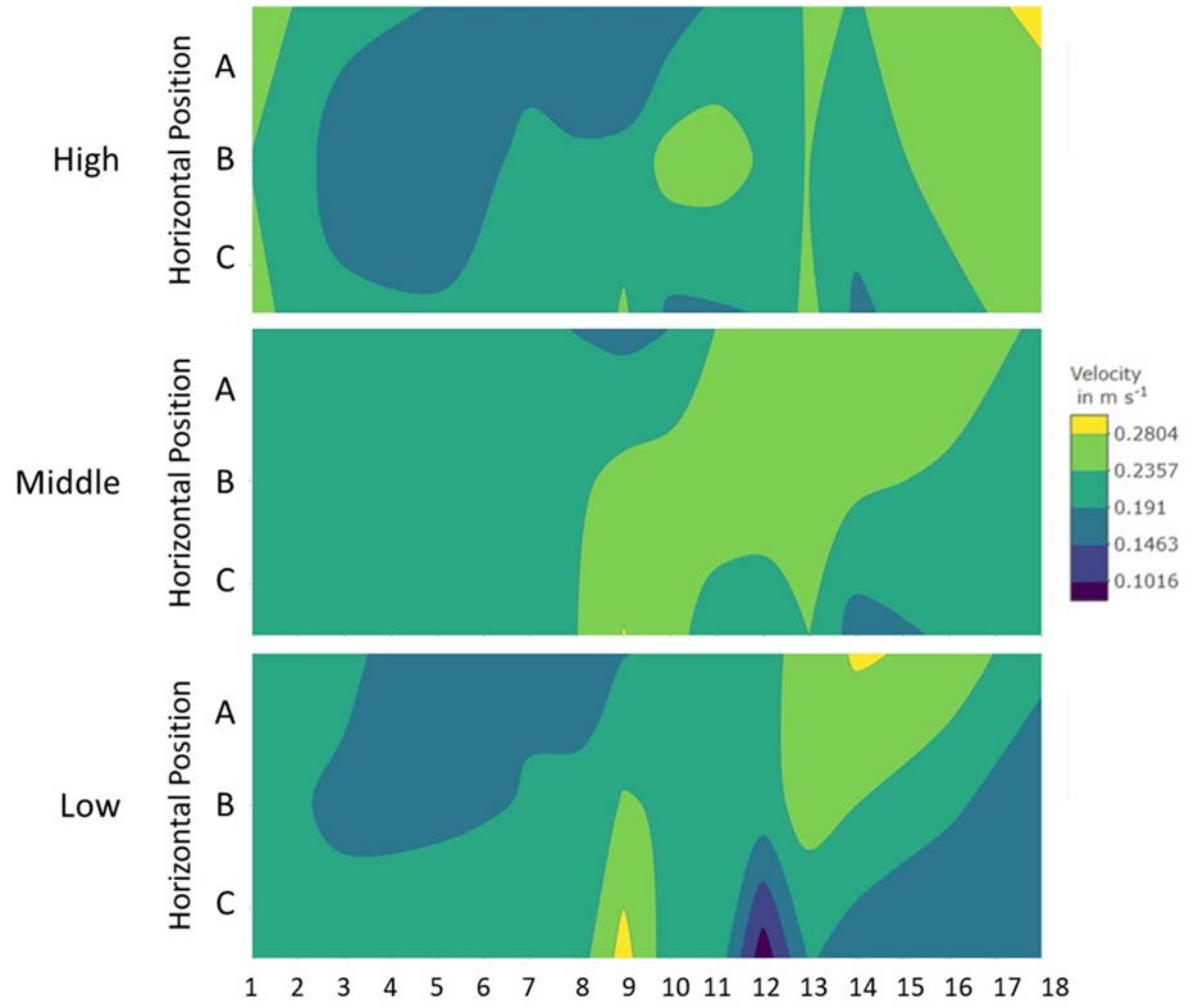

Figure S15. Vertical Velocity Profile of the Chamber at 0.2 m s^{-1} (16 Hz), no Flow Straightener

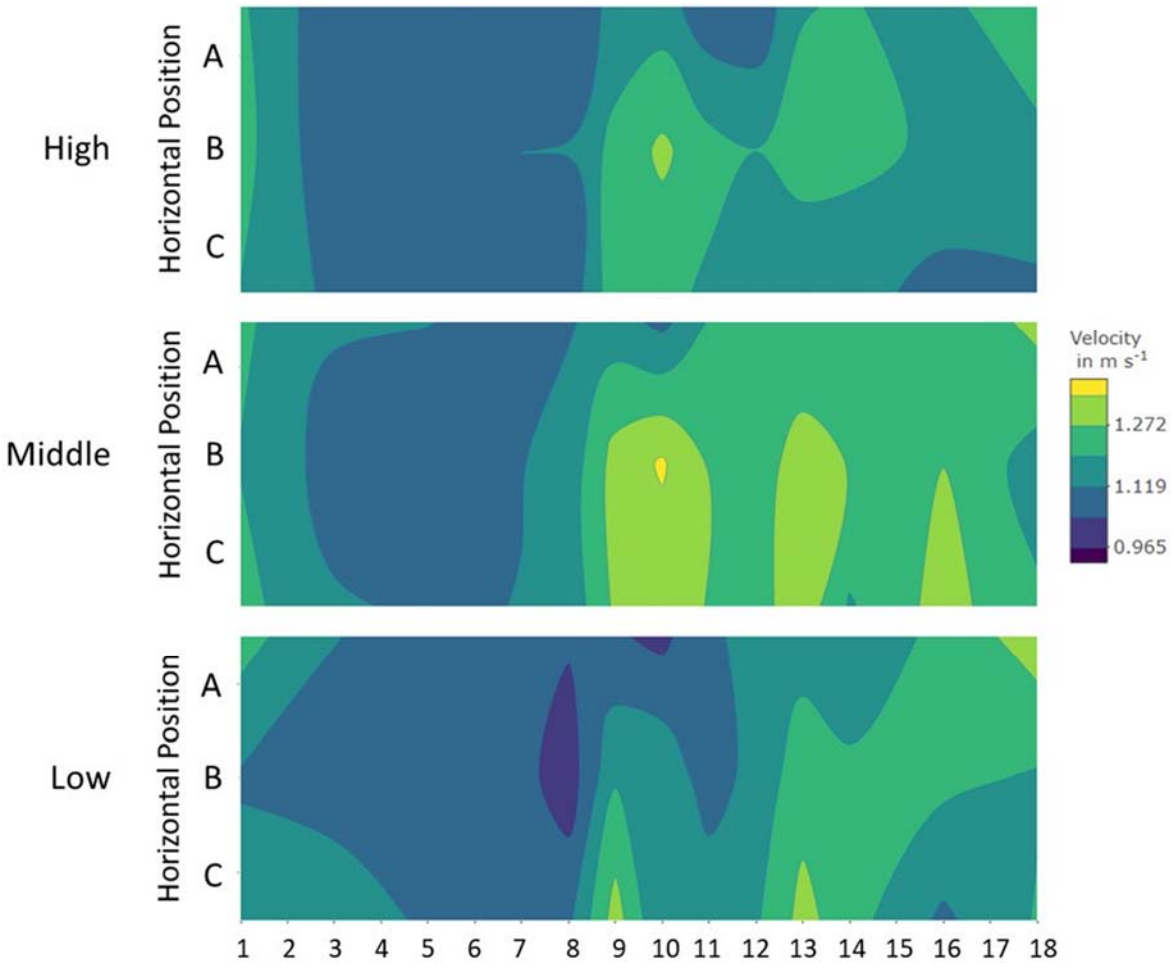

Figure S16. Vertical Velocity Profile of the Chamber at 1.0 m s^{-1} (60 Hz), no Flow Straightener

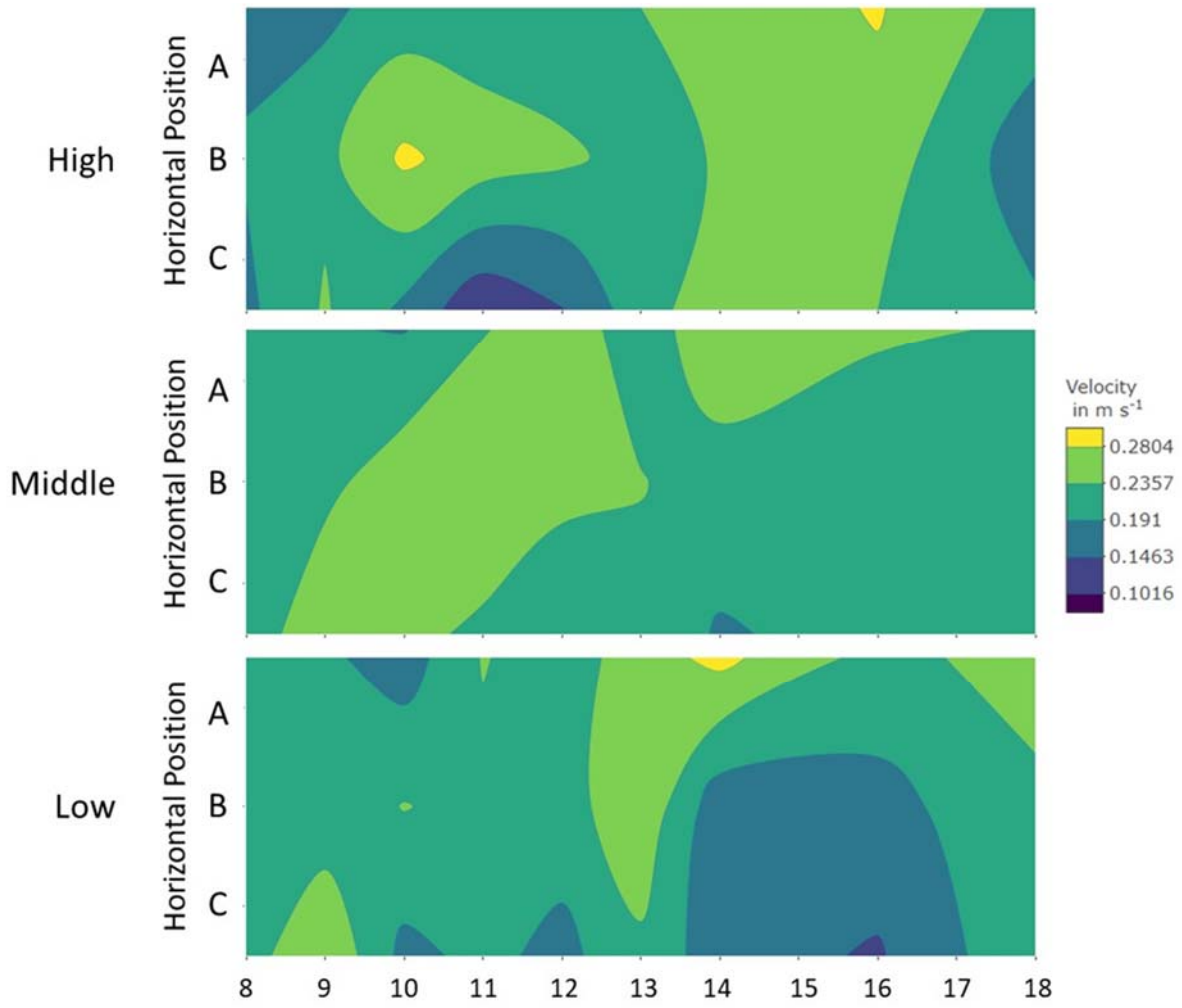

Figure S17. Vertical Velocity Profile of the Chamber at 0.2 m s^{-1} (16 Hz), with Flow Straightener

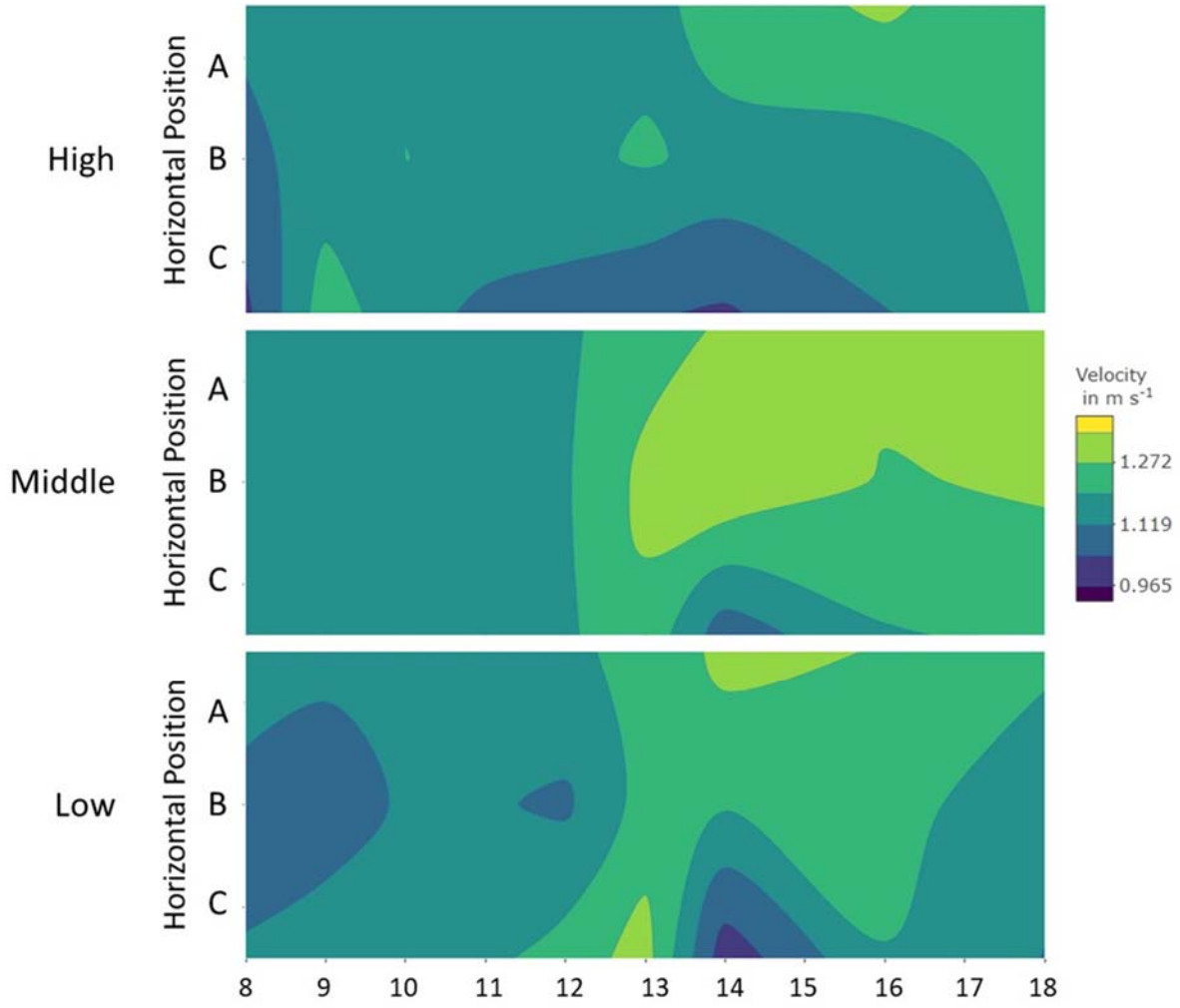

Figure S18. Vertical Velocity Profile of the Chamber at 1.0 m s^{-1} (60 Hz), with Flow Straightener

Day-to-Day Variability in Velocity Measurements

Grubbs' test was used to determine whether there were any outliers in the velocity data. One data point was shown to be an outlier at chamber position 16, suggesting transient slow velocities (Figure S6).

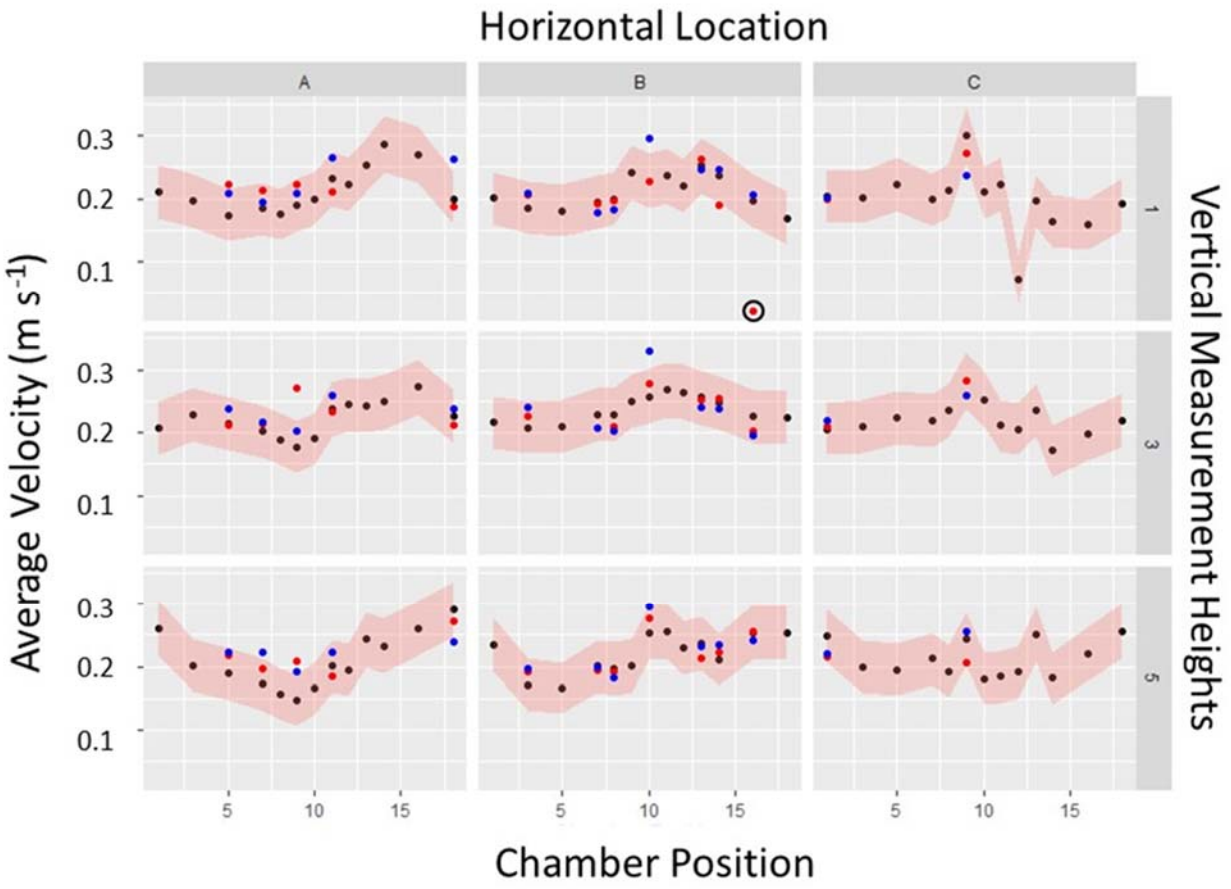

Figure S19. Day-to-Day Variability in Average Velocity at 0.2 m s^{-1}, no Flow Straightener

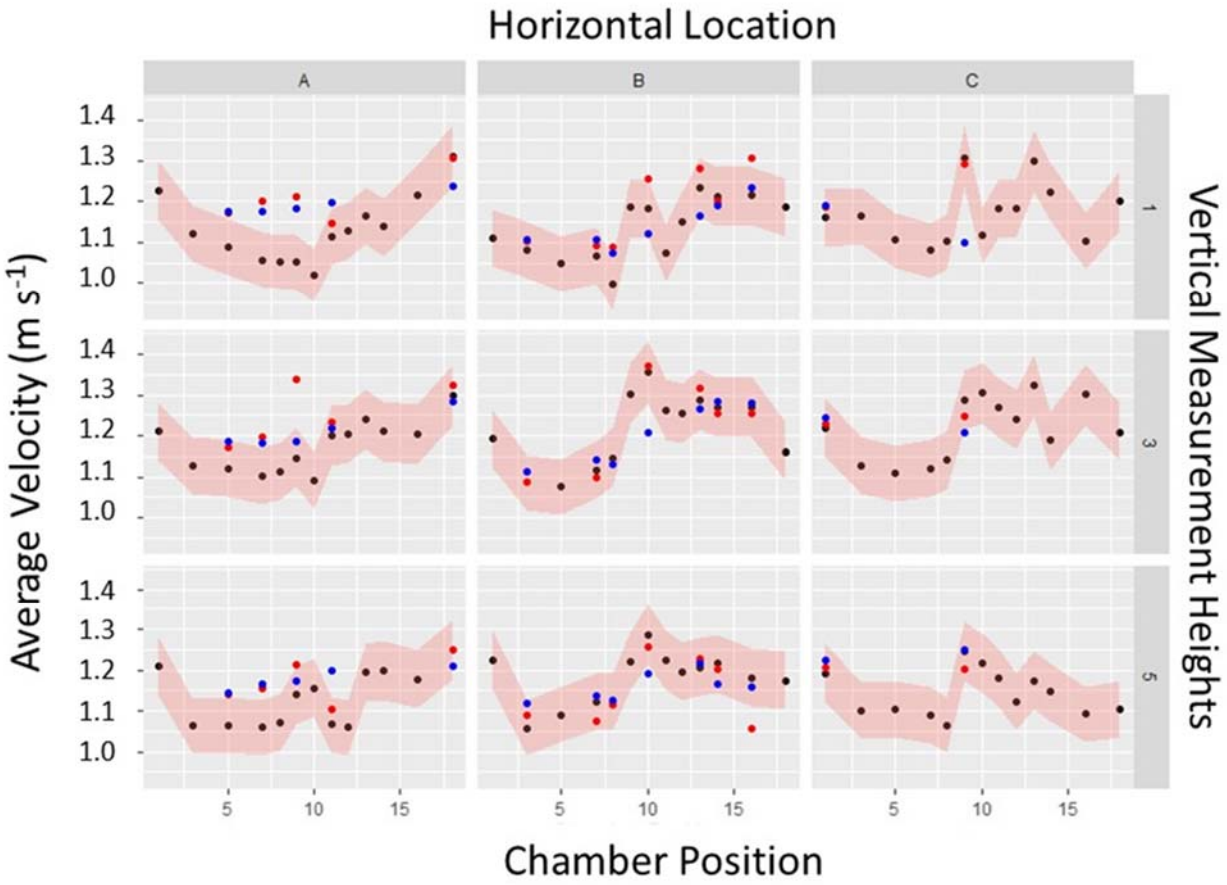

Figure S20. Day-to-Day Variability in Average Velocity at 1.0 m s^{-1}, no Flow Straightener

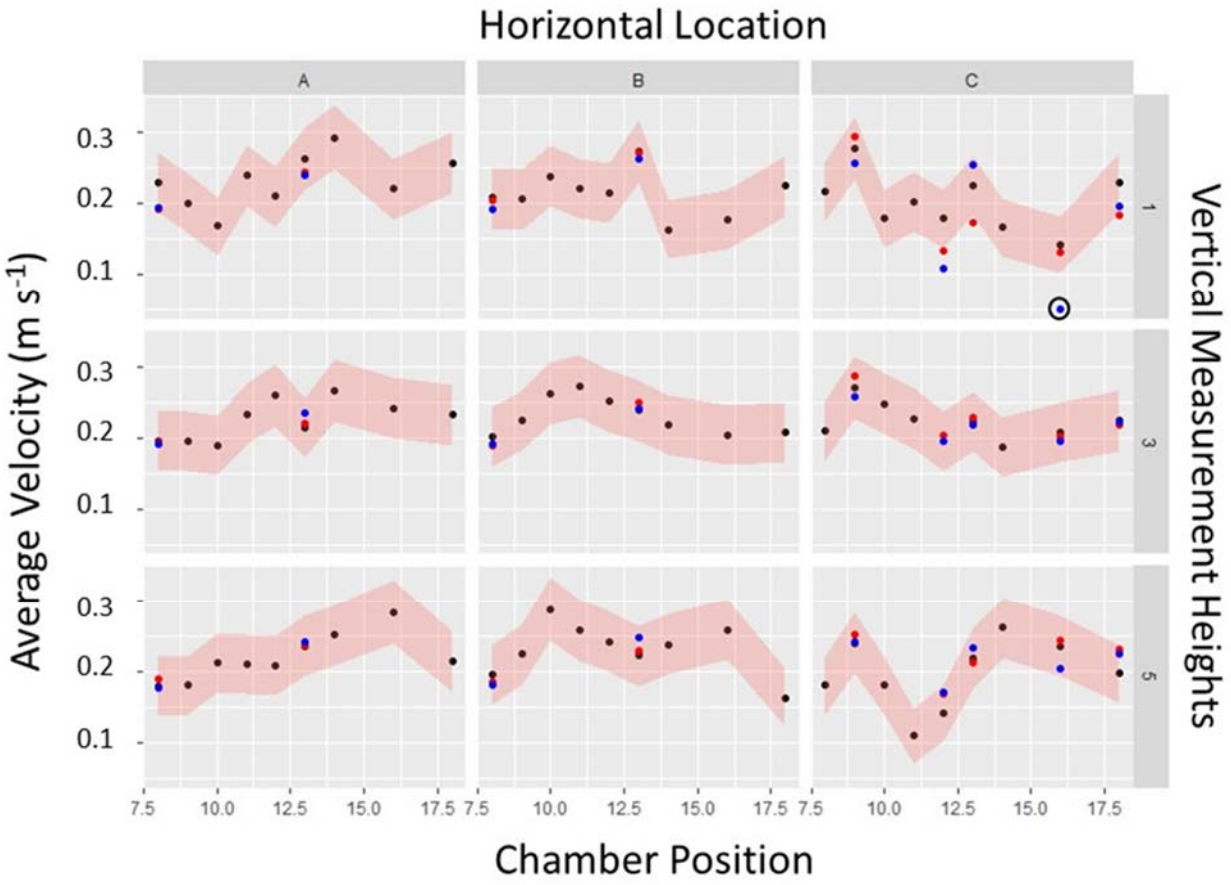

Figure S21. Day-to-Day Variability in Average Velocity at 0.2 m s^{-1}, with Flow Straightener

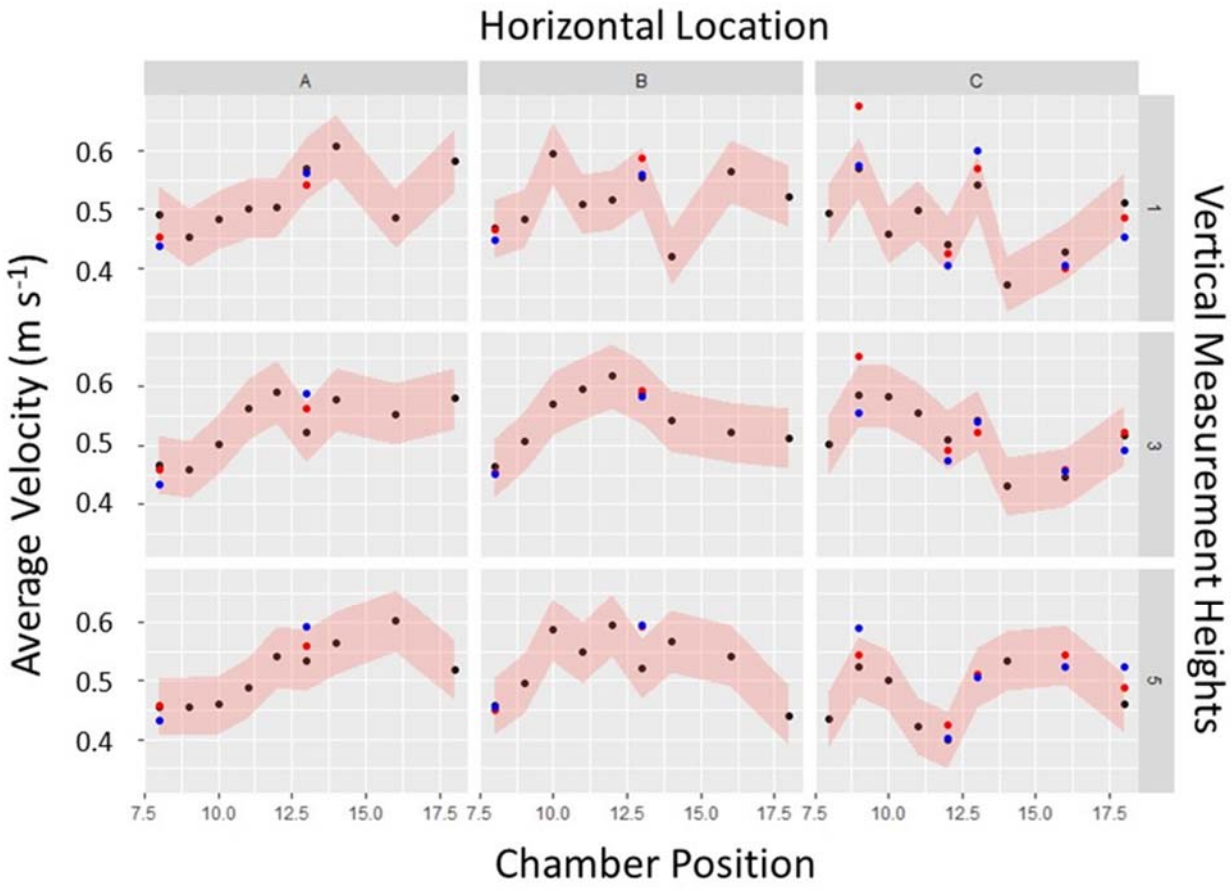

Figure S22. Day-to-Day Variability in Average Velocity at 0.5 m s^{-1}, with Flow Straightener

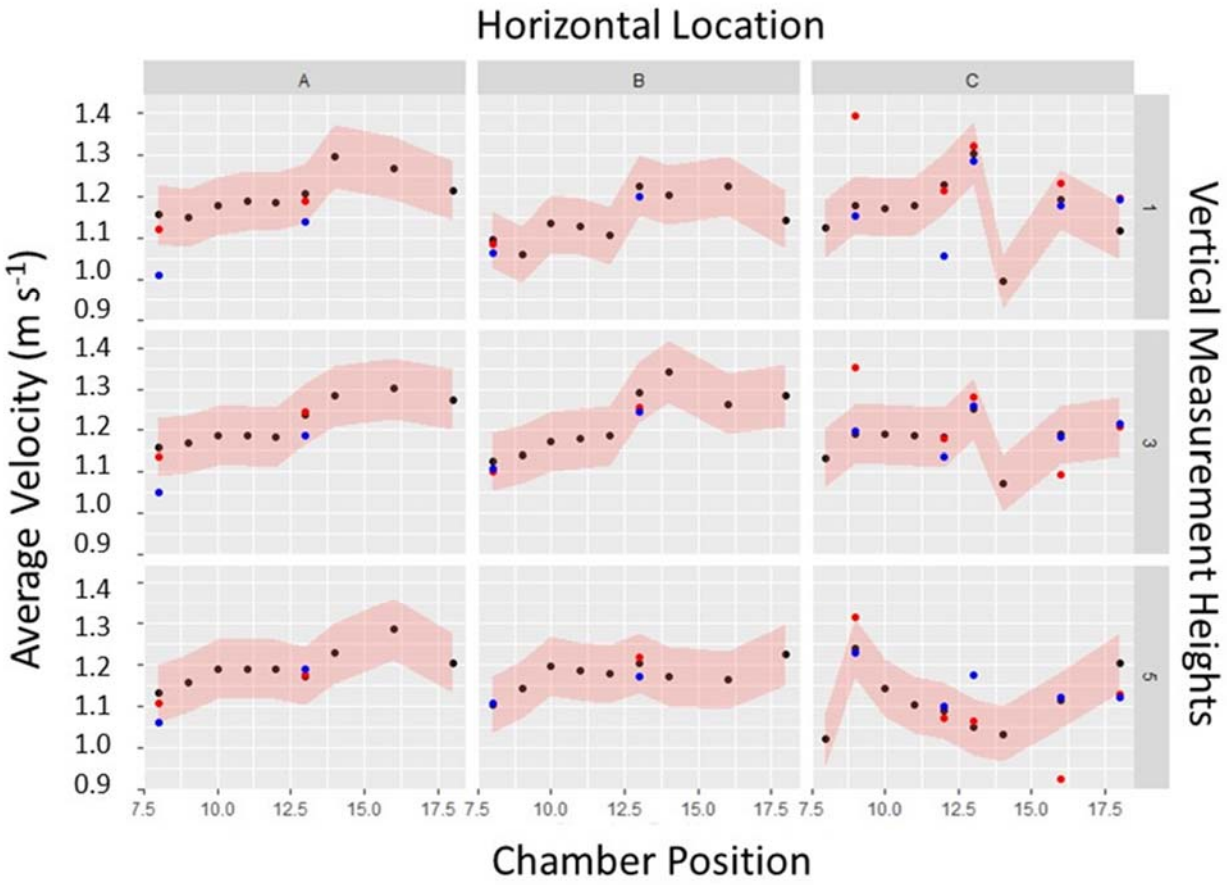

Figure S23. Day-to-Day Variability in Average Velocity at 1.0 m s^{-1}, with Flow Straightener

S4.1.a. Chamber Measurement Results and Analysis

Data collected without the flow straightener were tested for equal variance using Levene's test. In Levene's test, Pr(>F) should be less than the chosen cutoff value to reject the null hypothesis of equal variance. In this study, a significance of 0.05 was chosen as the cutoff. Data were tested for equal variance using Bartlett's test for data procured with the flow straightener. For Bartlett's test, the p-value must be less than the specified cutoff to reject the null. Data were analyzed for the same interactions as data collected without the flow straightener.

Data collected with the flow straightener, when analyzed with Bartlett's test for equal variance, generated results similar to those found in the data without the flow straightener. Only chamber position alone resulted in p-values that necessitated the rejection of the null hypothesis (Table S1).

Table S20. Results of Bartlett's Test for Equal Variance for Velocity Data with Flow Straightener

Air Velocity, m s^{-1} (Fan Frequency, Hz)	Chamber Position only			Chamber Position, Vertical Position			Chamber Position, Horizontal Position			Horizontal Position, Vertical Position		
	K^2	df	p	K^2	df	p	K^2	df	p	K^2	df	p
0.2 (16)	14.59	8	0.067	32.42	26	0.18	25.53	26	0.489	5.59	8	0.69
0.5 (30)	19.43	8	0.013	34.74	26	0.12	33.58	26	0.15	0.45	8	0.99
1.0 (60)	31.15	8	0.0001	51.07	26	0.002	47.81	26	0.006	9.76	8	0.28

Results for the horizontal and vertical position interaction were again qualitatively evaluated through boxplots (Figure S11). Variances remained large overall.

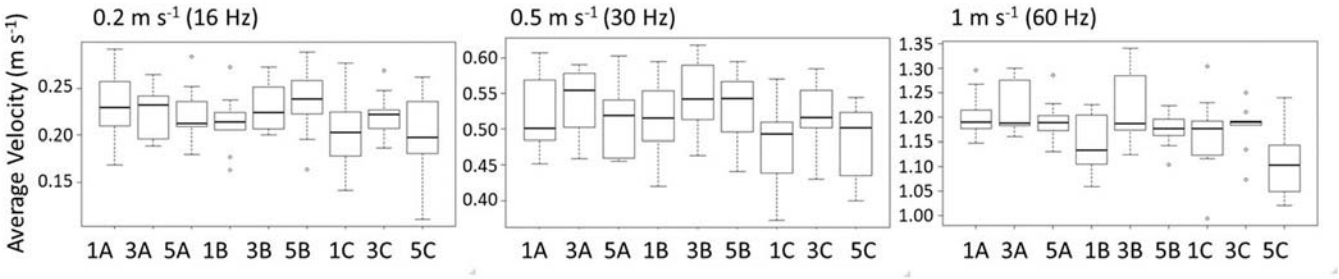

Figure S24. Variance of Velocity Profiles, with Flow Straightener

Example Determination of CMD, MMD, and GSD for Aerosol Data

Table S21. Size Distribution Calculations of Aerosol Data

Bin Width	Size Range (µm)	Midpoint	Volume (m^3)	Count	Mass (mg)	Frequency/µm	Fraction/ µm	Cumulative Mass	LN(d_i)	n_i*LN(d_i)	d_i/d_g	CMD	CMD (d_i/d_g)
0.074	0.3 - 0.374	0.337	2.00E-20	21789	2.18E-07	2.95E-06	0.119	1%	-1.09	-2.37E-07	1.20E-06	-23699.3	2802.2
0.091	0.374 - 0.465	0.420	3.87E-20	11158	2.16E-07	2.37E-06	0.095	2%	-0.87	-1.87E-07	9.79E-07	-9692.5	217.6
0.114	0.465 - 0.579	0.522	7.45E-20	5694	2.12E-07	1.86E-06	0.075	3%	-0.65	-1.38E-07	7.75E-07	-3701.6	35.5
0.142	0.579 - 0.721	0.650	1.44E-19	1951	1.40E-07	9.88E-07	0.040	3%	-0.43	-6.04E-08	4.02E-07	-840.5	173.6
0.176	0.721 - 0.897	0.809	2.77E-19	637	8.82E-08	5.01E-07	0.020	4%	-0.21	-1.87E-08	1.92E-07	-134.9	170.2
0.220	0.897 - 1.117	1.007	5.35E-19	2408	6.44E-07	2.93E-06	0.118	6%	0.01	4.49E-09	1.01E-06	16.8	1304.7
0.274	1.117 - 1.391	1.254	1.03E-18	1077	5.56E-07	2.03E-06	0.082	8%	0.23	1.26E-07	5.96E-07	243.7	982.8
0.341	1.391 - 1.732	1.562	1.99E-18	688	6.85E-07	2.01E-06	0.081	11%	0.45	3.05E-07	4.56E-07	306.4	948.7
0.424	1.732 - 2.156	1.944	3.85E-18	990	1.90E-06	4.49E-06	0.181	19%	0.66	1.27E-06	6.78E-07	657.8	1922.4
0.529	2.156 - 2.685	2.421	7.43E-18	722	2.68E-06	5.07E-06	0.204	30%	0.88	2.37E-06	3.82E-07	638.6	1879.7
0.658	2.685 - 3.343	3.014	1.43E-17	407	2.92E-06	4.43E-06	0.179	41%	1.10	3.22E-06	7.31E-08	449.1	1366.6
0.819	3.343 - 4.162	3.753	2.77E-17	256	3.55E-06	4.33E-06	0.174	56%	1.32	4.69E-06	1.31E-08	339.0	1078.9
1.020	4.162 - 5.182	4.672	5.34E-17	154	4.12E-06	4.04E-06	0.163	72%	1.54	6.36E-06	3.23E-07	238.1	796.2
1.269	5.182 - 6.451	5.817	1.03E-16	68	3.49E-06	2.75E-06	0.111	86%	1.76	6.14E-06	8.69E-07	119.2	419.7
1.580	6.451 - 8.031	7.241	1.99E-16	21	2.07E-06	1.31E-06	0.053	95%	1.98	4.10E-06	1.07E-06	41.2	152.9
1.969	8.031 - 10	9.016	3.84E-16	2	4.50E-07	2.28E-07	0.009	96%	2.20	9.89E-07	3.95E-07	5.2	20.1
10.000	10 - 20	15.000	1.77E-15	1	8.84E-07	8.84E-08	0.004	100%	2.71	2.39E-06	1.85E-06	2.7	11.8
			TOTAL:	48023	2.48E-05								

MMD Distribution Boxplots

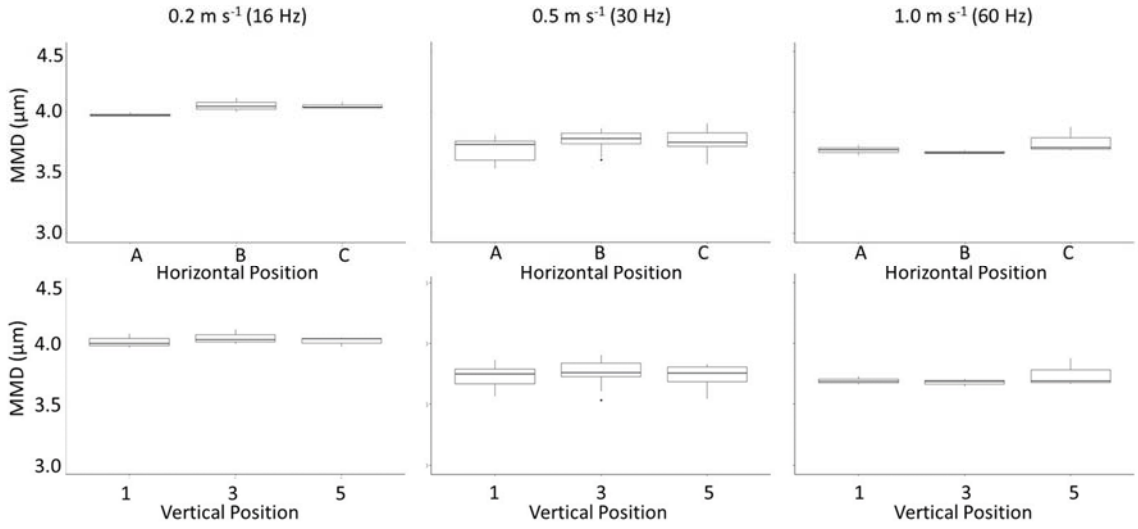

Figure S25. MMD Boxplots for Plane 7

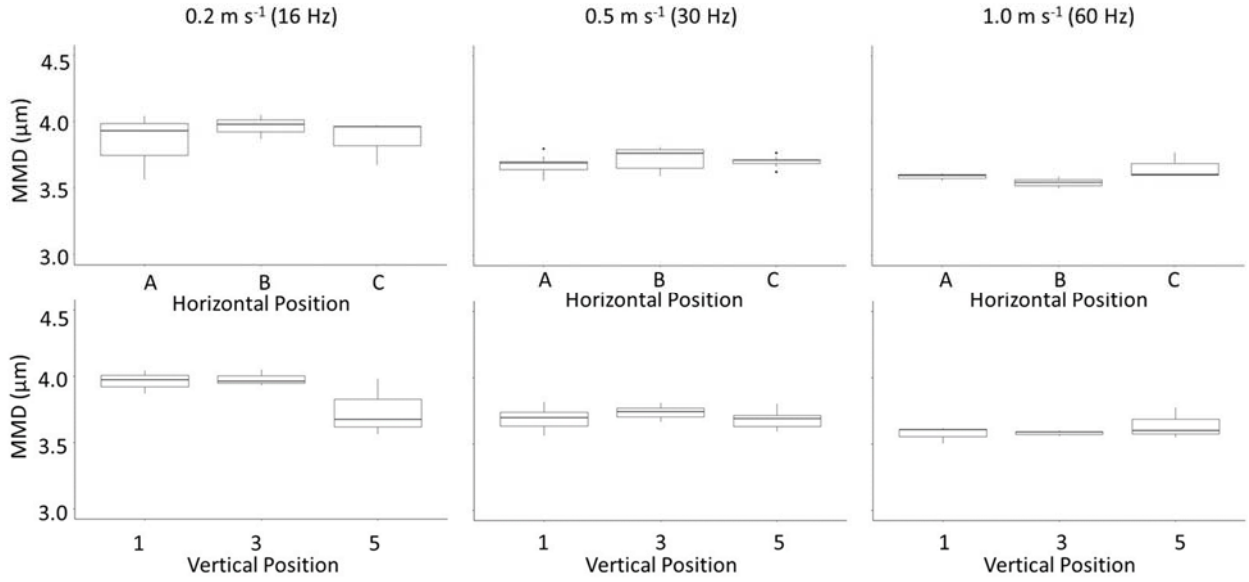

Figure S26. MMD Boxplots for Plane 8

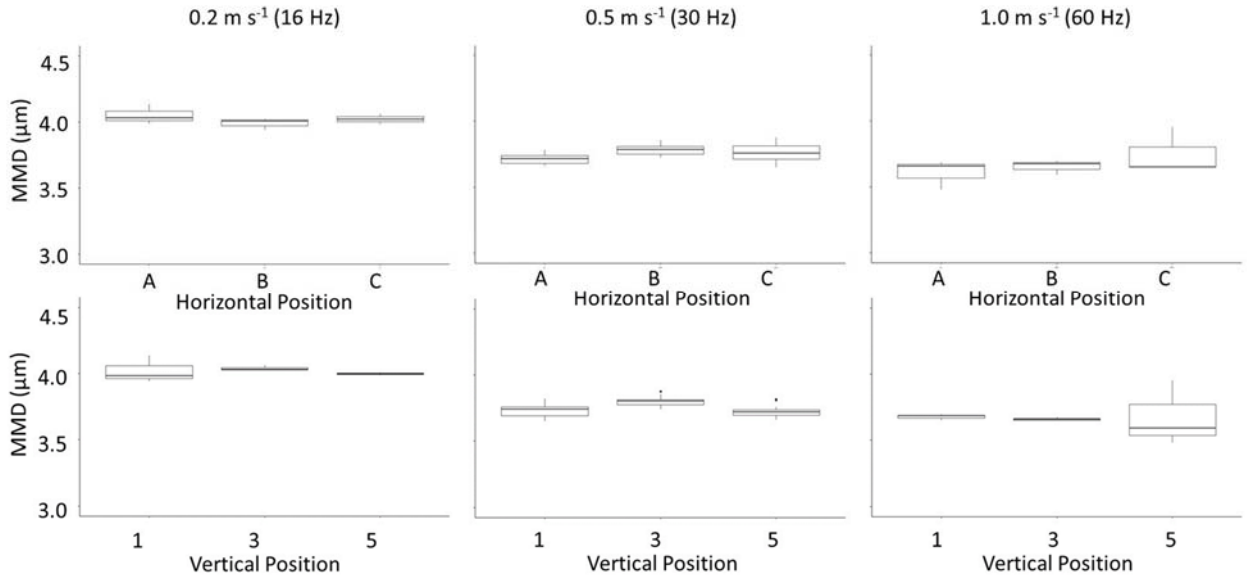

Figure S27. MMD Boxplots for Plane 10

S4.1.b. Chamber Measurement Results

Velocity and Particle Count Profiles

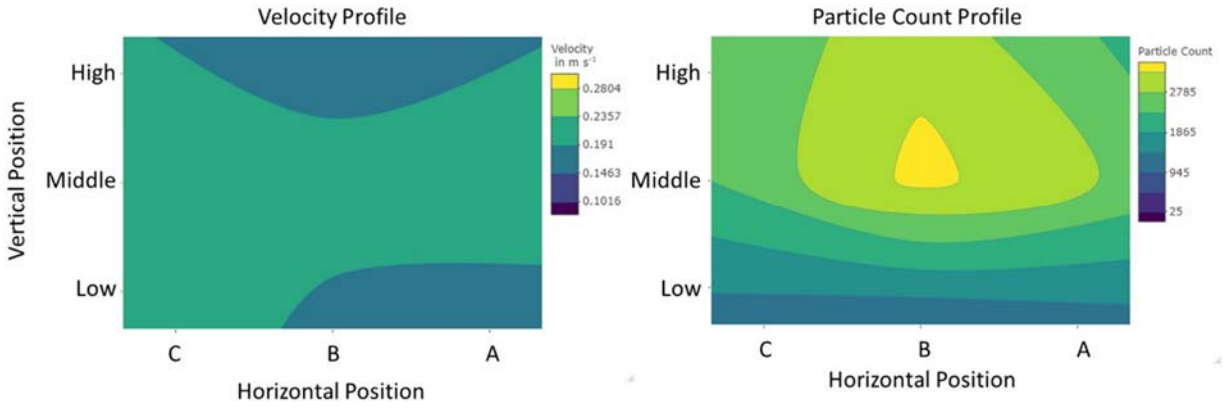

Figure S28. Velocity and Particle Count Profiles in Plane 5 at 0.2 m s^{-1}

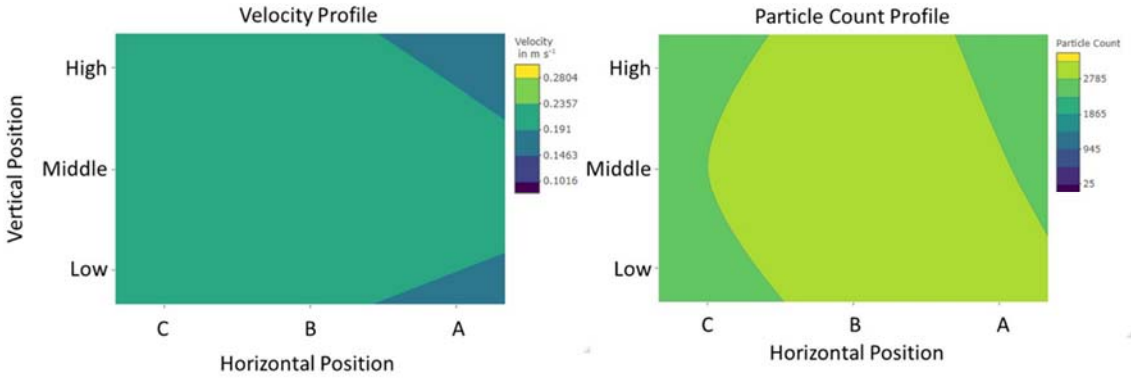

Figure S29. Velocity and Particle Count Profiles in Plane 7 at 0.2 m s^{-1}

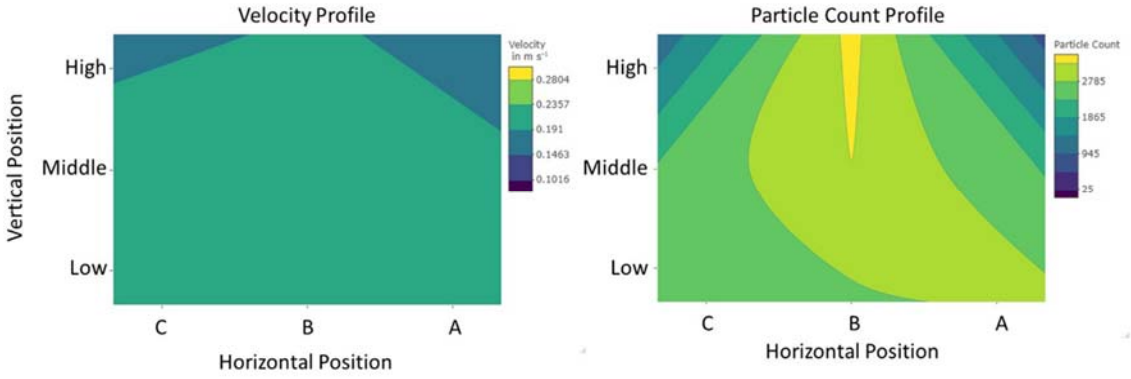

Figure S30. Velocity and Particle Count Profiles in Plane 8 at 0.2 m s^{-1}

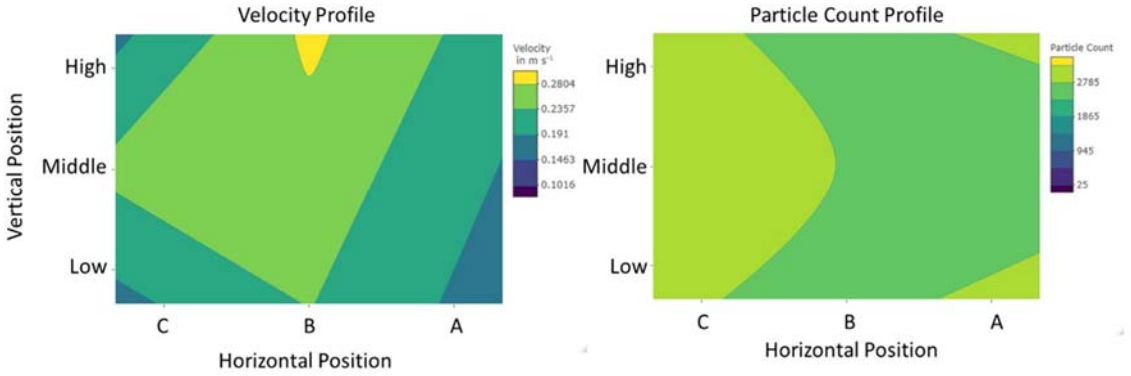

Figure S31. Velocity and Particle Count Profiles in Plane 10 at 0.2 m s^{-1}

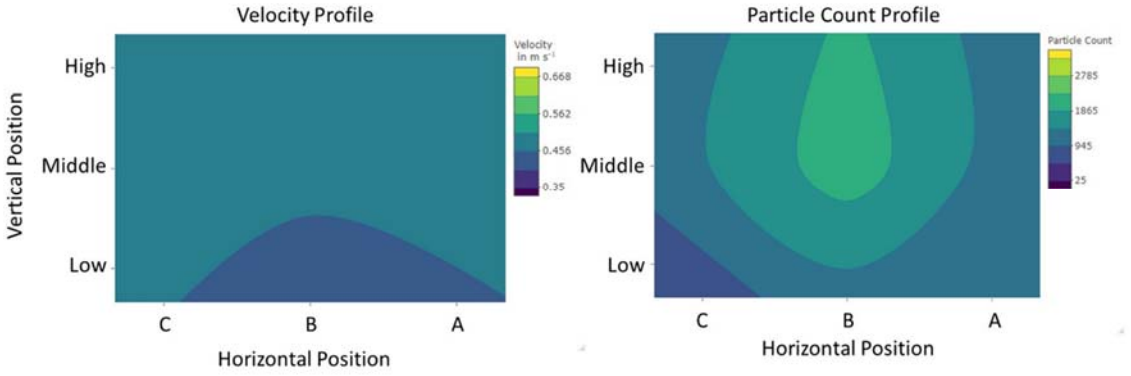

Figure S32. Velocity and Particle Count Profiles in Plane 7 at 0.5 m s^{-1}

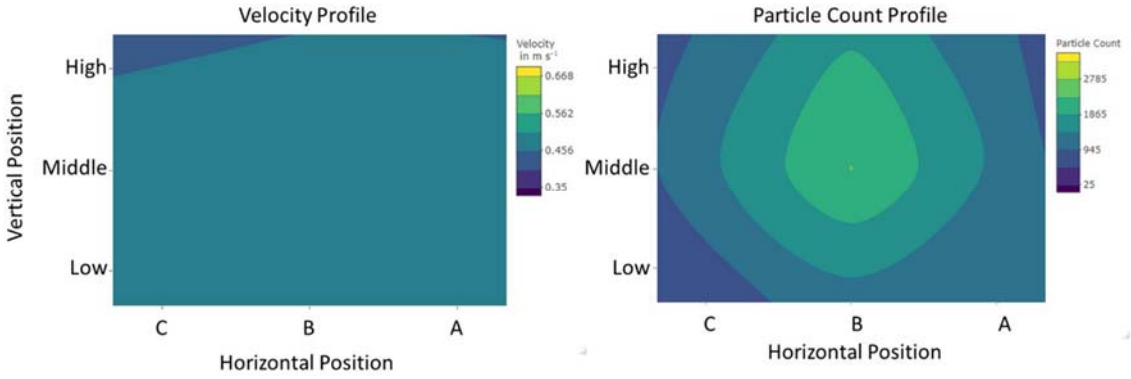

Figure S33. Velocity and Particle Count Profiles in Plane 8 at 0.5 m s^{-1}

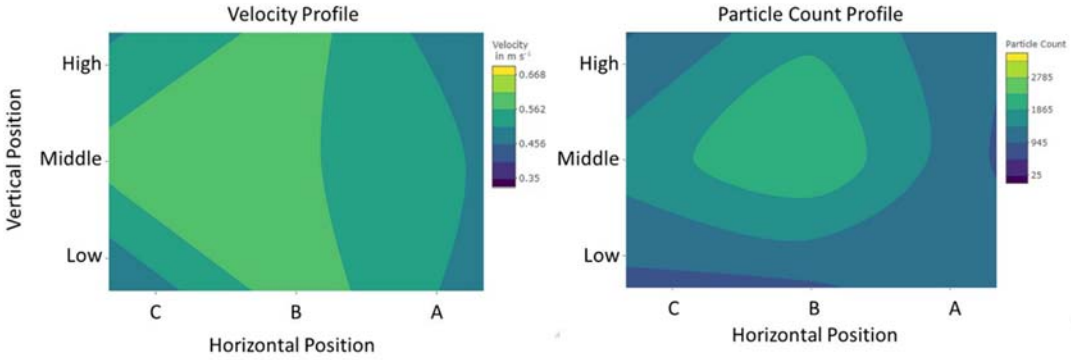

Figure S34. Velocity and Particle Count Profiles in Plane 10 at 0.5 m s^{-1}

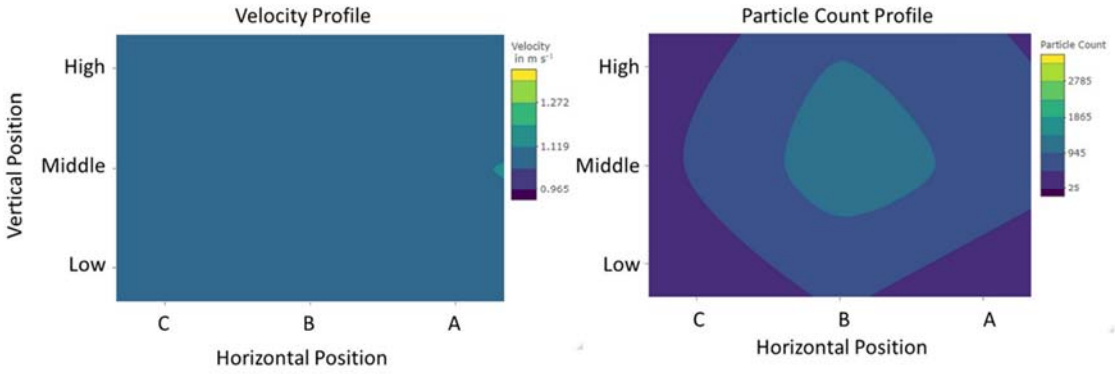

Figure S35. Velocity and Particle Count Profiles in Plane 5 at 1.0 m s^{-1}

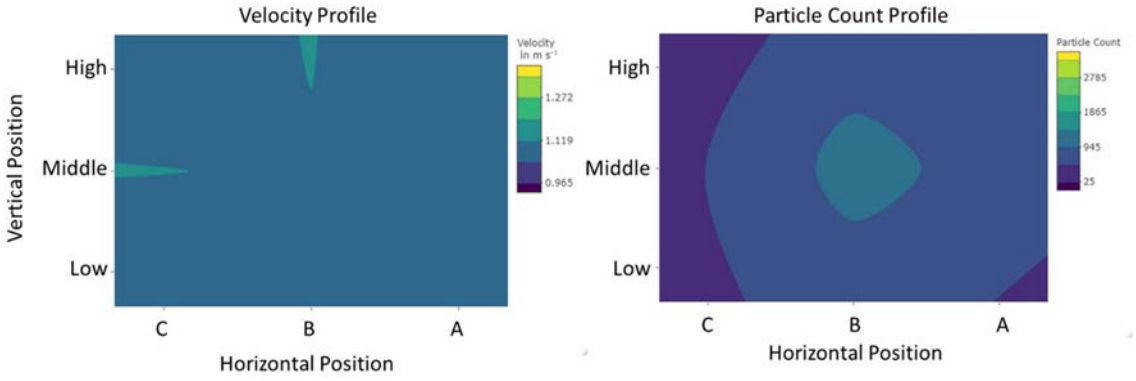

Figure S36. Velocity and Particle Count Profiles in Plane 7 at 1.0 m s^{-1}

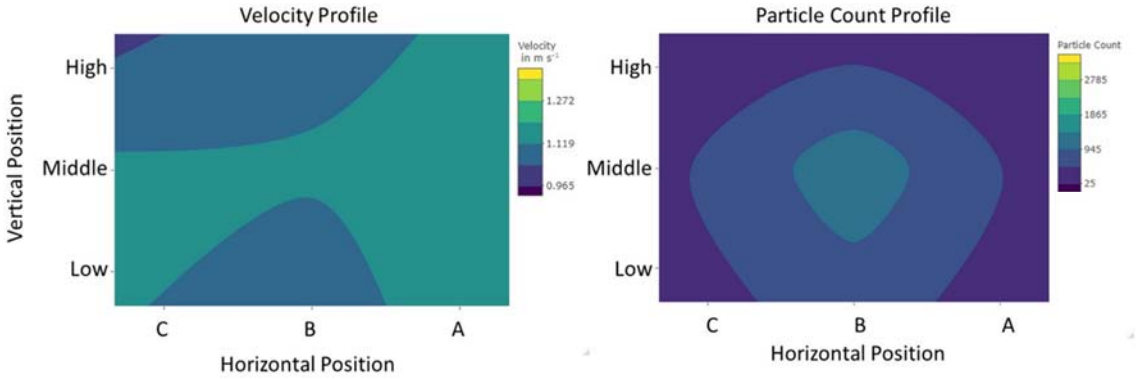

Figure S37. Velocity and Particle Count Profiles in Plane 8 at 1.0 m s^{-1}

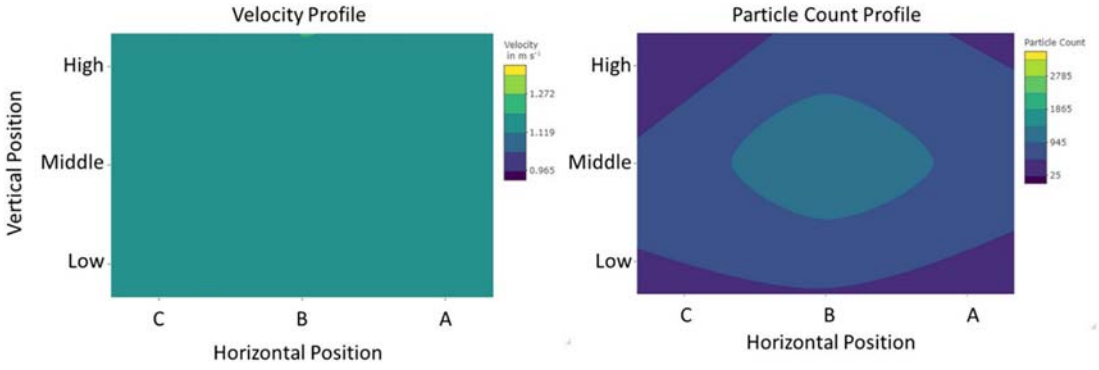

Figure S38. Velocity and Particle Count Profiles in Plane 10 at 1.0 m s^{-1}

S4.2. CFD Model Results

Table S22. Validation Points for Chamber CFD Model

Plane	Grid Square	Velocity (m s^{-1})				Percent Difference
		Measured Velocity	Min (Lower C.I.)	Max (Upper C.I.)	Model Value	
1	A-Low	0.504	0.454	0.555	0.521	3%
	A-Middle	0.491	0.441	0.542	0.522	6%
	A-High	0.539	0.488	0.591	**0.443**	-18%
	B-Low	0.465	0.415	0.514	0.461	-1%
	B-Middle	0.474	0.424	0.524	0.473	0%
	B-High	0.513	0.462	0.564	**0.428**	-17%
	C-Low	0.497	0.447	0.557	0.468	-6%
	C-Middle	0.502	0.451	0.573	0.456	-9%
	C-High	0.557	0.477	0.609	**0.470**	-16%
3	A-Low	0.470	0.421	0.520	**0.543**	15%
	A-Middle	0.477	0.427	0.527	**0.541**	13%
	A-High	0.504	0.454	0.555	0.467	-7%
	B-Low	0.441	0.393	0.502	0.502	14%
	B-Middle	0.425	0.377	0.502	0.485	14%
	B-High	0.427	0.379	0.525	0.452	6%
	C-Low	0.478	0.428	0.528	0.488	2%
	C-Middle	0.496	0.446	0.547	0.485	-2%
	C-High	0.462	0.413	0.512	0.490	6%
5	A-Low	0.445	0.396	0.550	0.546	23%
	A-Middle	0.464	0.415	0.554	0.536	15%
	A-High	0.478	0.423	0.568	0.464	-3%
	B-Low	0.420	0.372	0.555	0.492	17%
	B-Middle*	0.430	0.381	0.605	0.496	15%
	B-High	0.446	0.397	0.562	0.451	1%
	C-Low*	0.471	0.293	0.521	0.492	4%
	C-Middle	0.483	0.433	0.573	0.484	0%

	C-High	0.481	0.431	0.551	0.487	1%
7	A-Low	0.455	0.405	0.545	0.539	19%
	A-Middle	0.484	0.408	0.542	0.533	10%
	A-High	0.473	0.403	0.546	0.458	-3%
	B-Low	0.423	0.375	0.523	0.496	17%
	B-Middle	0.474	0.405	0.577	0.505	6%
	B-High	0.458	0.393	0.534	0.457	0%
	C-Low	0.472	0.364	0.522	0.491	4%
	C-Middle	0.495	0.444	0.562	0.484	-2%
	C-High	0.497	0.414	0.547	0.488	-2%
8	A-Low	0.430	0.381	0.546	0.531	24%
	A-Middle	0.483	0.398	0.533	0.520	8%
	A-High	0.469	0.365	0.519	0.435	-7%
	B-Low	0.432	0.383	0.552	0.504	17%
	B-Middle	0.489	0.424	0.556	0.511	4%
	B-High	0.453	0.398	0.518	0.461	2%
	C-Low	0.483	0.433	0.586	0.492	2%
	C-Middle	0.506	0.453	0.580	0.492	-3%
	C-High	0.474	0.395	0.524	0.485	2%
9	A-Low*	0.410	0.362	0.579	0.522	27%
	A-Middle*	0.479	0.428	0.636	0.468	-2%
	A-High	0.462	0.412	0.548	**0.694**	50%
	B-Low	0.526	0.475	0.578	0.502	-5%
	B-Middle	0.568	0.516	0.621	0.525	-8%
	B-High	0.504	0.453	0.554	0.480	-5%
	C-Low	0.596	0.509	0.676	**0.492**	-17%
	C-Middle	0.599	0.530	0.684	**0.496**	-17%
	C-High	0.534	0.478	0.622	0.495	-7%
10	A-Low*	0.440	0.391	0.656	0.515	17%
	A-Middle*	0.429	0.381	0.616	0.534	24%
	A-High	0.442	0.393	0.545	0.533	21%
	B-Low	0.565	0.488	0.696	0.513	-9%
	B-Middle	0.605	0.533	0.678	0.546	-10%
	B-High	0.577	0.468	0.651	0.487	-16%
	C-Low*	0.464	0.360	0.602	0.498	7%
	C-Middle	0.572	0.519	0.671	**0.501**	-12%
	C-High	0.505	0.439	0.559	0.497	-2%
11	A-Low	0.489	0.439	0.583	0.498	2%
	A-Middle	0.542	0.490	0.654	0.527	-3%
	A-High	0.474	0.420	0.574	0.541	14%

	B-Low	0.477	0.427	0.527	0.521	9%
	B-Middle	0.582	0.529	0.635	0.566	-3%
	B-High	0.596	0.542	0.649	**0.494**	-17%
	C-Low	0.475	0.425	0.525	0.497	5%
	C-Middle	0.551	0.499	0.603	0.508	-8%
	C-High	0.422	0.374	0.470	**0.495**	17%
12	A-Low	0.506	0.455	0.557	0.499	-1%
	A-Middle	0.556	0.504	0.608	0.518	-7%
	A-High	0.515	0.464	0.566	**0.461**	-11%
	B-Low	0.522	0.471	0.573	0.537	3%
	B-Middle	0.618	0.564	0.673	0.572	-8%
	B-High	0.593	0.540	0.646	**0.491**	-17%
	C-Low	0.424	0.375	0.472	**0.502**	18%
	C-Middle	0.502	0.451	0.552	0.511	2%
	C-High	0.440	0.391	0.489	**0.496**	13%
13	A-Low	0.545	0.493	0.597	**0.478**	-12%
	A-Middle	0.536	0.484	0.587	0.525	-2%
	A-High	0.539	0.488	0.591	0.492	-9%
	B-Low	0.560	0.503	0.612	0.544	-3%
	B-Middle	0.586	0.519	0.653	0.575	-2%
	B-High	0.540	0.472	0.642	0.494	-8%
	C-Low	0.563	0.510	0.615	**0.497**	-12%
	C-Middle	0.534	0.482	0.585	0.514	-4%
	C-High	0.498	0.447	0.548	0.497	0%
14	A-Low	0.619	0.565	0.673	**0.459**	-26%
	A-Middle	0.585	0.532	0.639	0.538	-8%
	A-High	0.530	0.479	0.582	0.496	-6%
	B-Low	0.567	0.475	0.643	0.536	-5%
	B-Middle	0.589	0.507	0.648	0.582	-1%
	B-High	0.493	0.443	0.604	0.488	-1%
	C-Low	0.437	0.388	0.485	**0.496**	14%
	C-Middle	0.481	0.431	0.531	0.510	6%
	C-High	0.446	0.397	0.495	0.493	10%
16	A-Low	0.596	0.542	0.649	**0.445**	-25%
	A-Middle	0.593	0.540	0.647	0.557	-6%
	A-High	0.560	0.507	0.612	**0.488**	-13%
	B-Low*	0.479	0.384	0.625	0.524	10%
	B-Middle	0.523	0.472	0.588	**0.589**	13%
	B-High	0.546	0.488	0.638	0.492	-10%
	C-Low	0.449	0.400	0.498	0.484	8%

	C-Middle	0.459	0.410	0.509	**0.509**	11%
	C-High	0.474	0.425	0.524	0.482	2%
18	A-Low*	0.507	0.422	0.651	0.473	-7%
	A-Middle	0.572	0.506	0.630	0.567	-1%
	A-High	0.598	0.492	0.652	**0.484**	-19%
	B-Low	0.398	0.351	0.446	**0.484**	21%
	B-Middle	0.555	0.503	0.607	0.598	8%
	B-High	0.568	0.515	0.620	**0.496**	-13%
	C-Low	0.435	0.387	0.484	0.481	11%
	C-Middle	0.487	0.437	0.538	0.512	5%
	C-High	0.580	0.527	0.633	**0.480**	-17%

References

Brice, T. and T. Hall. No Date. Vapor Pressure. National Weather Service, NOAA, El Paso, TX. Accessed January 3, 2020. https://www.weather.gov/media/epz/wxcalc/vaporPressure.pdf.

Engineers Edge, LLC. (no date) Viscosity of Air, Dynamic and Kinematic. Accessed January 3, 2020. https://www.engineersedge.com/physics/viscosity_of_air_dynamic_and_kinematic_14483.htm

Engineering Toolbox. 2004. Relative Humidity in Air. Accessed January 3, 2020. https://www.engineeringtoolbox.com/relative-humidity-air-d_687.html.

de Nevers, N. 2005. *Fluid Mechanics for Chemical Engineers*. 3rd ed. New York, NY: McGraw-Hill Companies.

Appendix IV Equipment List and Software Versions

TSI Velocicalc® Multi-function Ventilation Meter Model 9565-P

962 Thermoanemometer Articulating Probe Velocity and Temperature

Range 0 to 9,999 ft/min (0 to 50 m/s), 0 to 200°F (-18 to 93°C)

Accuracy ±3% of reading or ±3 ft/min (±0.015 m/s), whichever is greater, ±0.5°F (±0.3°C) Resolution 1 ft/min (0.01 m/s), 0.1°F (0.1°C)

https://www.tsi.com/getmedia/aa0d7904-6902-4773-a2a6-e53be59b0b13/9565-VelociCalc_A4_5001362-web?ext=.pdf

FLIR® C2 Thermal Imaging Camera

IR Sensor 80x60, Spectral Range: 7.5-14 µm.

Measurement: -10°C to +150°C (14 to 302°F)

Accuracy: ± 2°C (±3.6°F) or ± 2% whichever is greater at 25°C (77°F)

https://www.flir.com/products/c2/

SATCO Slide Lamp Dimmer Item 90/1070 https://www.satco.com/90-1070.html

Bosch BLAZE GLM 20 Laser Measure Accuracy ± 0.125in.

https://www.boschtools.com/us/en/boschtools-ocs/laser-measuring-glm-20-143533-p/

Feit Electric 150W Incandescent High Wattage Light Bulb

Keep Model: A8025M12S DC Brushless Fan

Ktaxon Male Body Model Plastic Mannequin https://www.walmart.com/ip/Ktaxon-Male-Body-Model-Plastic-Mannequin-Full-Body-Dress-Form-Shopwindow-Display/191608632?athcpid=191608632&athpgid

=athenaItemPage&athcgid=null&athznid=PWVUB&athieid=v0&athstid=CS004&athguid=70cc7d53-007-173d46984a5184&athancid=null&athena=true

TEKCOPLUS Thermometer Thermocouple K Type 4-Channel Multi Channel SD https://www.amazon.com/Thermometer-Thermocouple-Channel-Datalogger-Temperature/dp/B01HD4WMS8/ref=sr_1_5?dchild=1&keywords=k+type+temperature+logger&qid=1597014366&sr=8-5

Card Data Logger

TWTADE Thermocouple K-type connector https://www.amazon.com/Mini-Connector-Thermocouple-Temperature-Measure-40-350%C2%B0C/dp/B07M84554V/ref=sr_1_1_sspa?dchild=1&keywords=twtade+5+pcs+k+type&qid=1597014657&sr=8-1-spons&psc=1&spLa=ZW5jcnlwdGVkUXVhbGlmaWVyPUEyTFBHSE8xVjY0RDIxJmVuY3J5cHRlZElkPUEwMTE0Njk2MUZCUk4wOEFRQzdCMCZlbmNyeXB0ZWRBZElkPUEwNjE5NzM0MlBLSEdNU1ZSMUZMVSZ3aWRnZXROYW1lPXNwX2F0ZiZhY3Rpb249Y2xpY2tSZWRpcmVjdCZkb05vdExvZ0NsaWNrPXRydWU=

Software List.

COMSOL Multiphysics® 5.4 https://www.comsol.com/

Solidworks 2017 https://www.solidworks.com/

AutoDesk Meshmixer 3.5 http://www.meshmixer.com/

Meshlab 2020.07 https://www.meshlab.net/

FreeCAD https://www.freecadweb.org/

Python in JupyterNotebook 5.7.4 https://www.python.org/

All software was used under license as a commercial product, is open source and or as a free software with public license.

Appendix V Common Model Inputs and Material Properties.

Heat Transfer Module	Input Type	Value	Symbol	Reference Location
Solid	Domain	307 K	T_{ref}	Imported Human Geometry
Fluid	Domain	303 K		Cube Geometry
Heat Source	Domain	101.625 W	Q_0	Imported Human Geometry
Temperature Initial	Initial Condition	303K	T	
Thickness of domain outside of plane	Domain	0.914m	d_z	2-D heat transfer
Inflow	Boundary	303K, 1 atm	T, P	Inlet
Outflow	Boundary			Outlet
Fluid Flow				
Gravity	Domain	z-plane m/s^2	-g_cont	x:0.45m, y:0.20m, z:0.45m
Reference Pressure	Domain	1 atm	P_{ref}	
Fluid	Domain	Air	spf	
Walls	Boundary	No Slip		Cube Geometery
Inlet	Boundary	0.20 m/s	U_0	Cube Geometery
Outlet	Boundary	0.991 atm	P_0	Cube Geometery
Initial Values				
Velocity Flow	Domain	0.20 m/s	**u**	y-plane
Compensate for hydrostatic pressure	Domain	yes		

Material Properties			
Air	**Fluid Domain**		
Thermal Conductivity	Material Property	Temperature Dependent	k
Heat capacity at constant Pressure	Material Property	Temperature Dependent	Cp
Density	Material Property	Temperature Dependent	rho
Dynamic Viscosity	Material Property	Temperature Dependent	mu
Ratio of specific heats	Material Property	1.4	gamma
Skin	**Solid Domain**		
Heat Capacity	Material Property	3391J/(kg*K)	Cp
Density	Material Property	1109 kg/m^3	rho
Thermal Conductivity	Material Property	0.37 W/(m*K)	k

Appendix VI 0.50 m/s Data Tables

0.50 m/s Chamber Only	Right Side (0.304m)		Center (0.457 m) *		Left Side (0.609 m)	
Position	Mean (m/s)	Standard Deviation	Mean (m/s)	Standard Deviation	Mean (m/s)	Standard Deviation
H1	0.48	0.008	0.43	0.015	0.52	0.02
H2	0.46	0.007	0.41	0.007	0.50	0.01
H3	0.46	0.005	0.41	0.012	0.51	0.01
H4*	0.43	0.011	0.40	0.011	0.51	0.01
H5*	0.45	0.017	0.42	0.009	0.54	0.01
H6	0.42	0.007	0.42	0.010	0.54	0.01
H7*	0.42	0.007	0.43	0.014	0.53	0.01
H8*	0.41	0.011	0.44	0.009	0.49	0.01
H9*	0.40	0.014	0.44	0.012	0.50	0.01
H10**	0.39	0.010	0.43	0.015	0.47	0.02
B1	0.39	0.021	0.41	0.013	0.51	0.01
B2	0.40	0.015	0.40	0.012	0.49	0.00
B3	0.46	0.026	0.41	0.007	0.51	0.02
B4	0.44	0.013	0.41	0.009	0.49	0.02
B5	0.44	0.010	0.43	0.022	0.48	0.01
B6	0.42	0.017	0.42	0.018	0.48	0.01
B7	0.43	0.010	0.45	0.014	0.42	0.01
BA1	0.46	0.011	0.44	0.020	0.54	0.01
BA2	0.44	0.007	0.45	0.012	0.51	0.01
BA3	0.44	0.007	0.45	0.012	0.49	0.01
P1	0.39	0.011	0.44	0.016	0.46	0.01
P2	0.42	0.009	0.45	0.004	0.44	0.01
P3	0.44	0.015	0.46	0.012	0.45	0.01
P4	0.45	0.011	0.46	0.010	0.42	0.01
P5	0.42	0.006	0.44	0.010	0.40	0.01
P6	0.44	0.006	0.44	0.014	0.41	0.01
P7	0.42	0.010	0.45	0.007	0.45	0.01
P8	0.40	0.007	0.43	0.010	0.43	0.01
* Measurement locations that 18" is against the manikin head and has no measurement at 24" when manikin is in place.						
** Measurement location when manikin is in place passes under the manikin's neck when manikin is in place.						

0.50 m/s Litter assembly only	Right Side (0.304m)		Center (0.457 m) *		Left Side (0.609 m)	
Position	Mean	Standard Deviation	Mean	Standard Deviation	Mean	Standard Deviation
H1	0.51	0.007	0.47	0.012	0.48	0.019
H2	0.50	0.011	0.45	0.009	0.42	0.019
H3	0.47	0.010	0.45	0.005	0.44	0.008
H4*	0.46	0.009	0.45	0.005	0.39	0.016
H5*	0.46	0.009	0.46	0.006	0.41	0.012
H6	0.43	0.005	0.45	0.012	0.39	0.010
H7*	0.44	0.010	0.44	0.007	0.40	0.009
H8*	0.45	0.007	0.43	0.012	0.44	0.013
H9*	0.45	0.006	0.43	0.007	0.41	0.009
H10**	0.30	0.031	0.35	0.017	0.41	0.013
B1	0.51	0.012	0.45	0.024	0.41	0.012
B2	0.52	0.012	0.43	0.019	0.40	0.011
B3	0.50	0.004	0.47	0.015	0.47	0.011
B4	0.50	0.006	0.46	0.016	0.46	0.013
B5	0.48	0.007	0.46	0.012	0.45	0.009
B6	0.46	0.008	0.45	0.005	0.44	0.015
B7	0.40	0.010	0.45	0.007	0.47	0.005
BA1	0.46	0.005	0.47	0.011	0.46	0.011
BA2	0.46	0.011	0.47	0.009	0.48	0.009
BA3	0.45	0.011	0.46	0.004	0.47	0.007
P1	0.48	0.007	0.45	0.016	0.45	0.012
P2	0.48	0.010	0.45	0.010	0.47	0.007
P3	0.48	0.007	0.47	0.012	0.48	0.004
P4	0.47	0.012	0.47	0.009	0.47	0.009
P5	0.41	0.007	0.42	0.011	0.42	0.004
P6	0.42	0.008	0.44	0.006	0.37	0.008
P7	0.42	0.011	0.44	0.014	0.40	0.008
P8	0.42	0.011	0.44	0.011	0.47	0.005

* Measurement locations that 18" is against the manikin head and has no measurement at 24" when manikin is in place.

** Measurement location when manikin is in place passes under the manikin's neck when manikin is in place.

0.50 m/s Manikin and assembly	Right Side (0.304m)		Center (0.457 m) *		Left Side (0.609 m)	
Position	Mean (m/s)	Standard Deviation	Mean (m/s)	Standard Deviation	Mean (m/s)	Standard Deviation
H1	0.53	0.0207	0.49	0.017	0.51	0.021
H2	0.50	0.0083	0.50	0.009	0.53	0.015
H3	0.45	0.0142	0.46	0.006	0.50	0.019
H4*	0.48	0.0117	0.46	0.008	-	-
H5*	0.38	0.0439	0.10	0.042	-	-
H6	0.40	0.0397	0.32	0.024	0.38	0.019
H7*	0.44	0.0172	0.39	0.022	-	-
H8*	0.21	0.0957	0.09	0.018	-	-
H9*	0.43	0.0222	0.35	0.026	-	-
H10**	0.23	0.0807	0.09	0.031	0.34	0.046
B1	0.60	0.0124	0.53	0.013	0.49	0.019
B2	0.57	0.0148	0.54	0.013	0.50	0.012
B3	0.55	0.0122	0.53	0.013	0.53	0.016
B4	0.51	0.0226	0.55	0.010	0.54	0.014
B5	0.50	0.0174	0.54	0.009	0.53	0.015
B6	0.45	0.0166	0.48	0.010	0.50	0.005
B7	0.26	0.0834	0.22	0.017	0.49	0.010
BA1	0.31	0.0120	0.32	0.054	0.52	0.006
BA2	0.32	0.0328	0.46	0.013	0.53	0.015
BA3	0.29	0.0207	0.38	0.032	0.54	0.009
P1	0.52	0.0169	0.50	0.008	0.50	0.013
P2	0.51	0.0154	0.50	0.007	0.50	0.010
P3	0.52	0.0100	0.48	0.021	0.49	0.011
P4	0.52	0.0141	0.48	0.026	0.48	0.011
P5	0.32	0.0288	0.31	0.035	0.27	0.082
P6	0.35	0.0088	0.32	0.042	0.34	0.013
P7	0.37	0.0158	0.35	0.013	0.42	0.012
P8	0.37	0.0078	0.39	0.016	0.49	0.014

* Measurement locations that 18" is against the manikin head and has no measurement at 24" when manikin is in place.

** Measurement location when manikin is in place passes under the manikin's neck when manikin is in place.

0.50 m/s Heat location	Right Side (0.304m)		Center (0.457 m) *		Left Side (0.609 m)	
Position	Mean (m/s)	Standard Deviation	Mean (m/s)	Standard Deviation	Mean (m/s)	Standard Deviation
BA1	0.51	0.010	0.51	0.013	0.56	0.012
BA2	0.41	0.007	0.46	0.007	0.63	0.019
BA3	0.36	0.023	0.47	0.013	0.48	0.036
P1	0.48	0.013	0.53	0.013	0.54	0.007
P2	0.47	0.009	0.51	0.005	0.52	0.006
P3	0.49	0.008	0.48	0.013	0.52	0.008
P4	0.48	0.008	0.54	0.012	0.52	0.009
P5	0.31	0.017	0.25	0.015	0.44	0.018
P6	0.41	0.014	0.38	0.012	0.40	0.005
P7	0.51	0.036	0.51	0.011	0.50	0.013
P8	0.51	0.014	0.48	0.025	0.42	0.027

0.50 m/s Manikin	Mean (m/s)	Standard Deviation
Forehead	0.354	0.019
Chin	0.021	0.009
Nose	0.283	0.026
Head, Top	0.009	0.003
Chest, Left	0.332	0.015
Chest, Right	0.264	0.017
Abs/Hips, Center	0.344	0.012
Thigh, Left	0.337	0.009
Thigh, Right	0.242	0.024

0.50 m/s Heated Manikin	Mean (m/s)	Standard Deviation
Chest, Left	0.27	0.019
Chest, Right	0.25	0.029
Abs/Hips, Center	0.26	0.007
Thigh, Left	0.24	0.011
Thigh, Right	0.16	0.016

REPORT DOCUMENTATION PAGE

Form Approved
OMB No. 074-0188

1. REPORT DATE *(DD-MM-YYYY)*	2. REPORT TYPE	3. DATES COVERED *(From – To)*
11-09-2020	Master's Thesis	September 2018 – September 2020

TITLE AND SUBTITLE

Survey of Airflow Around a Heated Manikin as a Simulated Aeromedical Evacuation Patient on a Litter with Computational Fluid Dynamics Models

5a. CONTRACT NUMBER

5b. GRANT NUMBER
2018-178R;2019-073

5c. PROGRAM ELEMENT NUMBER

6. AUTHOR(S)

Lemmer, George P., Contractor

5d. PROJECT NUMBER

5e. TASK NUMBER

5f. WORK UNIT NUMBER

7. PERFORMING ORGANIZATION NAMES(S) AND ADDRESS(S)
Air Force Institute of Technology
Graduate School of Engineering and Management (AFIT/ENV)
2950 Hobson Way, Building 640
WPAFB OH 45433-8865

8. PERFORMING ORGANIZATION REPORT NUMBER

AFIT-ENV-MS-20-S-070

9. SPONSORING/MONITORING AGENCY NAME(S) AND ADDRESS(ES)
AFRL/RHBAF
2510 Fifth Street
WPAFB, OH 45433-7765
(937) 938-2671
Dr. Doug Lewis, Doug.lewis.13@us.af.mil

10. SPONSOR/MONITOR'S ACRONYM(S)

AFRL/RHBAF

11. SPONSOR/MONITOR'S REPORT NUMBER(S)

12. DISTRIBUTION/AVAILABILITY STATEMENT
DISTRUBTION STATEMENT A. APPROVED FOR PUBLIC RELEASE; DISTRIBUTION UNLIMITED.

13. SUPPLEMENTARY NOTES
This material is declared a work of the U.S. Government and is not subject to copyright protection in the United States.

14. ABSTRACT

Aeromedical Evacuations remain the predominant method used to transport patients from forward deployed areas of operations to secure locations with more robust medical infrastructure. Transportation of chemical warfare casualties and infectious patients require additional attention to prevent cross contamination. Specific airflow characteristics paired with environmental control system settings are a gap in scholarly literature. Based on the available literature computational fluid dynamics models were created to simulate the airflow around a patient represented by human geometry using commercially available software. In order to compare simulated and experimental results a heated manikin was placed in the MURPHEE aerosol exposure chamber and velocity of the airflow was surveyed. The survey and model results indicated that the heated manikin generated a thermal plume that increased the airflow on average at the sampled positions. More research is required to determine the impact of multiple litters during aeromedical operations and impact on cross contamination from patient to aircraft or aircrew.

15. SUBJECT TERMS
Computational Fluid Dynamics, Aeromedical Environment, C-130, Airflow Around Patients

16. SECURITY CLASSIFICATION OF:			17. LIMITATION OF ABSTRACT	18. NUMBER OF PAGES	19a. NAME OF RESPONSIBLE PERSON
a. REPORT	b. ABSTRACT	c. THIS PAGE			Dr. Jeremy Slagley, AFIT/ENV
U	U	U	UU	142	19b. TELEPHONE NUMBER *(Include area code)* (937) 255-3636, ext 4632 (NOT DSN) (jeremy.slagley@afit.edu)